Determination of the η mass from the production threshold for the $\gamma p \longrightarrow p\eta$ reaction

Dissertation

zur

Erlangung des Doktorgrades (Dr. rer. nat.)

der

Mathematisch-Naturwissenschaftlichen Fakultät

der

Rheinischen Friedrich-Wilhelms-Universität Bonn

vorgelegt von

Alexander Nikolaev

aus

Zyryanovsk, Kasachstan

Bonn, Juli 2011

Angefertigt mit Genehmigung der
Mathematisch-Naturwissenschaftlichen Fakultät der
Rheinischen Friedrich-Wilhelms-Universität Bonn

Diese Dissertation ist auf dem Hochschulschriftenserver der
ULB Bonn (http://hss.ulb.uni-bonn.de/diss_online/) elektronisch
publiziert (Erscheinungsjahr 2012).

1. Referent:	Prof. Dr. Reinhard Beck
2. Referent:	Prof. Dr. Kai-Thomas Brinkmann

Tag der Promotion: 16. Dezember 2011

Erscheinungsjahr: 2012

Abstract

This thesis is dedicated to a new precise determination of the η meson mass based on a measurement of the threshold for the $\gamma p \rightarrow p\eta$ reaction. This experiment was performed in the years 2004/2005 using the Crystal Ball/TAPS detector setup and the recently developed tagger focal-plane microscope detector at the MAMI-B facility in the Institut für Kernphysik of the Johannes Gutenberg-Universität Mainz. The real photon beam was produced by Bremsstrahlung of the 883 MeV electrons from MAMI-B on a thin diamond radiator. The absolute electron energy of the incident beam was precisely determined in the 3rd race-track microtron of MAMI-B. The tagged photon energies were determined using the Glasgow photon tagging spectrometer (tagger). The tagger focal-plane microscope detector was used for the first time in this experiment. It was placed in front of the main focal-plane detector array and improved the tagged photon energy resolution, covering the energy region around the η production threshold ($E_{\mathrm{thr}} = 707\,\mathrm{MeV}$) from $E_\gamma = 674\,\mathrm{MeV}$ to $E_\gamma = 730\,\mathrm{MeV}$ at an electron beam energy $E_0 = 883\,\mathrm{MeV}$. Made of 96 scintillator strips overlapping to one third, the tagger microscope provided 191 tagging channels with an energy resolution of about 290 keV per channel compared to approximately 2 MeV available from the main focal-plane detector. The liquid hydrogen target was located at the center of the Crystal Ball detector. The Crystal Ball, covering polar angles between $\theta = 20^\circ$ and $\theta = 160^\circ$, consisted of 672 NaI(Tl) crystals. In order to distinguish between neutral and charged particles detected by the Crystal Ball, the system was equipped with a particle identification detector (PID) made of plastic scintillator. The forward wall detector, TAPS, had 510 BaF_2 hexagonally shaped crystals, each equipped with a 5 mm thick plastic scintillator for identifying charged particles. The TAPS detector, intended for detecting particles in the forward direction ($\theta = 4^\circ$ - 20°), was located at a distance of 173 cm from the Crystal Ball center, making it possible to use time-of-flight analysis for particle identification.

Special care was taken of the energy calibration of the tagger microscope with electrons of different known energies from MAMI. The calibration of the tagger microscope was performed by varying the magnetic field B_{cal} in the tagging spectrometer around the value B_{exp} used in the experiment. This was done with three different MAMI energies to scan across the tagger microscope by increasing the value of B_{cal} in small steps and plotting the measured hit position of the beam in the microscope versus the equivalent energy. The fit was performed by a least squares

minimization with the aid of the MINUIT package, supposing a linear dependence between tagging electron energy and microscope channel number.

The η mesons were identified via their two main decay modes, $\eta \to 2\gamma$ and $\eta \to 3\pi^0$, with the Crystal Ball/TAPS setup, which measured energies and emission angles of particles. The identification of the $\eta \to 2\gamma$ decay was performed using events with two clusters detected as photons, ignoring all other particles, and the standard invariant mass analysis. Cuts were applied on the invariant and missing mass distributions. The identification of the $\eta \to 3\pi^0 \to 6\gamma$ decay concentrated on events with six clusters detected as photons. Among fifteen possible combinations of six photons to be arranged in three pairs, the combination with the smallest χ^2-value for the three pion masses was assumed to be correct. Cuts were applied on the χ^2-distribution and on the invariant and missing mass distributions. The normalization of the total cross section was obtained from the target thickness, the intensity of the photon flux, the simulated acceptance of the Crystal Ball, and the branching ratios of the η decays. The determination of the η mass required a very precise measurement of the production threshold. This was obtained by fitting the measured cross section as a function of photon energy and gave the result for the η mass,

$$m_\eta = (547.851 \pm 0.031_{\,\text{stat.}} \pm 0.062_{\,\text{syst.}})\,\text{MeV}.$$

This result agrees very well with the precise values of the NA48, KLOE, and CLEO collaborations and deviates by about 5σ from the smaller, but also very precise value obtained by the GEM collaboration at COSY.

Contents

Chapter 1

Introduction

The η meson had been predicted by the *Eightfold Way*, formulated by Murray Gell-Mann in 1961. Named by Gell-Mann χ^0, it was expected to decay into two photons or four pions. However, the discovery of the η meson can be ascribed to Pevsner *et al.* [Pev61] in the same year. Though the discovered η meson decayed into three pions and was apparently unrelated to χ^0, early in 1962, it was properly identified [Bas62] as the pseudoscalar meson predicted by the *Eightfold Way*. In 1964, the η meson was also discovered independently by two groups: Kalbfleisch *et al.* [Kal64] and Goldberg *et al.* [Gol64].

The first bubble-chamber measurements in the 1960's gave the η meson mass $m_\eta \approx (548.8 \pm 0.8)\,\mathrm{MeV}$, which seems to have been systematically high, by about 1 MeV, in comparison with more recent measurements. This thesis is dedicated to the determination of the η mass by measuring the η photoproduction threshold, E_γ^{thr}, from data taken in the years 2004-2005 with the Crystal Ball photon spectrometer and the tagger focal-plane microscope detector at MAMI-B in Mainz. From the kinematics of the reaction $\gamma p \to p\eta$, the η meson mass m_η can be calculated using

$$m_\eta = -m_p + \sqrt{m_p^2 + 2\,m_p\,\frac{E_\gamma^{\mathrm{thr}}}{c^2}}. \tag{1.1}$$

In this relation, m_p is the proton mass, and c is the speed of light in vacuum.

In section 1.1 of this chapter, a short overview of the previous η mass measurements is presented, giving the motivation to the present work, and the outline of the thesis is summarized in section 1.2.

1.1 Motivation

Being a basic property of the particle, the mass plays a key role in fundamental physics. Though it is not really known what mass is, this does not stop one from determining the mass of an elementary particle. The desired accuracy of a mass determination experiment depends on how the result will be used. For example, a

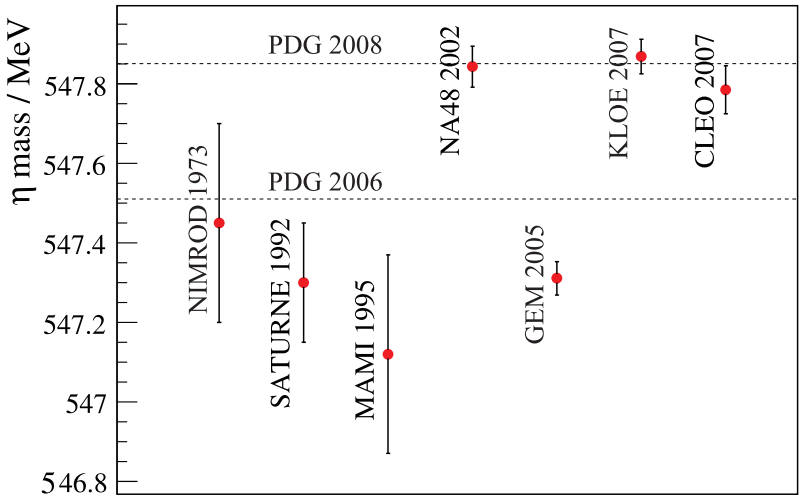

Figure 1.1: Overview of the previous η mass measurements in comparison to the world average published by the PDG in 2006 [Yao06] and 2008 [Ams08].

few percent accuracy would be sufficient for testing the validity of the Gell-Mann – Okubo mass formula [Oku62] of the quark model.

Having a mass between the masses of the π^0 meson and the proton, the η meson is a useful particle when calibrating the beam energy of a 1 GeV particle accelerator or the momentum of a final-state particle. The η has two major neutral decay modes, namely $\eta \to 2\gamma$ (BR = 39.31%) and $\eta \to 3\pi^0 \to 6\gamma$ (BR = 32.56%). The average energy of the decay photons from the first mode is about three times larger than in the second mode. Therefore, the η provides two different calibration points, which can be used, for instance, to check the linearity of the calibration.

The mass of the η meson has been a controversial issue in recent years. Before 2000, three different experiments [Dua74, Plo92, Kru95] yielded comparable masses for the η meson (see fig. 1.1 and table 1.1). The Particle Data Group (PDG) then used these results to calculate a weighted mean mass $m_\eta = (547.30 \pm 0.12)\,\mathrm{MeV}$ [Gro00]. In 2002, the NA48 collaboration published [Lai02] a very precise result, $m_\eta = (547.84 \pm 0.05)\,\mathrm{MeV}$, which deviated significantly from the world average adopted by the PDG. Including the NA48 measurement in the average, the PDG in 2004 [Eid04] obtained the value $m_\eta = (547.75 \pm 0.12)\,\mathrm{MeV}$, almost 0.5 MeV higher than the value reported previously. This created the motivation to repeat the previous Mainz [Kru95] measurement at MAMI, especially after another precise measurement by the GEM collaboration at the COSY facility [Abd05] gave the result $m_\eta = (547.31 \pm 0.04)\,\mathrm{MeV}$, in agreement with the old measurements of the η meson mass.

Furthermore, significant improvements in the experimental facilities have been made since the previous η mass measurement at Mainz. Changes, made on MAMI, provided a more precisely known electron beam energy and much higher beam stability. In addition, on-line monitoring of the primary electron beam and secondary

Facility	Reference	Reaction	η mass, MeV
NIMROD	[Dua74]	$\pi^- p \rightarrow n\,\eta$	547.45 ± 0.25
SATURNE	[Plo92]	$dp \rightarrow {}^3\mathrm{He}\,\eta$	547.30 ± 0.15
MAMI	[Kru95]	$\gamma\,p \rightarrow p\,\eta,\ \eta \rightarrow 2\gamma$	$547.12 \pm 0.06_{\,\mathrm{stat.}} \pm 0.25_{\,\mathrm{syst.}}$
NA48	[Lai02]	$\eta \rightarrow 3\pi^0$	$547.843 \pm 0.030_{\,\mathrm{stat.}} \pm 0.041_{\,\mathrm{syst.}}$
GEM	[Abd05]	$dp \rightarrow {}^3\mathrm{He}\,X$	$547.311 \pm 0.028_{\,\mathrm{stat.}} \pm 0.032_{\,\mathrm{syst.}}$
KLOE	[Amb07]	$\phi \rightarrow \gamma\eta$	$547.874 \pm 0.007_{\,\mathrm{stat.}} \pm 0.031_{\,\mathrm{syst.}}$
CLEO	[Mil07]	$\psi(2S) \rightarrow \eta J/\psi$	$547.785 \pm 0.017_{\,\mathrm{stat.}} \pm 0.057_{\,\mathrm{syst.}}$

Table 1.1: Overview of the previous η mass measurements showing the name of facility or collaboration, where the measurement was performed, reference to the publication, the reaction used in the experiment, and the result for the η mass.

photon beam positions in the experimental hall was introduced. The old TAPS setup with its limited angle coverage was replaced with the large acceptance Crystal Ball detector system, which allowed improvement of the detection efficiency for the two most prominent neutral decay modes of the η meson. Together with the high tagged photon beam energy resolution, offered by the recently developed tagger focal-plane microscope detector, these improvements provided the more accurate determination of the η mass presented in this work.

1.2 Outline

The presented thesis has the following structure. Since the determination of the η mass described in this work requires a very precise measurement of the production threshold, it is necessary to know the behavior of the cross section near threshold. Therefore, in chapter 2, the theoretical model for η photo- and electroproduction on the nucleon developed by W.-T. Chiang *et al.* [Chi02] is presented. The experimental setup at Mainz is described in chapter 3, which includes the MAMI accelerator, single components of the detector setup (photon tagging facility, Crystal Ball photon spectrometer, particle identification detector, TAPS), and the electronics used for readout of the experimental data. In order to convert the raw data, collected during the experiment, into physical quantities, the calibrations of the detector components were done using the procedures described in chapter 4. Chapter 5 is devoted to the Monte Carlo simulations needed for determination of the detector acceptance. The chapter describes the procedure for the generation of events, which then were simulated with the GEANT code using a virtual model of the detector setup. Event selection and reconstruction of the physical reactions are described in chapter 6, and the experimental results and discussion are finally presented in chapter 7.

Chapter 2

Theoretical model

In the last decade, theoretical analyses that describe η photo- and electroproduction on the nucleon have been performed in very different frameworks [Ben95, Bor02, Chi02, Ani05]. Common in most approaches is the dominance of the $S_{11}(1535)$ resonance, which explains the almost isotropic angular distributions of the differential cross sections from the production threshold at $E_\gamma = 707\,\mathrm{MeV}$ up to energies around $E_\gamma = 1\,\mathrm{GeV}$ [Chi02]. The $S_{11}(1535)$ state is well known for its large ηN coupling [Ams08], whereas other resonances couple only weakly to ηN.

This work refers to an isobar model for η photo- and electroproduction, ETA-MAID [Chi02]. The model extends an earlier version of an isobar model by Knöchlein *et al.* [Knö95] and was implemented as a part of the MAID program. Similarly to MAID [Dre99] for pions, ETA-MAID describes η photo- and electroproduction using the nucleon *Born terms*, *vector meson exchange* contributions and resonance excitations parameterized with Breit-Wigner shapes directly connected to the conventional resonance parameters listed in the particle data tables: masses, widths, branching ratios, and photon couplings.

This chapter focuses mainly on the ETA-MAID isobar model [Chi02] and has the following structure. In section 2.1, an introduction to nucleon resonances and mesons is presented. Section 2.2 gives the general formalism for η photo- and electroproduction. The description of the model ingredients and resonance parameterization is presented in section 2.3. Finally, the results of the model fitted to the experimental data from TAPS and GRAAL are shown in section 2.4.

2.1 Nucleon resonances and mesons

Nucleon resonances are excited states of the nucleon with large mass width and well-defined spin, isospin, and parity. They are baryons, which together with mesons build a family of subatomic particles called hadrons. In the quark model of hadron spectroscopy, hadrons are the family of composite particles made of point-like quarks (q). As opposed to mesons, the baryons are composed of three quarks (qqq), whereas mesons are composed of one quark and one antiquark ($q\bar{q}$). The quarks that consti-

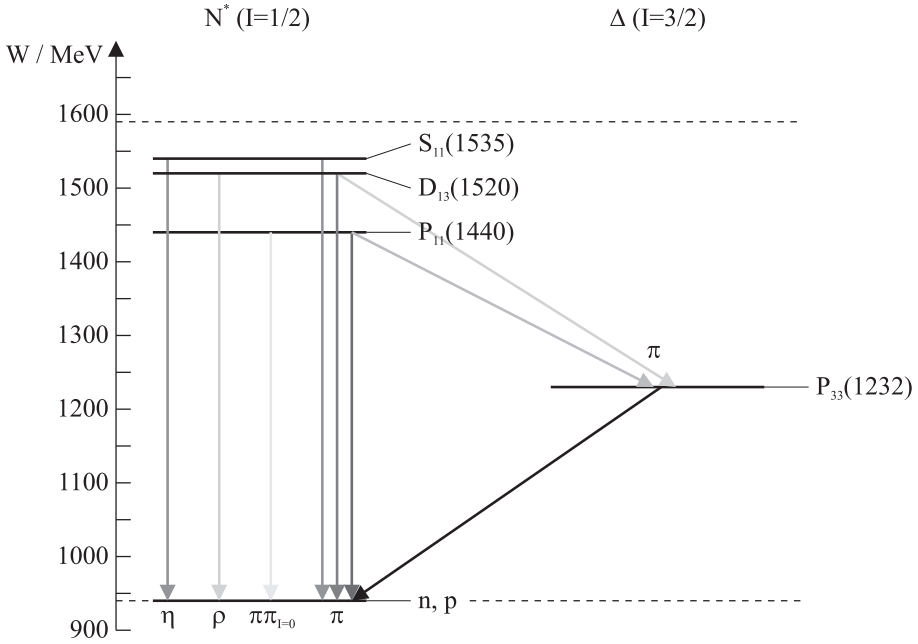

Figure 2.1: The lowest lying nucleon resonances and their decays. The arrows show the mesonic decay channels of the resonances, and the gray scales of the arrows represent the probability of the corresponding decay.

tute a hadron are called valence quarks and give rise to the quantum numbers of the hadron. Quark models of hadrons, based on constituent valence quarks[1], were quite successful in making predictions of hadron properties and could reproduce most of the known resonances as excited states of the nucleon.

The lowest lying nucleon resonances and their most prominent mesonic decays are shown in the energy level diagram in fig. 2.1. In table 2.1, the main properties of these resonances are summarized. They split into two families: N^* with isospin $I = 1/2$ and Δ with isospin $I = 3/2$ [Ams08]. The states are characterized by a letter corresponding to the orbital angular momentum of the decay mode into a pion-nucleon system in spectroscopic notation (S, P, D, F corresponding to $l_{\pi N} = 0, 1, 2, 3$) and two indices. The first index indicates twice the isospin, I, and the second index is twice the total angular momentum, J. The branching ratios for the πN, $\pi\pi N$ or ηN decay modes are shown in the last three columns of table 2.1. In fact, only N^* family resonances can decay into ηN under isospin conservation, since, because the η has zero isospin, the total isospin of the ηN system can only be 1/2. Of high interest is the large branching ratio of $S_{11}(1535)$ into ηN.

In terms of quarks, a meson is constituted by one quark and one antiquark. The mesons with zero orbital angular momentum, which are built of the quarks with the

[1]Since the quark model is derivable from the theory of Quantum chromodynamics (QCD), the structure of hadrons is more complicated: the full wave function of any hadron also includes virtual quark-antiquark pairs as well as virtual gluons.

N^*	$l_{\pi N}$	I	J^P	Mass width, MeV	Branching ratio, %		
					πN	$\pi\pi N$	ηN
$P_{11}(1440)$	1	1/2	$1/2^+$	200-450	55-75	30-40	
$D_{13}(1520)$	2	1/2	$3/2^-$	100-125	55-65	40-50	
$S_{11}(1535)$	0	1/2	$1/2^-$	125-175	35-55	1-10	45-60
$S_{11}(1650)$	0	1/2	$1/2^-$	145-185	60-95	10-20	3-10
$D_{15}(1675)$	2	1/2	$5/2^-$	130-165	35-45	50-60	
Δ							
$P_{33}(1232)$	1	3/2	$3/2^+$	116-120	100		
$P_{33}(1600)$	1	3/2	$3/2^+$	250-450	10-25	75-90	
$S_{31}(1620)$	0	3/2	$1/2^-$	135-150	20-30	70-80	

Table 2.1: Main properties of the lowest lying nucleon resonances [Ams08].

lowest masses (u, d, s), are divided into two classes: vector mesons with $J^P = 1^-$ and pseudoscalar mesons with $J^P = 0^-$. According to the SU(3) symmetry [Don92], each of the two classes consists of an octet and a singlet. Figure 2.2 shows nine pseudoscalar mesons, which form an octet ($\pi^\pm$, π^0, η_o, $K^\pm$, K^0, $\overline{K}^0$) and a singlet (η_s). Note that the physical η and η' mesons are not absolute octet or singlet states but are mixtures of η_o and η_s.

The photoproduction of mesons mainly happens via the intermediate excitation of a resonant state of the nucleon. The diagram of this process for η photoproduction is shown in fig. 2.3 (e). The high energy photon interacts electromagnetically with the nucleon, which is excited to an N^* state decaying again into the nucleon by

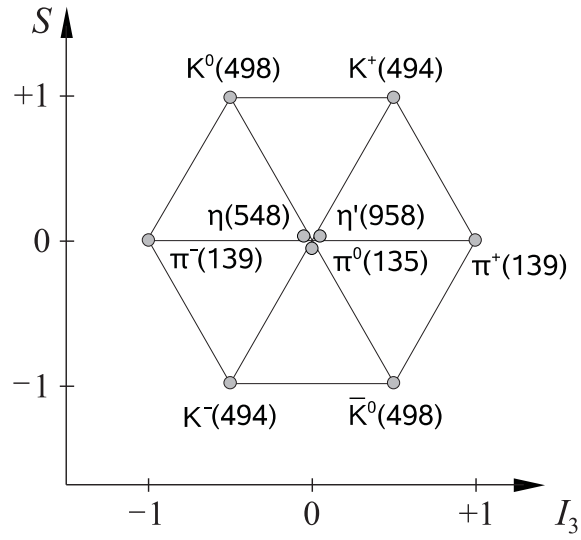

Figure 2.2: Mesons with $J^P = 0^-$ form a nonet of the pseudoscalar mesons. They vary in the third component of the isospin, I_3, and strangeness S.

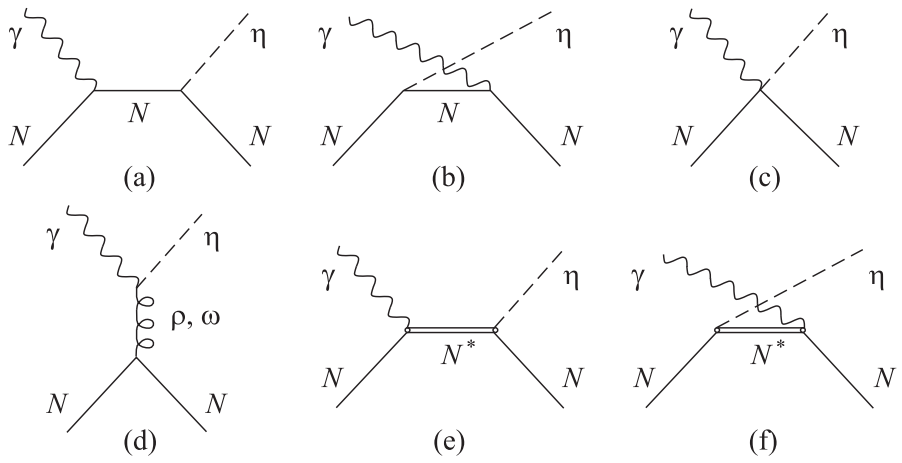

Figure 2.3: Feynman diagrams for η photoproduction: (a), (b) the direct (s-channel) and crossed (u-channel) nucleon *Born term* contributions, (c) the equivalence breaking contribution; (d) the t-channel ρ and ω *vector meson exchanges*; (e), (f) the s- and u-channel nucleon resonance excitations.

emission of an η meson. Besides the excitation of nucleon resonances, a variety of other mechanisms for η photoproduction exists. Some examples are compared to the resonance excitation diagram in fig. 2.3. They include the nucleon *Born terms* (a) - (c), which have an off-shell nucleon in the intermediate state rather than an excited nucleon; the t-channel ρ and ω *vector meson exchanges* (d); and the crossed u-channel resonant diagram (f). Such contributions are called background. It is impossible to separate the background contributions experimentally, since they have initial and final states identical to the resonant s-channel contribution. Also the interference between different contributions complicates the situation, and the interpretation of the experimental data requires descriptions based on the effective Lagrangian. By measuring many different observables, the extraction of the resonant contributions can be simplified.

2.2 Formalism for η photo- and electroproduction

Electromagnetic η production on the nucleon includes photoproduction,

$$\gamma\,(k) + N(p_i) \rightarrow \eta\,(q) + N(p_f), \tag{2.1}$$

and electroproduction,

$$e\,(k_i) + N(p_i) \rightarrow e'\,(k_f) + \eta\,(q) + N(p_f), \tag{2.2}$$

where the 4-momentum for each particle is shown in the parentheses: $k = (\omega, \vec{k})$ for the photon, $k_{i,f} = (\varepsilon_{i,f}, \vec{k}_{i,f})$ for the electron, $p_{i,f} = (E_{i,f}, \vec{p}_{i,f})$ for the nucleon, and $q = (\omega_\eta, \vec{q})$ for the η meson. The electron interacts with the hadronic system

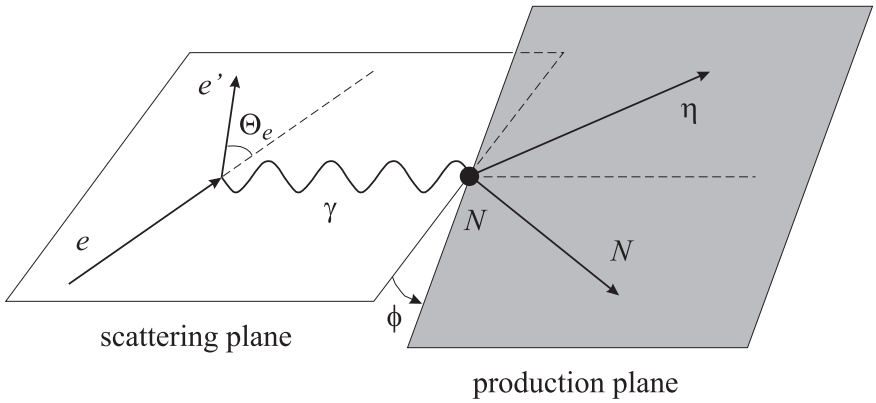

Figure 2.4: Kinematics for the η electroproduction process $eN \rightarrow e'\eta N$ in the laboratory frame.

through the exchange of one virtual photon with 4-momentum $k = k_i - k_f$, and in case of the photoproduction, the photon energy and momentum are related by $k^2 = \omega^2 - \vec{k}^2 = 0$. The squared 4-momentum of the virtual photon is negative, and in this situation a positive quantity $Q^2 = -k^2$ is used to describe form factors and structure functions.

In the center-of-mass (c. m.) frame, where the experimental observables are calculated, the momenta of the initial γN and final ηN states can be expressed in terms of the total c. m. energy W and the square of the momentum transfer, k^2:

$$|\vec{k}| \;=\; |\vec{p}_i| \;=\; \frac{1}{2W}\sqrt{[(W+M)^2 - k^2]\,[(W-M)^2 - k^2]}, \tag{2.3}$$

$$|\vec{q}| \;=\; |\vec{p}_f| \;=\; \frac{1}{2W}\sqrt{[(W+M)^2 - m^2]\,[(W-M)^2 - m^2]}, \tag{2.4}$$

where M and m denote the masses of the nucleon and the η meson. In these terms the threshold photon energy, $E_\gamma^{\rm thr}$, for η production in the laboratory frame is

$$E_\gamma^{\rm thr} = \frac{W^2 - M^2}{2M}\ . \tag{2.5}$$

Using the notation of Bjorken and Drell [Bjo64], the differential cross section for the electroproduction process can be written as[2]

$$\begin{aligned} \mathrm{d}\sigma = {} & \frac{m_e M}{\sqrt{(k_i\cdot p_i)^2 - k_i^2\,p_i^2}}\,\frac{\mathrm{d}^3k_f}{(2\pi)^3}\,\frac{m_e}{\varepsilon_f}\,\frac{\mathrm{d}^3q}{(2\pi)^3}\,\frac{1}{2\omega_\eta}\,\frac{\mathrm{d}^3p_f}{(2\pi)^3}\,\frac{M}{E_f} \\ & \times(2\pi)^4\,\delta^{(4)}\,(k + p_i - q - p_f)\ \left|\langle\, p_f\, q \,|\, J^\mu \,|\, p_i\,\rangle\frac{1}{k^2}\langle\, k_f \,|\, j_\mu \,|\, k_i\,\rangle\right|^2 \end{aligned} \tag{2.6}$$

with the electromagnetic currents j^μ and J^μ of the electron and the hadronic system, respectively.

[2]Formulas presented in this chapter are reproduced from [Knö95] and [Chi02].

The five-fold differential cross section for an electroproduction reaction can be expressed as

$$\frac{\mathrm{d}\sigma}{\mathrm{d}\Omega_f\,\mathrm{d}\varepsilon_f\,\mathrm{d}\Omega} = \Gamma\,\frac{\mathrm{d}\sigma_v}{\mathrm{d}\Omega}\,, \tag{2.7}$$

where $\mathrm{d}\sigma_v/\mathrm{d}\Omega$ is the differential cross section of the virtual photon, and Γ is the flux of the virtual photon field given by

$$\Gamma = \frac{\alpha}{2\pi^2}\,\frac{\varepsilon_f}{\varepsilon_i}\,K\,\frac{1}{1-\varepsilon}\,, \tag{2.8}$$

where ε is the transverse polarization parameter of the virtual photon, and $K = (W^2 - M^2)/2M$ indicates the energy of the real photon in the laboratory frame that is necessary to excite a hadronic system with the total c. m. energy W. Since it is convenient to express the angular distribution of the η mesons in the c. m. frame, the virtual photon cross section $\mathrm{d}\sigma_v/\mathrm{d}\Omega$ has to be evaluated in the c. m. frame. The transverse polarization parameter ε of the virtual photon,

$$\varepsilon = \left(1 + 2\frac{\vec{k}^2}{Q^2}\tan^2\frac{\Theta_e}{2}\right)^{-1}\,, \tag{2.9}$$

is invariant under collinear transformations, and photon momentum $\vec{k}$ and scattering angle Θ_e (see fig. 2.4) may be expressed in the laboratory or c. m. frame. By choosing the energies $\varepsilon_{i,f}$ of the electron in the initial and final states and the scattering angle Θ_e, the momentum transfer Q^2 and the polarization parameter ε of the virtual photon can be fixed. For an unpolarized target and without recoil polarization, the virtual photon differential cross section is

$$\begin{aligned}\frac{\mathrm{d}\sigma_v}{\mathrm{d}\Omega} = \frac{\mathrm{d}\sigma_T}{\mathrm{d}\Omega} + \varepsilon\frac{\mathrm{d}\sigma_L}{\mathrm{d}\Omega} + \sqrt{2\varepsilon(1+\varepsilon)}\,\frac{\mathrm{d}\sigma_{LT}}{\mathrm{d}\Omega}\cos\phi \\ +\varepsilon\frac{\mathrm{d}\sigma_{TT}}{\mathrm{d}\Omega}\cos 2\phi + h\sqrt{2\varepsilon(1+\varepsilon)}\,\frac{\mathrm{d}\sigma_{LT'}}{\mathrm{d}\Omega}\sin\phi\,,\end{aligned} \tag{2.10}$$

where ϕ is the azimuthal angle between the electron scattering plane and the η production plane (see fig. 2.4), and $h = \vec{\sigma}\cdot\hat{\vec{k}}_i = \pm 1$ is the helicity of the incident electron with longitudinal polarization. Note that all kinematical variables appearing in $\mathrm{d}\sigma_v/\mathrm{d}\Omega$ have to be expressed in the c. m. frame. The first two contributions, $\mathrm{d}\sigma_T/\mathrm{d}\Omega$ and $\mathrm{d}\sigma_L/\mathrm{d}\Omega$, are the transverse and longitudinal cross sections and do not depend on ϕ. The $\mathrm{d}\sigma_{LT}/\mathrm{d}\Omega$ and $\mathrm{d}\sigma_{LT'}/\mathrm{d}\Omega$ describe longitudinal-transverse interferences, and the $\mathrm{d}\sigma_{TT}$ is the transverse-transverse interference term.

In pseudoscalar meson production, three types of polarization measurement can be performed: polarization of the photon beam, polarization of the target nucleon, and polarization of the recoil nucleon. For the most general expression of the differential cross section for a coincidence experiment with all three types of polarization see [Knö95]. In the case of a photoproduction experiment, the longitudinal components vanish, and the relevant response functions are divided by the transverse

Photon		Target			Recoil			Target + Recoil			
	$-$	$-$	$-$	$-$	x'	y'	z'	x'	x'	z'	z'
	$-$	x	y	z	$-$	$-$	$-$	x	z	x	z
unpolarized	σ_0	0	T	0	0	P	0	$T_{x'}$	$-L_{x'}$	$T_{z'}$	$L_{z'}$
linear pol.	$-\Sigma$	H	$-P$	$-G$	$O_{x'}$	$-T$	$O_{z'}$	$-L_{z'}$	$T_{z'}$	$-L_{x'}$	$-T_{x'}$
circular pol.	0	F	0	$-E$	$-C_{x'}$	0	$-C_{z'}$	0	0	0	0

Table 2.2: Polarization observables in pseudoscalar meson photoproduction. Target polarization is described in the frame $\{x, y, z\}$ with the z-axis pointing into the direction of the photon momentum $\vec{k}$, the y-axis perpendicular to the reaction plane, and the x-axis given by $\vec{x} = \vec{y} \times \vec{z}$. For recoil polarization the frame $\{x', y', z'\}$ is used with the z'-axis defined by the outgoing η momentum vector $\vec{q}$, the y'-axis as for the target polarization, and the x'-axis given by $\vec{x}' = \vec{y}' \times \vec{z}'$.

response function in order to obtain the polarization observables that are summarized in table 2.2. The photoproduction differential cross sections can be sorted by the three classes of double polarization experiments:

- polarized photons and polarized target,
- polarized photons and recoil polarization,
- polarized target and recoil polarization.

There are sixteen different polarization observables for photoproduction experiments, and a minimum of eight carefully chosen observables can uniquely determine [Chi97] the contributing amplitudes. The next section briefly summarizes how the observables and response functions are selected in the framework of the ETA-MAID isobar model.

2.3 ETA-MAID isobar model

The ETA-MAID isobar model is closely related to the unitary isobar model MAID for pions developed by Drechsel *et al.* [Dre99], but, in contrast to MAID, the unitarization procedure in η production is not feasible due to lack of the necessary information on eta-nucleon scattering.

Background contribution

The background is described by the *Born terms* and *vector meson exchange* contributions, obtained by evaluating the Feynman diagrams (see fig. 2.3) derived from an effective Lagrangian. For the electromagnetic vertex γNN the Lagrangian has the following structure:

$$\mathcal{L}_{\gamma NN} = -e\,\bar{\psi}\left[\gamma_\mu A^\mu F_1^{p,n}(Q^2) + \frac{\sigma_{\mu\nu}}{2m_N}(\partial^\mu A^\nu) F_2^{p,n}(Q^2)\right]\psi\,, \tag{2.11}$$

where A^μ is the electromagnetic vector potential, ψ is the nucleon field operator, and $(F_{1,2}^p)$ and $(F_{1,2}^n)$ are proton and neutron electromagnetic form factors, which depend on Q^2. For real photons the form factors are normalized to $F_1^p(0) = 1$, $F_1^n(0) = 0$, $F_2^p(0) = \kappa_p = 1.79$, and $F_2^n(0) = \kappa_n = -1.97$.

For the hadronic vertex ηNN, two types of couplings are possible, namely pseudoscalar (PS) coupling and pseudovector (PV) coupling. The effective Lagrangians for each type of the ηNN coupling are given by

$$\mathcal{L}_{\eta NN}^{\rm PS} = -i\, g_{\eta NN}\, \bar{\psi}\, \gamma_5\, \psi\, \phi_\eta\,, \quad \mathcal{L}_{\eta NN}^{\rm PV} = \frac{g_{\eta NN}}{2m_N}\, \bar{\psi}\, \gamma_5\, \gamma_\mu\, \psi\, \partial^\mu \phi_\eta\,. \tag{2.12}$$

In contrast to the πN interaction, where PS coupling is ruled out by chiral symmetry, little is known about the ηN interaction. Neither PS nor PV coupling is ruled out by chiral symmetry as in the case of pion production, and both couplings can occur in the ηN interaction, where the symmetry breaks. Nevertheless, according to [Tia94], the PS coupling was chosen.

The effective Lagrangians (2.11) - (2.12) allow construction of the *Born terms*. For the other part of background, the *vector meson exchange* vertices $\gamma\eta V$ and VNN ($V = \rho, \omega$), the effective Lagrangians can be written as

$$\mathcal{L}_{\gamma\eta V} = \frac{e\lambda_V}{m_\eta}\, \varepsilon_{\mu\nu\rho\sigma}\, (\partial^\mu A^\nu)\, \phi_\eta\, (\partial^\rho V^\sigma)\, F_V^{\rm em}(Q^2)\,, \tag{2.13}$$

$$\mathcal{L}_{VNN} = \bar{\psi}\, \left(g_v \gamma_\mu + \frac{g_t}{2m_N}\, \sigma_{\mu\nu}\, \partial^\nu \right)\, V^\mu \psi\,, \tag{2.14}$$

with the following parameters: the electromagnetic couplings, λ_V, of the vector mesons, the electromagnetic form factor $F_V^{\rm em}(Q^2)$, and hadronic couplings g_v (vector coupling) and g_t (tensor coupling). The λ_V are determined from the radiative decay widths $\Gamma_{V\to\eta\gamma}$ via

$$\Gamma_{V\to\eta\gamma} = \frac{\alpha\, (m_V^2 - m_\eta^2)^3}{24\, m_V^3 m_\eta^2}\, \lambda_V^2\,. \tag{2.15}$$

The electromagnetic form factor $F_V^{\rm em}(Q^2)$ is assumed to have the usual dipole behavior, and the off-shell behavior of the hadronic couplings g_v and g_t is described by a dipole form factor

$$g_{v,t} = \tilde{g}_{v,t} \frac{(\Lambda_V^2 - m_V^2)^2}{(\Lambda_V^2 + \vec{k}_V^2)^2}, \tag{2.16}$$

where the values for the strong coupling constants $\tilde{g}_v$ and $\tilde{g}_t$ were taken as free parameters to be varied within certain ranges [Chi02] to fit the measured cross sections.

Resonance contribution

Besides the dominant resonance $S_{11}(1535)$, the N^* contributions $D_{13}(1520)$, $S_{11}(1650)$, $D_{15}(1675)$, $F_{15}(1680)$, $D_{13}(1700)$, $P_{11}(1710)$, and $P_{13}(1720)$ are also considered in the

N^*	Mass	Width	$\zeta_{\eta N}$	$\beta_{\eta N}$	$\beta_{\pi N}$	$\beta_{\pi\pi N}$
$D_{13}(1520)$	1520	120	+1	$0.08 \pm 0.01\%$	$50-60\%$	$40-50\%$
				$\underline{0.06\%}$	60%	40%
$S_{11}(1535)$	1520-1555	100-250	+1	$30-55\%$	$35-55\%$	$1-10\%$
	$\underline{1541}$	$\underline{191}$		50%	40%	10%
$S_{11}(1650)$	1640-1680	145-190	−1	$3-10\%$	$55-90\%$	$10-20\%$
	$\underline{1638}$	$\underline{114}$		$\underline{7.9\%}$	77%	15%
$D_{15}(1675)$	1670-1685	150	−1	$0.1 \pm 0.1\%$	$40-50\%$	$50-60\%$
	$\underline{1665}$			$\underline{17\%}$	40%	43%
$F_{15}(1680)$	1675-1690	130	+1	$0.15 \pm 0.3\%$	$60-70\%$	$30-40\%$
	$\underline{1681}$			$\underline{0.06\%}$	60%	40%
$D_{13}(1700)$	1700	100	−1	$10 \pm 6\%$	$5-15\%$	$85-95\%$
				$\underline{0.3\%}$	15%	85%
$P_{11}(1710)$	1680-1740	100	+1	$16 \pm 10\%$	$10-20\%$	$40-90\%$
	$\underline{1721}$			$\underline{26\%}$	14%	60%
$P_{13}(1720)$	1720	150	+1	$0.2 \pm 1\%$	$10-20\%$	$> 70\%$
				$\underline{3.0\%}$	15%	82%

Table 2.3: Parameters of the nucleon resonances used in the ETA-MAID model. The masses and widths are given in MeV, $\zeta_{\eta N}$ gives the relative sign between $N^* \to \eta N$ and $N^* \to \pi N$ couplings, and $\beta_{\eta N,\, \pi N,\, \pi\pi N}$ are the branching ratios for the corresponding decay channels. The values in the first rows are given by the PDG [Gro00], the numbers in the second rows were used in the model, and the underlined ones were determined from data fitting [Chi02].

model. The cross section is parametrized using a Breit-Wigner energy dependence of the form

$$\mathcal{M}_{\ell\pm}(W, Q^2) = \tilde{\mathcal{M}}_{\,\ell\pm}(Q^2)\, \frac{W_R \Gamma_{\rm tot}(W)}{W_R^2 - W^2 - i W_R \Gamma_{\rm tot}(W)}\, f_{\eta N}(W)\, C_{\eta N}, \tag{2.17}$$

where $\mathcal{M}_{\ell\pm}$ denotes the relevant multipole amplitudes $E_{\ell\pm}$, $M_{\ell\pm}$, or $S_{\ell\pm}$ of the resonance contributions, and $f_{\eta N}(W)$ is the usual Breit-Wigner factor describing the decay $N^* \to \eta N$ of the resonance with total width $\Gamma_{\rm tot}$, partial width $\Gamma_{\eta \rm N}$, and spin J. For this factor

$$f_{\eta N}(W) = \zeta_{\eta N} \left[\frac{1}{(2J+1)\pi}\, \frac{k_W}{|\vec{q}|}\, \frac{m_N}{W_R}\, \frac{\Gamma_{\eta N}}{\Gamma_{\rm tot}^2} \right]^{1/2}, \quad k_W = \frac{W^2 - m_N^2}{2W} \tag{2.18}$$

apply, where $\zeta_{\eta N} = \pm 1$ describes the relative sign between $N^* \to \eta N$ and $N^* \to \pi N$ couplings, the isospin factor $C_{\eta N}$ is -1, and $\tilde{E}_{\ell\pm}$, $\tilde{M}_{\ell\pm}$ are related to the photon excitation helicity amplitudes by

$$A_{1/2}^{\ell+} = -\frac{1}{2} \left[(\ell+2)\tilde{E}_{\ell+} + \ell\, \tilde{M}_{\ell+} \right],$$

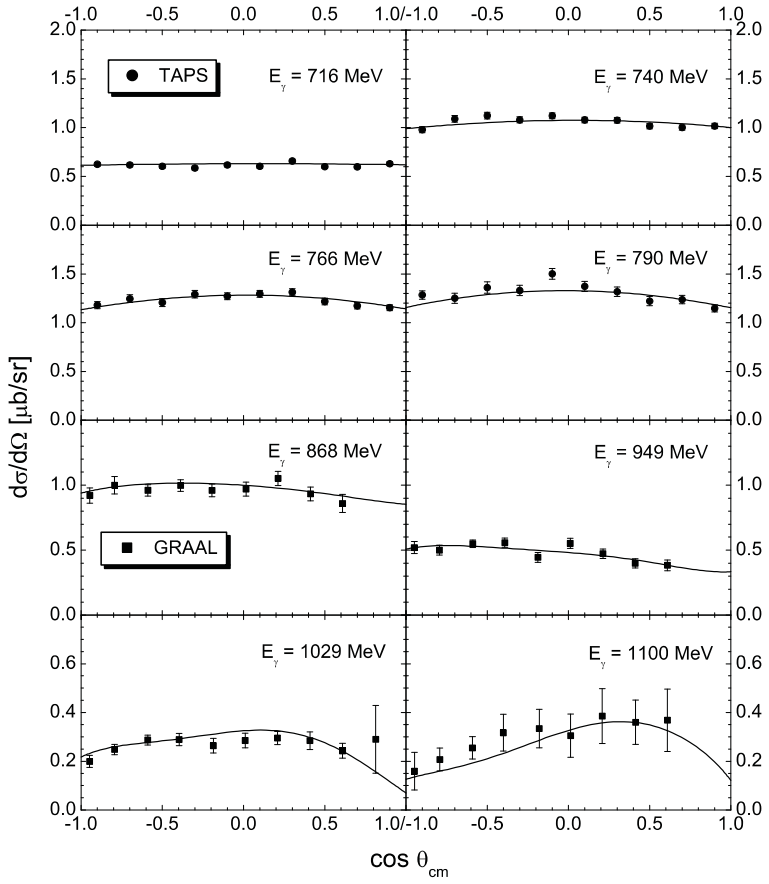

Figure 2.5: Differential cross section for $\gamma p \to p\eta$ [Chi02]. The experimental data are from TAPS [Kru95] and GRAAL [Ren02].

$$
\begin{aligned}
A_{3/2}^{\ell+} &= -\frac{1}{2}\sqrt{\ell(\ell+2)}\,\left(\tilde{E}_{\ell+} - \tilde{M}_{\ell+}\right), \\
A_{1/2}^{(\ell+1)-} &= -\frac{1}{2}\,\left[\ell\tilde{E}_{(\ell+1)-} - (\ell+2)\,\tilde{M}_{(\ell+1)-}\right], \\
A_{3/2}^{(\ell+1)-} &= -\frac{1}{2}\sqrt{\ell(\ell+2)}\,\left(\tilde{E}_{(\ell+1)-} + \tilde{M}_{(\ell+1)-}\right).
\end{aligned} \tag{2.19}
$$

The scalar multipole amplitudes $S_{\ell\pm}$ appear only in electroproduction. In accordance with [Wal69], the energy dependence of the partial width $\Gamma_{\eta N}$ can be expressed as

$$
\Gamma_{\eta N}(W) = \beta_{\eta N}\Gamma_R \left(\frac{|\vec{q}\,|}{|\vec{q}_R|}\right)^{2\ell+1} \left(\frac{X^2+\vec{q}_R^{\,2}}{X^2+\vec{q}^{\,2}}\right)^{\ell} \frac{W_R}{W}, \tag{2.20}
$$

where X is a parameter, assumed to be 500 MeV for all resonances. Γ_R and $\vec{q}_R$ are the total width and the η c. m. momentum at the resonance peak ($W = W_R$) respectively, and $\beta_{\eta N}$ is the ηN decay branching ratio.

The total width $\Gamma_{\rm tot}$ in equations (2.17) and (2.18) is given by the sum

$$
\Gamma_{\rm tot}(W) = \Gamma_{\eta N}(W) + \Gamma_{\pi N}(W) + \Gamma_{\pi\pi N}(W), \tag{2.21}
$$

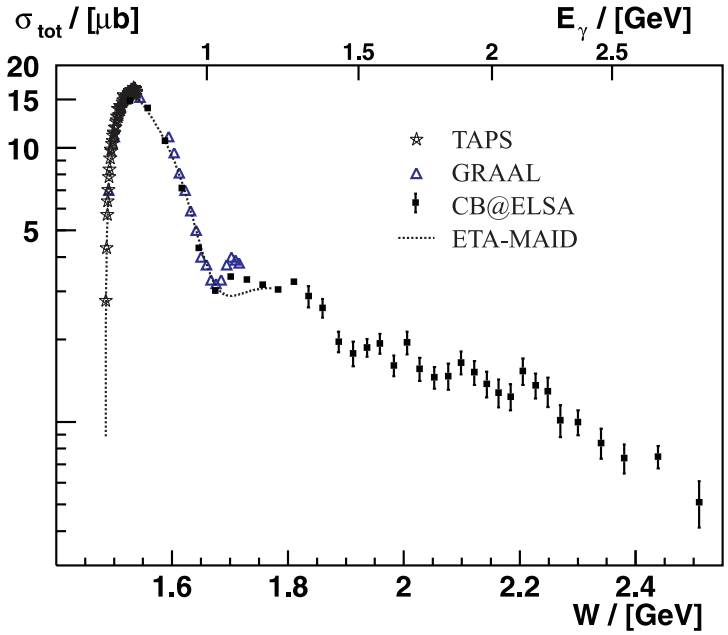

Figure 2.6: Total cross section for $\gamma p \to p\eta$ [Chi02]. The experimental data are from TAPS [Kru95], GRAAL [Ren02], and CB@ELSA [Cre05].

where $\Gamma_{\eta N,\,\pi N,\,\pi\pi N}$ are the widths of the corresponding decays of the N^*. The width $\Gamma_{\pi N}$ has a similar energy dependence as $\Gamma_{\eta N}$, and $\Gamma_{\pi\pi N}$ is parameterized in an energy dependent form:

$$\Gamma_{\pi N}(W) = \beta_{\pi N}\Gamma_R \left(\frac{|\vec{q}_\pi|}{|\vec{q}_R|}\right)^{2\ell+1} \left(\frac{X^2+\vec{q}_R^{\,2}}{X^2+\vec{q}_\pi^{\,2}}\right)^{\ell} \frac{W_R}{W}\,, \tag{2.22}$$

$$\Gamma_{\pi\pi N}(W) = (1-\beta_{\pi N}-\beta_{\eta N})\,\Gamma_R \left(\frac{q_{2\pi}}{q_0}\right)^{2\ell+4} \left(\frac{X^2+q_0^2}{X^2+q_{2\pi}^2}\right)^{\ell+2}\,, \tag{2.23}$$

where $q_{2\pi}$ is the momentum of the compound (2π) system with mass $2m_\pi$ and $q_0 = q_{2\pi}$ at $W = W_R$. The definition of $\Gamma_{\pi\pi N}$ has been chosen to account for the correct energy behavior of the phase space near the three-body threshold. The resonance parameters in this isobar model are given in table 2.3. For more details about the ETA-MAID model the reader is referred to [Chi02].

2.4 Photoproduction cross sections

The η photoproduction cross sections, obtained from the isobar model, described in the previous section, were fitted [Chi02] to the experimental data including total and differential cross sections from TAPS [Kru95] and GRAAL [Ren02].

The TAPS data [Kru95] included differential cross sections as well as the total cross section from the production threshold at $E_\gamma = 707\,\text{MeV}$ up to the energy

$E_\gamma = 790\,\mathrm{MeV}$, which is nearly the peak of the $S_{11}(1535)$ resonance. The GRAAL data covered a wider energy region, from the threshold energy up to $E_\gamma = 1100\,\mathrm{MeV}$, but did not provide the total cross section independently, which was obtained by integration of the differential cross sections.

The resonance parameters obtained by fitting the model to the total and differential experimental cross sections are shown in table 2.3. In fig. 2.5, the resulting ETA-MAID differential cross sections are in very good agreement with the experimental data from TAPS and GRAAL. Due to s-wave dominance in the low energy region, the differential cross sections are flat, while at higher energies, higher partial waves start to contribute. The results for the total cross sections are shown in fig. 2.6 in comparison to the experimental data. Again, these are in good agreement except for the bump observed in the GRAAL data in the region above $E_\gamma = 1050\,\mathrm{MeV}$ that could not be reproduced in the model. However, the total cross section of the GRAAL data is obtained from integrating the differential cross sections, by use of a polynomial fit in $\cos\theta$ to extrapolate the data into the unmeasured parts of the angle range [Chi02]. Therefore, it is more meaningful to compare the differential cross sections directly.

Since the determination of the η mass requires a very precise measurement of the production threshold, it is necessary to know the behavior of the cross section near threshold. One can see in fig. 2.6 that the background contribution is very small, and the total cross section is strongly dominated by the $S_{11}(1535)$ in the threshold region. Though the exclusion of the second resonance, $S_{11}(1650)$, leads to incorrect resonance parameters, the single $S_{11}(1535)$ resonance (the dash-dotted curve in fig. 2.6) fits the data very nicely in the threshold region. This fact can be used for precise measurement of the threshold energy from the total cross section data near threshold.

Chapter 3

Experimental detector setup

In this chapter the experimental setup of the Crystal Ball/TAPS experiment at MAMI is described. The experiment was carried out in the A2 experimental hall (see fig. 3.1), in the Institut für Kernphysik, in Mainz. The data, concerning the topic of this work, were collected in December 2004 and January 2005. The electron accelerator MAMI (Mainz Microtron) provided a high quality electron beam with a maximum energy of 883 MeV. The electron beam was used to produce an energy tagged Bremsstrahlung photon beam with the Glasgow-Mainz photon tagging spectrometer (tagger). The photon beam interacted with a liquid hydrogen target inducing the nuclear reactions. The target was placed in the center of the Crystal Ball (CB) photon spectrometer. The detector system also comprized a particle identification detector (PID), multi-wire proportional chambers (MWPCs), and a forward detector, TAPS. The Crystal Ball provided the energies and emission angles of particles emitted into over 94% of the solid angle around the target. The PID, a cylinder of 24 plastic scintillator strips, was used to identify charged particles detected in the CB. The MWPCs were intended to make possible accurate determination of the origin of a charged particle within the target, but they were not used in this experiment and, thus, are not described in this work. The TAPS detector provided the identification of the particles in the forward region. In the following sections of this chapter these components are described in more detail. An overview of the electronics used to read out the data from the photomultipliers is presented in the second half of this chapter.

3.1 Mainz Microtron MAMI

The electron accelerator of the Institut für Kernphysik in the configuration MAMI-B [Her76, Wal90] is a cascade of three race-track microtrons (RTM), delivering since 1991 a high-quality continuous wave electron beam current of up to 100 μA. It begins with an injector linac supplying electrons with a total energy of 3.97 MeV, which are accelerated through the three stages, RTM1, RTM2, and RTM3, to an end energy of 855 MeV. The main parameters of the RTMs are summarized in table 3.1. The beam

is delivered to the A2 experimental hall, shown in fig. 3.1. The fourth stage (MAMI-C), harmonic double-sided microtron (HDSM), was under construction during our experiment. It can raise the maximum beam energy up to 1.6 GeV.

The operating principle of a race-track microtron is illustrated in fig. 3.2. The microtron consists of a single linac and two constant field B bending magnets. The bunched electron beam with the energy E_{inj} after injection is steered into the linac and is accelerated, gaining the energy ΔE. The purpose of the bending magnets is to steer the beam and direct it to the linac again. The microtron is designed in such a way that the electron bunches always see the same phase of the alternating electromagnetic field in the accelerating section. As the electron energy E_n increases, the radius R_n of the beam path through the magnets grows. The procedure of beam recirculation through the linac can be repeated until the radius of the particle's path makes further acceleration impossible. The electron beam with the energy E_{ext} is then deflected into an experiment area or a further accelerator stage.

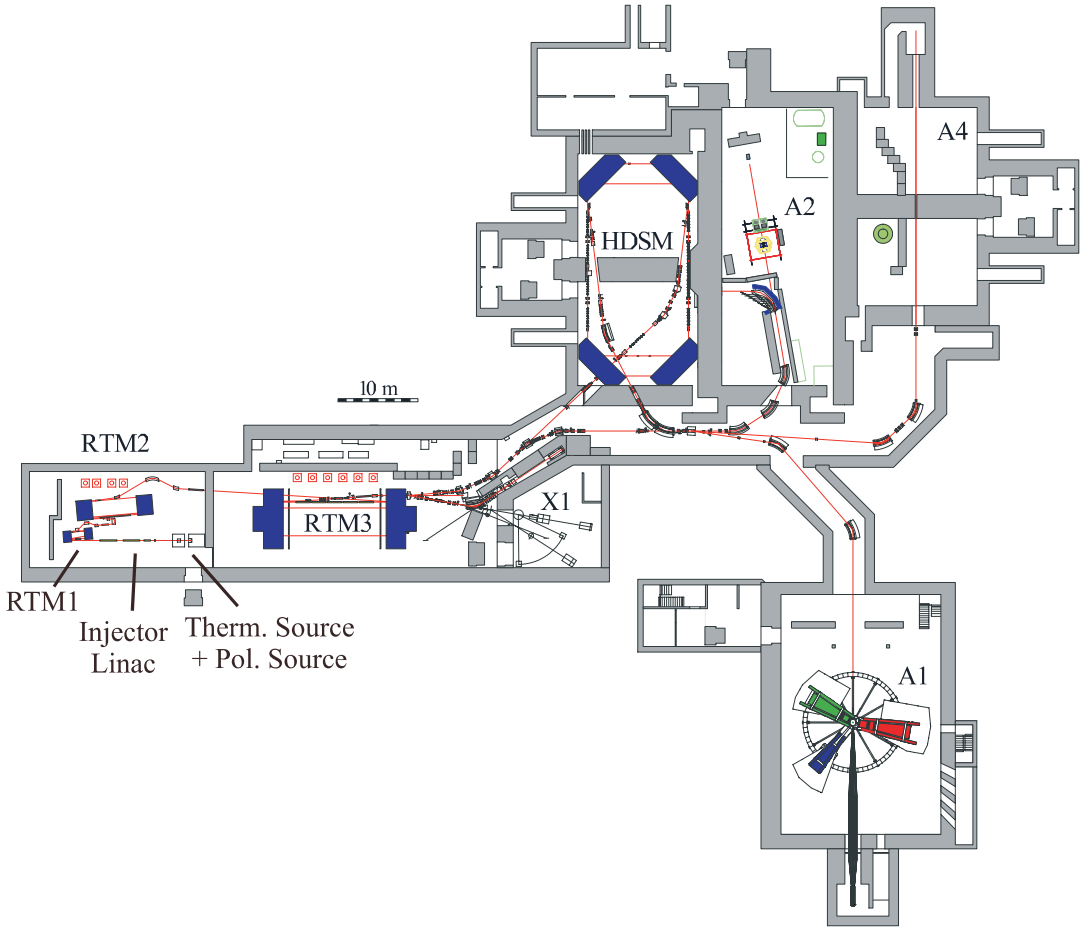

Figure 3.1: The floor plan of the accelerator and the experimental halls in the Institut für Kernphysik, in Mainz. The experiment was carried out in the A2 hall, using the electron beam from MAMI-B (RTM1, RTM2, and RTM3). The photon tagging spectrometer and the Crystal Ball/TAPS setup are shown in the A2 hall.

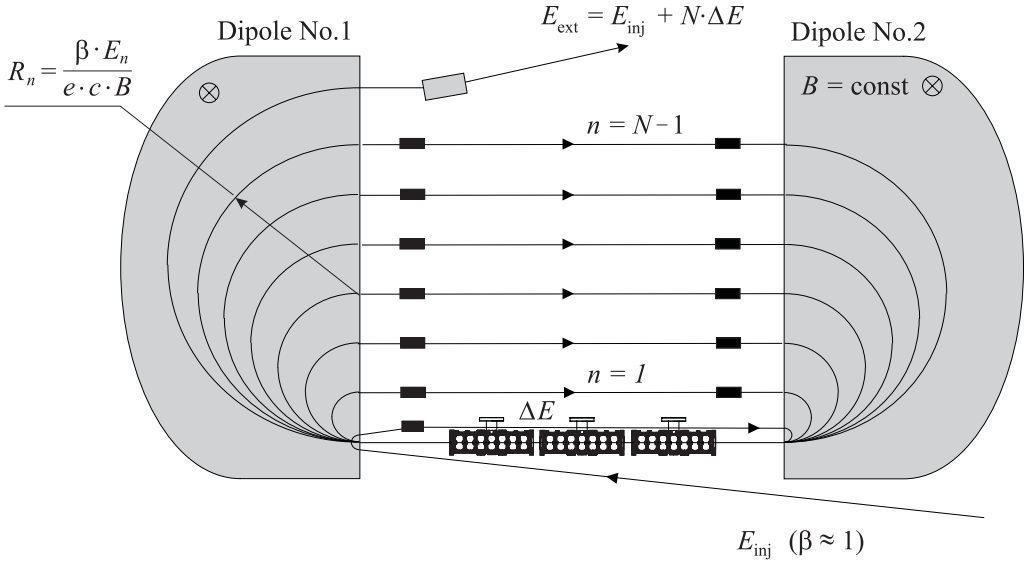

Figure 3.2: Schematic illustration of a race-track microtron (RTM) showing the single linac and the two bending magnets.

There are two possibilities to produce free electrons to be accelerated by a microtron. For production of unpolarized electrons, the cathode of an electron gun is heated to high temperature. Thereby the electrons tend to break free of their atoms and dwell near the surface of the cathode. In order to produce polarized electrons, a laser beam is fired at a GaAs(P) crystal. Through the photoeffect, polarized electrons escape from the crystal. In the experiments with η mesons, unpolarized electrons were used. Due to the voltage applied between the cathode and an anode, the electrons are accelerated and escape through the hole in the anode into the buncher, where they are packed into bunches using microwaves. The linac, which is in principle an extension of the buncher, continues accelerating the electrons and compacting them into tighter bunches. At MAMI, after leaving the linac, the electrons have an energy of 3.97 MeV. Further acceleration proceeds in the cascade of the three RTMs.

The initial RTM1 of MAMI first operated in 1975 and is now used as an injector for RTM2. In this configuration the accelerator first operated in 1983 as MAMI-A. Since 1990, RTM2 acts as an injector for RTM3 (see fig. 3.3). The three stages work together as MAMI-B (see table 3.1). RTM3 takes electrons of energy 180 MeV and accelerates them to 855 MeV in 7.50 MeV steps by 90 recirculations. It can produce a beam of any energy starting from 180 to 855 MeV in 15 MeV steps. Later the MAMI staff raised the maximum beam energy to 883 MeV. This was achieved by slightly increased dipole magnetic field and slightly higher energy gain per turn. The physical geometry of the microtrons has not been changed. In the experiment described in this work a beam of energy 883 MeV was used.

Due to the working frequency of 2.45 GHz of the linac, the time difference between the electron bunches is $\approx$ 400 ps. Therefore, for an experiment with typical time

Figure 3.3: The 3rd race-track microtron (RTM3) of MAMI-B. Each of the two bending magnets weighs 450 t.

resolution of 1 ns, the beam can be considered as continuous. Thus, the duty factor of the MAMI accelerator can be estimated as 100%. Such a beam is ideal for coincidence experiments like one being described in this thesis.

	RTM1	RTM2	RTM3
Injection energy	3.97 MeV	14.86 MeV	180/186 MeV
Extraction energy	14.86 MeV	180 MeV	855.1/883.1 MeV
Number of turns	18	51	90
Energy gain per turn	0.599 MeV	3.24 MeV	7.499/7.744 MeV
Magnetic field	0.1026 T	0.555 T	1.2842/1.3260 T

Table 3.1: Main parameters of the three race-track microtrons of MAMI-B [Jan06, Jan06a]. The maximum extraction energy can be increased up to 883 MeV without changing the geometry of the microtrons.

3.2 Photon tagging facility

The high energy photons for the experiment are produced with the Glasgow-Mainz photon tagging facility (tagger). The photon tagger consists of a thin foil or crystal radiator (a 100 μm thick diamond radiator in the present experiment), and a large dipole magnet [Ant91] with a focal-plane detector system [Hal96]. The setup is presented in fig. 3.4. When an electron of incident energy E_0 generates a Bremsstrahlung photon of energy E_γ in the radiator, the degraded electron has energy $E_{e^-} = E_0 - E_\gamma$ (the recoil energy of the nucleus involved can be neglected). The electrons, which have not radiated, are deflected in the magnetic field of the spectrometer into a beam dump, where the total beam charge is recorded. The degraded electrons have less momentum and are deflected into the focal plane, where they are detected in an array of plastic scintillators (ladder). Meanwhile the associated photons pass into

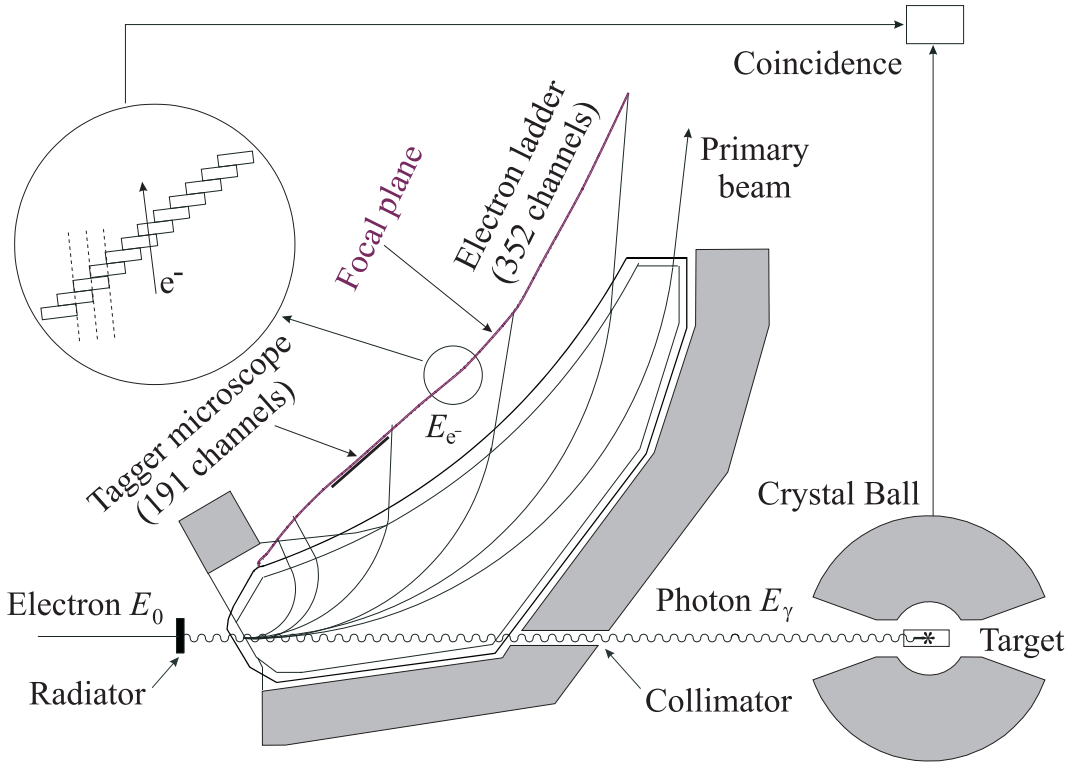

Figure 3.4: The top view of the tagger for producing Bremsstrahlung photons. The experimental detector (Crystal Ball) is shown not to scale. The tagger microscope, a high resolution focal-plane detector [Rei06], was positioned close to the focal plane covering channels 53-83 of the main detector array.

a separate experimental area and induce reactions in the experimental target. The number of photons available for inducing reactions is proportional to the number of electrons detected in the tagger, however, the photon flux at the target is reduced by collimation of the photon beam at the spectrometer exit. The photon energy can be determined using

$$E_\gamma = E_0 - E_{e^-}, \tag{3.1}$$

with the incident electron beam energy E_0, measured in the 3rd race-track microtron of MAMI-B (see section 4.5), and the tagging electron energy E_{e^-} measured in the tagger. The timing coincidence between the experimental detector and the focal-plane detector is required for correlation of the observed reaction with the tagged photon. Since the tagging electron is detected long before any reaction product, some signal delay is introduced into this arm of the system.

The focal-plane detector system [Hal96] is an array of 353 plastic scintillators of size approximately $2\,\text{cm} \times 8\,\text{cm} \times 0.2\,\text{cm}$. In order to reduce the background, the array is designed in such a way that each scintillator overlaps with both of its neighbors by about 1/2, so that any true tagging electron should hit two neighboring scintillators, which are examined for a coincidence between them. Therefore, the tagger has 352 tagging channels. At a primary incident beam energy $E_0 = 883\,\text{MeV}$,

the tagger can cover tagged photons of energies in range from $E_\gamma = 42\,\mathrm{MeV}$ to $E_\gamma = 820\,\mathrm{MeV}$ with an energy resolution of $\approx 2\,\mathrm{MeV}$. The maximum total counting rate of the tagger is determined by the channel with the highest rate. Due to the $1/E_\gamma$ behavior of the Bremsstrahlung energy distribution, the highest count rates occur in the lowest photon energy channels. In order to increase the total counting rate of the tagger for the η production experiment, only the first 80 channels, corresponding to the photon energy range from 682 MeV to 820 MeV, were enabled. This allowed a higher electron beam current and higher photon counting rate in the energy range of interest (η production threshold is $E_\gamma \approx 707\,\mathrm{MeV}$). During production running this rate was of the order of $10^5\,\mathrm{s}^{-1}\,\mathrm{MeV}^{-1}$. Since the energy resolution of the ladder is much greater than the intrinsic resolution of the spectrometer (100 keV [Hal96]), the scintillators lie not in the focal plane itself, but on a parallel curve at a distance of about 41 mm from it [Hal96]. This has little influence upon the energy resolution of the ladder, yet leaves space to mount an additional device with higher resolution at the true focal plane such as the tagger microscope described in section 3.3.

Photon flux

For the precise determination of the cross sections it is necessary to know the exact number of tagged photons in the photon beam, which is incident on the target during the experiment. This photon flux is also determined with the tagger. For this purpose each of the 352 channels has a scaler, which counts the total number N_{e^-} of the electrons detected in the channel. But not all of the Bremsstrahlung photons produced at the radiator reach the target because of collimation at the tagger exit. Thus, the number of photons passing into the experimental area, $N_\gamma(i)$, is less than the total number of the electrons, $N_{e^-}(i)$, counted in the scaler of tagger channel i. The ratio of the two numbers, known as the tagging efficiency $\varepsilon_{\mathrm{tagg}}(i)$, depends on the photon energy $E_\gamma(i)$, *i. e.* on the tagger channel number, i:

$$\varepsilon_{\mathrm{tagg}}(i) = \frac{N_\gamma(i)}{N_{e^-}(i)} < 1, \tag{3.2}$$

In order to determine the absolute value of the tagging efficiency, a large volume Pb-glass detector is driven into the photon beam. It has almost 100% efficiency for registering high energy photons. $N_\gamma(i)$ is determined by counting the photons in coincidence with the electrons, and $N_{e^-}(i)$ is the total number of counts in the corresponding scaler. Such measurements are performed regularly during the experiment with very low beam current to avoid damage to the Pb-glass detector, large dead-time, and random background counts.

It is also important to know that the photon beam spot is contained within the target diameter, so that all photons pass through the target. Since the photon beam is collimated at a distance of $\approx 2.5\,\mathrm{m}$ downstream from the radiator with a 3 or 4 mm diameter collimator, and the target is located at a distance of about 9 m from the radiator. The diameter of the beam spot at the target is less than 15 mm, comfortably smaller than the 40 mm target diameter.

Figure 3.5: Finished tagger microscope detector assembly without black plastic wrapping.

3.3 Tagger focal-plane microscope detector

The tagger focal-plane microscope detector [Rei99, Rei06], shown in fig. 3.5, is a focal-plane detector array developed to improve the energy resolution of the tagged photon flux in the Glasgow-Mainz photon tagging spectrometer over a movable energy range of width about 60 MeV. It can be placed in the 5 cm gap between the tagger exit window and the main detector array. A schematic view of the focal-plane gap of the spectrometer, where the microscope is installed, is presented in fig. 3.6. The figure shows how an electron leaves the vacuum box of the tagger, passes through the 1 mm aluminum protection window, through the 2 mm thick scintillator strips of the tagger microscope, and finally the 2 mm thick scintillators of the main focal-plane detector array.

The tagger microscope consists of 96 scintillator strips (3 mm wide, 2 mm thick, and 23.5 cm long), wrapped in aluminized mylar foil and directly connected to 6 Hamamatsu 16-channel multi-anode photomultipliers (a modification of H6568 model). The scintillator strips and the photomultiplier tubes are mounted on a compact frame, which can be inserted at any location along the tagger focal plane corresponding to the photon energies between 150 MeV and 735 MeV. The strips make a 30° angle with the focal plane (see fig. 3.7). The distance between neighboring strips is 4 mm, so that each single strip overlaps with 1/3 of its neighbor. Since, in the software, the overlaps are treated as separate channels, the tagger microscope has in total 191 detector channels giving resolution of about 300 keV.

For the η mass experiment the detector was positioned so that it covered the region around the η photoproduction threshold ($E_{\text{thr}} \approx 707\,\text{MeV}$) from $E_\gamma = 674\,\text{MeV}$ to $E_\gamma = 730\,\text{MeV}$ at an electron beam energy $E_0 = 883\,\text{MeV}$ and overlapped with the main focal-plane detector channels 53-83. At this position the tagger microscope had a resolution of about 290 keV, which is 6 times better compared to the 1.8 MeV resolution of the main detector array in this region. This allowed investigation of η photoproduction near threshold.

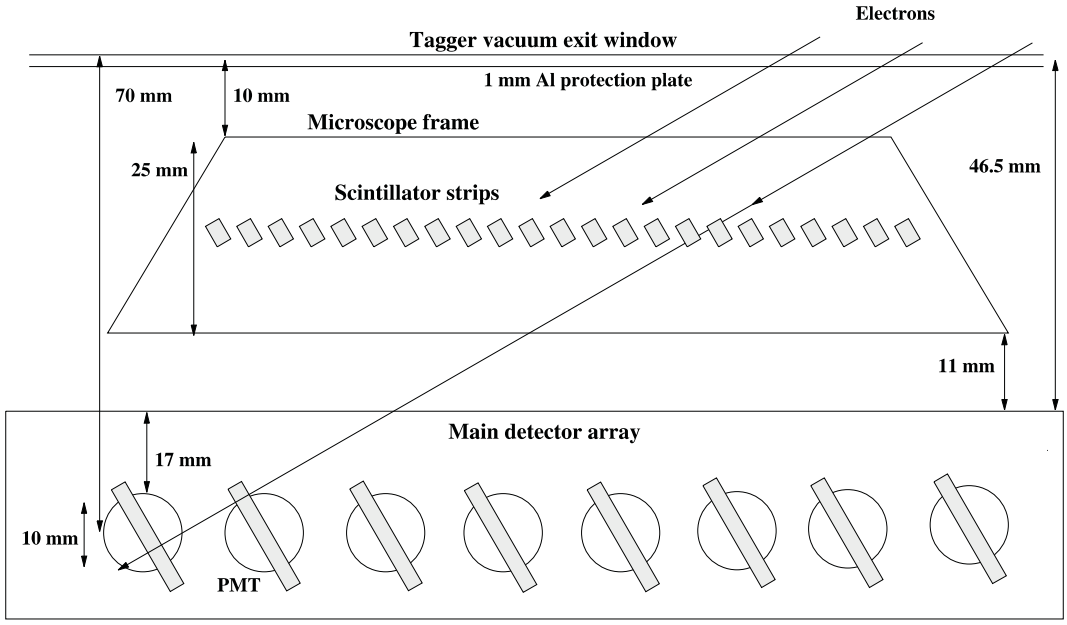

Figure 3.6: Schematic illustration showing the location of the tagger microscope in the gap between the exit window of the tagger and the main detector array [Rei06].

Microscope detector channel

The microscope detector channel is defined in the software in the following way: if a single strip $n = 0..95$ showed a signal, and there were no hits in the neighboring strips within the timing resolution, then the hit is written to the detector channel $2n$ (single-hit channel); if two neighboring strips n and $n+1$ showed a signal within the timing resolution, then a hit is written to the detector channel $2n+1$ (double-hit channel). In this way the 191 microscope channels are defined. However, if the trajectory of a tagging electron is not normal to the 3 mm face of the scintillator strip, the single- and double-hit channels are not of the same width. A typical hit distribution pattern, recorded during the experiment, is shown in fig. 3.8. It can be seen that the single-hit channels counted about 3 times more hits than the double-hit channels. From the geometry in fig. 3.7 one can show that the double- (D) and single- (S) hit projections (in mm) on to the focal plane are given [Rei06] by

$$D = 4 - S\,, \tag{3.3}$$

and

$$S = 8 - \frac{3}{\sin\alpha} + \frac{A \cdot \tan\delta}{\tan\alpha + \tan\delta}\,, \tag{3.4}$$

where

$$A = \frac{3}{\sin\alpha} \mp \frac{2}{\cos\alpha} \pm \frac{2\,p \cdot \cos\delta}{\cos\alpha}\,, \tag{3.5}$$

and $\alpha = 30^\circ$ is the angle between the normal to the front face of the strip and the focal plane, and $\alpha + \delta$ is the angle, which tagging electron trajectory makes with

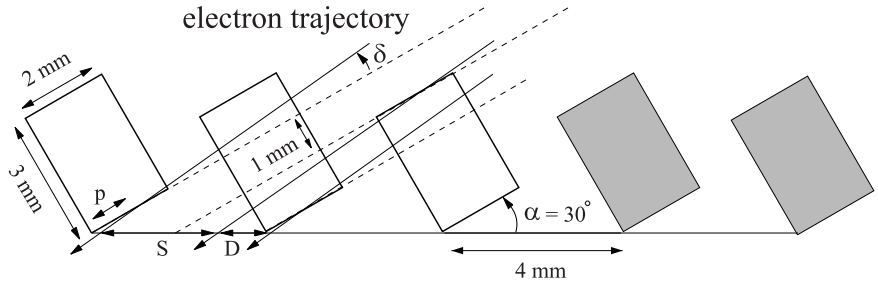

Figure 3.7: Geometry of the microscope detector channels. If the electron trajectory is not normal to the front face of the strips ($\delta > 0°$) then the even (single-hit) and odd (double-hit) channels are not of the same width.

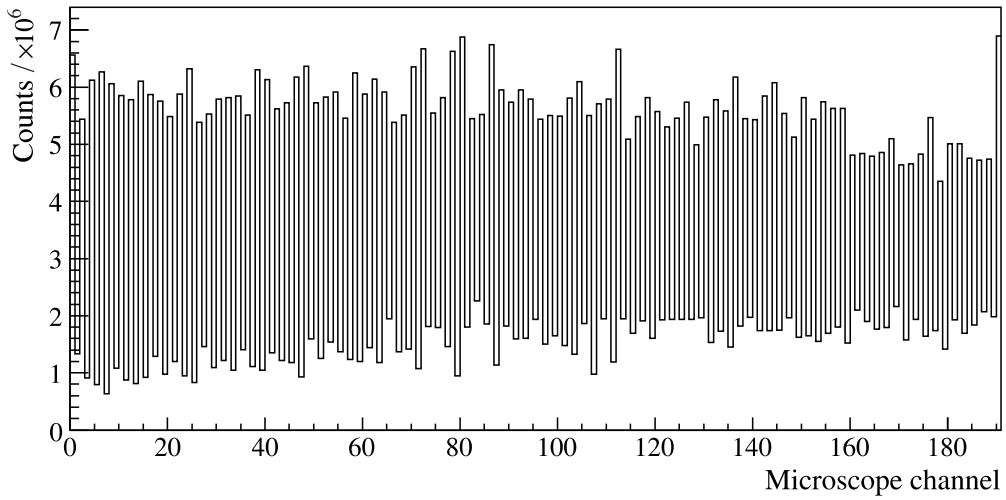

Figure 3.8: Microscope channel hit distribution pattern observed during the experiment with the electrons produced by Bremsstrahlung in a diamond radiator.

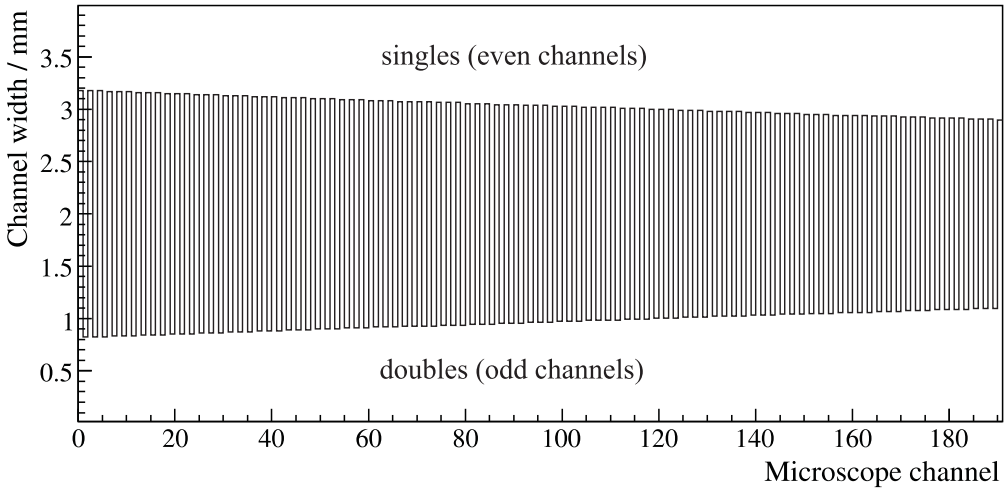

Figure 3.9: Calculated width of the microscope channels based on the single-/double-hit geometry for incidence angles $\alpha + \delta = 41.5°$ at microscope channel 0 smoothly changing to 38.1° at microscope channel 190.

the focal plane. In equation (3.5) the upper (lower) signs apply when δ is greater (less) than zero. In deriving these equations it was assumed that any path traversed through a scintillator strip greater than length p will lead to an output signal above the discriminator threshold. In our configuration the angle $\alpha + \delta$ is 41.5° at strip 0 smoothly changing to 38.1° at strip 95. The projected width of the microscope channel from the above equations is plotted as a function of the microscope channel number, i, in fig. 3.9 assuming $p = 0.75\,\text{mm}$. The number of counts in the channel should be proportional to the width of the channel, thus, one can see that the behavior of the channel width, calculated with equations (3.3) - (3.5), plotted in fig. 3.9, shows similar shape as the experimental hit distribution pattern plotted in fig. 3.8. The differences may be because of slight geometrical imperfections in strip alignments and in the threshold settings, which result in slightly different detection efficiency and p values for different strips.

Photon flux

As mentioned in the previous section, the flux of the photons $N_\gamma(i)$ of energy $E_\gamma(i)$ incident on the experimental target, which is important for determination of the cross sections, is determined by counting the total number of electrons, $N_{e^-}(i)$, detected by the i-th electron scaler:

$$N_\gamma(i) = N_{e^-}(i) \cdot \varepsilon_{\text{tagg}}(i)\,. \tag{3.6}$$

Each of 352 channels of the main detector array has a scaler, which counts the total number of electrons, $N_{e^-}(i)$, detected in the channel i. The tagger microscope strips are also connected to such scalers, however, the number of electrons counted by the scalers is prone to some background. In the main detector array the background problem is solved by requiring hardware coincidence between the two neighboring elements. In the tagger microscope electronics this requirement is not demanded, and background events (thermal emission, activation *etc.*) in the tagger microscope are significant at low count rates, such as during the tagging efficiency measurements. The procedure of the photon flux determination with the tagger microscope is described in section 4.7.3.

3.4 Liquid hydrogen target

For this round of the experiments with the Crystal Ball detector at MAMI a liquid hydrogen target was used (fig. 3.10). This target system was used previously with the DAPHNE detector [Ahr00] with a different target cell. In order to keep the detector acceptance free from heavy materials, a new shorter cell was constructed. The shorter cell allows more accurate determination of the reaction origin (vertex position) within the target cell. The target is made of the cylindrical kapton cell, which at temperature of 21 K has a length of 4.76 cm and a diameter of 40 mm

Figure 3.10: The liquid hydrogen target without wrapping.

[Tho07]. The walls of the target are made of 125 μm thick kapton. The cell is wrapped by 8 layers of super isolation foil, made of $\approx$ 8 μm mylar and $\approx$ 2 μm aluminum. In order to prevent ice growing on the target cell, an additional 25 μm thick kapton cylinder was installed over the isolation foil.

In the beginning all hydrogen for the experiment was kept in a tank in a gaseous state under a pressure of 1390 mbar and at a constant temperature of 21 K. A cooling machine brought the cooling gas (^{4}He) to a temperature of 17 K, which was sufficient to liquefy some of the hydrogen. In the normal working state, about 25% of the hydrogen was liquefied, and the pressure in the tank decreased to 1080 mbar.

3.5 Detector system

With the protons at rest in the hydrogen target and the photon energy information, obtained from the photon tagging spectrometer, the input of the photoproduction reaction is kinematically defined. The reaction products are identified with different detector systems. The detectors allow measurement of the directions and energies of the emitted particles so that the full 4-vectors can be determined.

3.5.1 Crystal Ball photon spectrometer

The Crystal Ball photon spectrometer (CB) has a spherical form with an outer radius of about 66 cm and an inner cavity of radius about 25 cm. The design is based on the geometrical form of an icosahedron, whose 20 triangular faces (major triangles) are divided into 4 minor triangles. Each of the 4 minor triangles are divided into 9 triangular faces. Such a form has 720 triangular faces in total, but, due to the holes for the beam, the CB consists of 672 crystals (see fig. 3.11 and fig. 3.12) and covers 94% of the solid angle. The crystals are not exactly identical (11 slightly different shapes), but each of them is a 40.6 cm long truncated triangular pyramid (fig. 3.11 right). The crystals are mounted on two stainless steel frames, so that the detector is divided into two hemispheres. The inner shell of the frames is made of 3 mm (0.18 radiation lengths) thick steel. The upper hemisphere can be moved up and down in order to have access to the central region of the detector. The gap between the 1.6 mm thick stainless steel disks of the housing frame, where the crystals

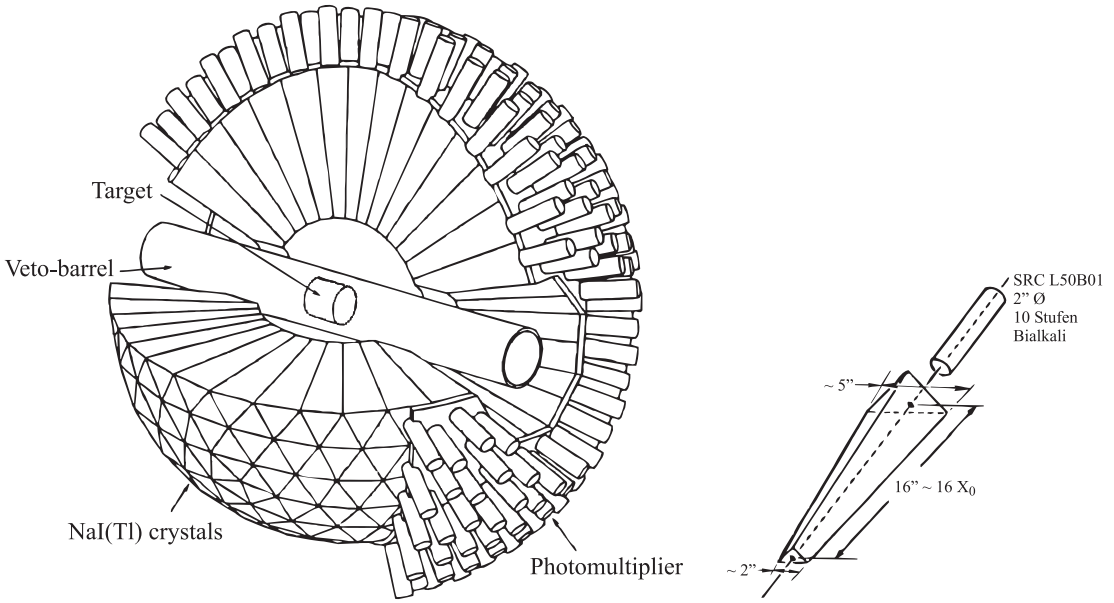

Figure 3.11: The Crystal Ball photon spectrometer with cut-away section giving a view of the inner detectors. The inset shows the geometry of a single NaI crystal.

are mounted, can be reduced down to a few millimeters. The outer shell of the CB is made of a 2.5 mm thick aluminum. Each crystal is read out with a photomultiplier, therefore, the shell has 672 glass windows on which the photomultipliers are mounted. Both hemispheres are vacuum sealed in order to improve the stability and decrease crystal damage since they are extremely hygroscopic. The hemispheres in their turn are mounted in a bigger frame, which is designed so that the CB can be moved in all directions in order to align the center of the CB with the beam.

The 672 crystals of CB are made of the inorganic scintillator NaI(Tl). A single crystal (fig. 3.11 right) is 40.6 cm long and has triangular pyramidal form, cut from both sides, and is optically isolated by wrapping in reflective paper and aluminized mylar. Such a crystal can stop protons with energy of up to 425 MeV. The thickness of the crystal is about 15.7 radiation lengths, and typically 98% of all the deposited energy from the electromagnetic shower, produced by a photon or electron, is contained within a 13 crystals cluster.

SRC L50B01 photomultipliers are used in the CB. They have a diameter of 5.1 cm and are mounted on the windows of the CB outer shell. The photomultiplier base chains are fitted with variable resistors between the 3rd and 4th dynodes. These are accessible from outside the photomultipliers and were adjusted to match the gains of the CB elements. This matching allows a calibration for the energy sum trigger used in the experiment – see section 3.6.4.

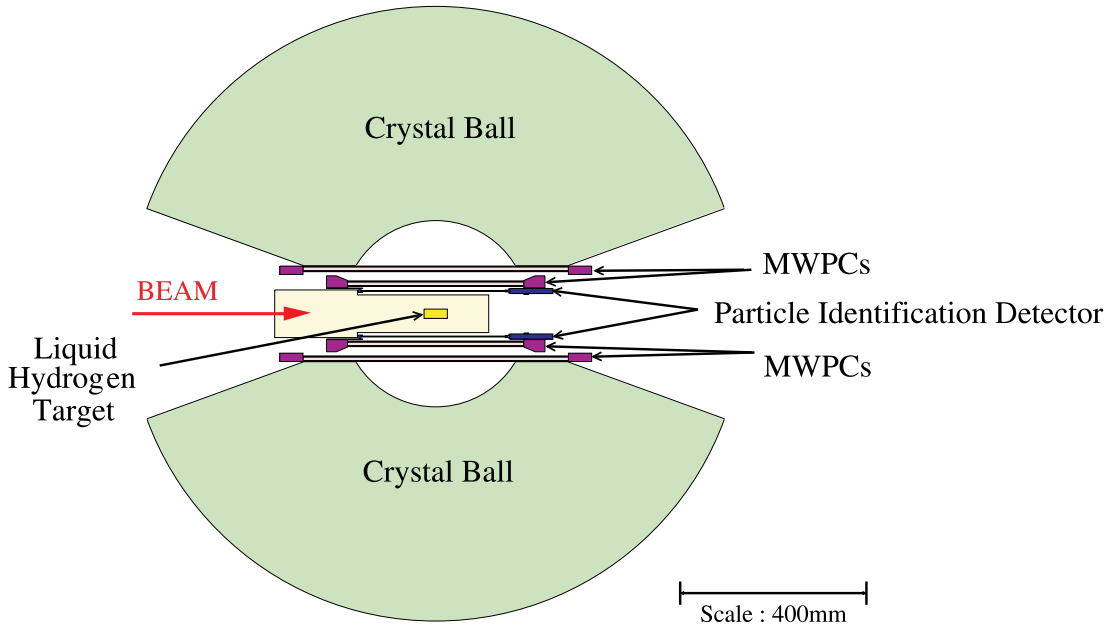

Figure 3.12: Transverse view of the Crystal Ball at MAMI showing the inner detectors (MWPCs, PID) and the liquid hydrogen target.

3.5.2 Particle identification detector

The particle identification detector (PID) is a detector, based on organic scintillator, intended to identify particles. The detector was developed at the Universities of Glasgow and Edinburgh for this round of the experiments. It is a cylinder of 10 cm radius, consisting of 24 scintillator strips, 31 cm long, 13 mm wide, and 2 mm thick (see fig. 3.13 and 3.14). As there was no space available between the multi-wire proportional chambers (MWPCs) and the CB, the PID was designed to fit between the target and the inner MWPC. The scintillator used is EJ204 which has a short

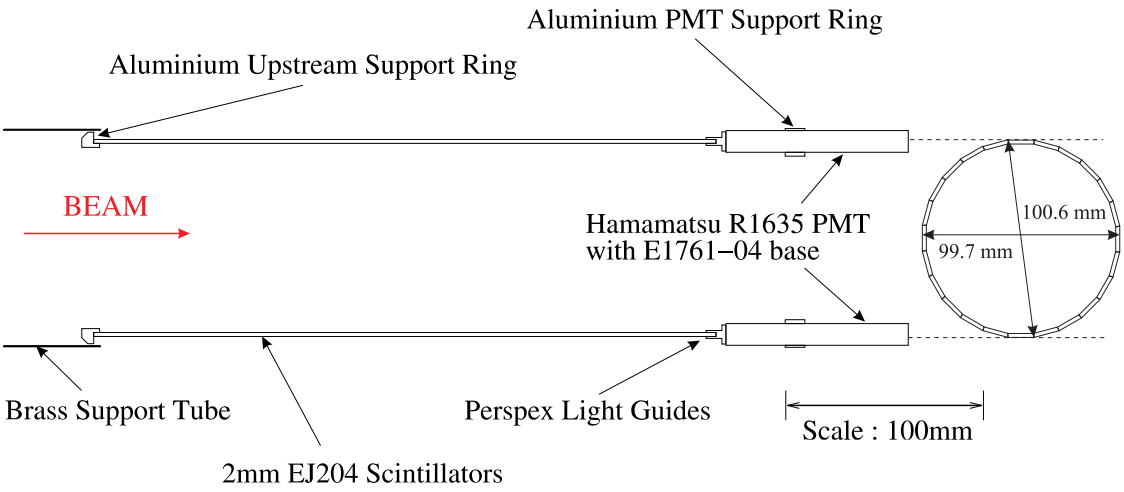

Figure 3.13: Particle identification detector (PID).

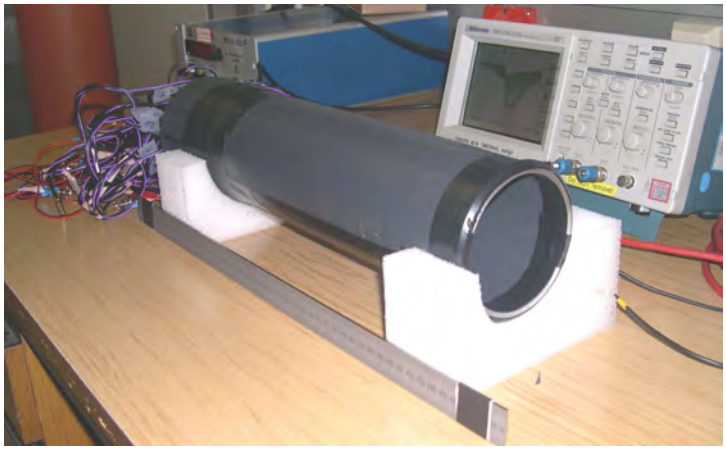

Figure 3.14: Finished particle identification detector (PID) assembly before installation.

rise time. More details about design and construction of the PID can be found in [Dow07].

The PID serves as a veto to separate photons from charged particles in the CB and to identify protons and charged pions. For the charged particles it provides identification of different particle species by comparison of the energy deposited in the CB and the energy deposited by the same particle in the PID. The lighter particles (electrons, pions) deposit a smaller fraction of their energy in the PID. By plotting the energy deposited in the PID versus the energy deposited in the CB (see fig. 4.4), different particle types can be distinguished.

3.5.3 TAPS forward angle detector

The detector TAPS [Nov91] is configured for our experiment as a forward angle spectrometer consisting of 510 BaF_2 elements (see figures 3.15 - 3.17). It is positioned at a distance of 173.3 cm from the center of the Crystal Ball. Since the Crystal Ball was originally designed for colliding beam experiments, there is a large hole in the forward region of the Crystal Ball. Due to the Lorentz boost from the center-of-mass system of the incident photon and the target proton, most reaction products in the present experiment are emitted in the forward direction. Therefore, TAPS is used to detect particles in the polar angle range between $\theta = 0°$ and $\theta = 20°$.

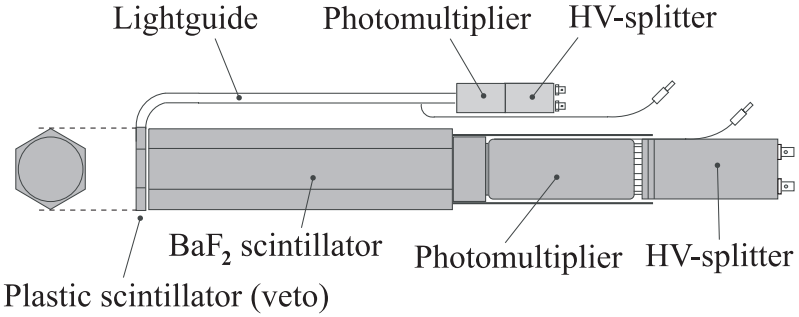

Figure 3.15: Structure of a single BaF_2 module of TAPS.

Figure 3.16: Single BaF_2 module of the TAPS spectrometer and a scintillator crystal.

A single element of TAPS is shown in fig. 3.15 and 3.16. Each TAPS element is a BaF_2 crystal of hexagonal cross section contained within a circle of 59 mm diameter and has a length of 25 cm, which corresponds to approximately 12 radiation lengths. The length is sufficient to stop 180 MeV $\pi^{\pm}$ and 360 MeV protons. Each element has an individual 5 mm thick plastic scintillator in front of the BaF_2 crystal, which is connected to a separate photomultiplier via a lightguide. These scintillators provide the possibility to distinguish between charged and neutral particles.

The scintillation light of the BaF_2 has two components with different response time, fast and slow. The fast component has a decay time of 0.76 ns, and the slow component a decay time of 620 ns. The various ionization densities of the particles influence the light output of the crystal in both components to a different extent. Thus, the selection of the particles by means of the pulse-shape-analysis (PSA) is possible. The very good time resolution (about 0.5 ns (FWHM)) of TAPS and

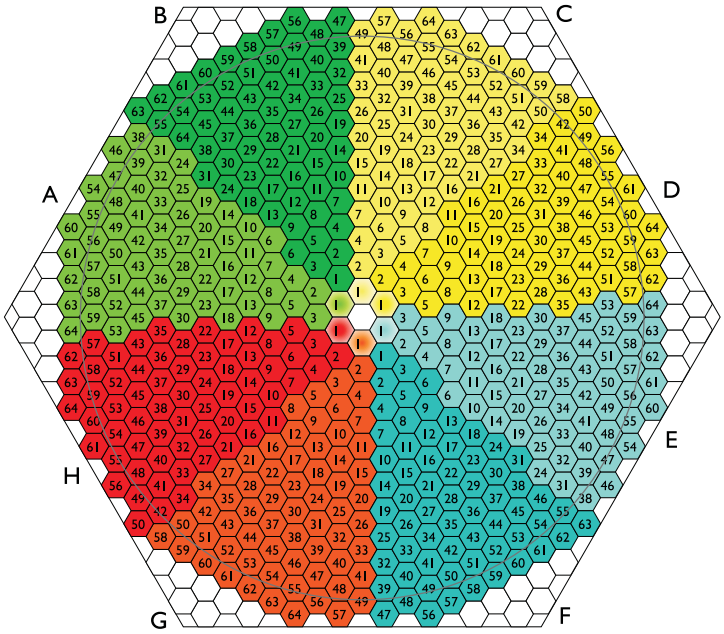

Figure 3.17: The forward detector TAPS as used with the CB at MAMI. The 510 BaF_2 crystals are numbered as shown and divided into 4 logical segments (A+B, C+D, E+F, G+H) for the cluster multiplicity trigger (see section 3.6.4).

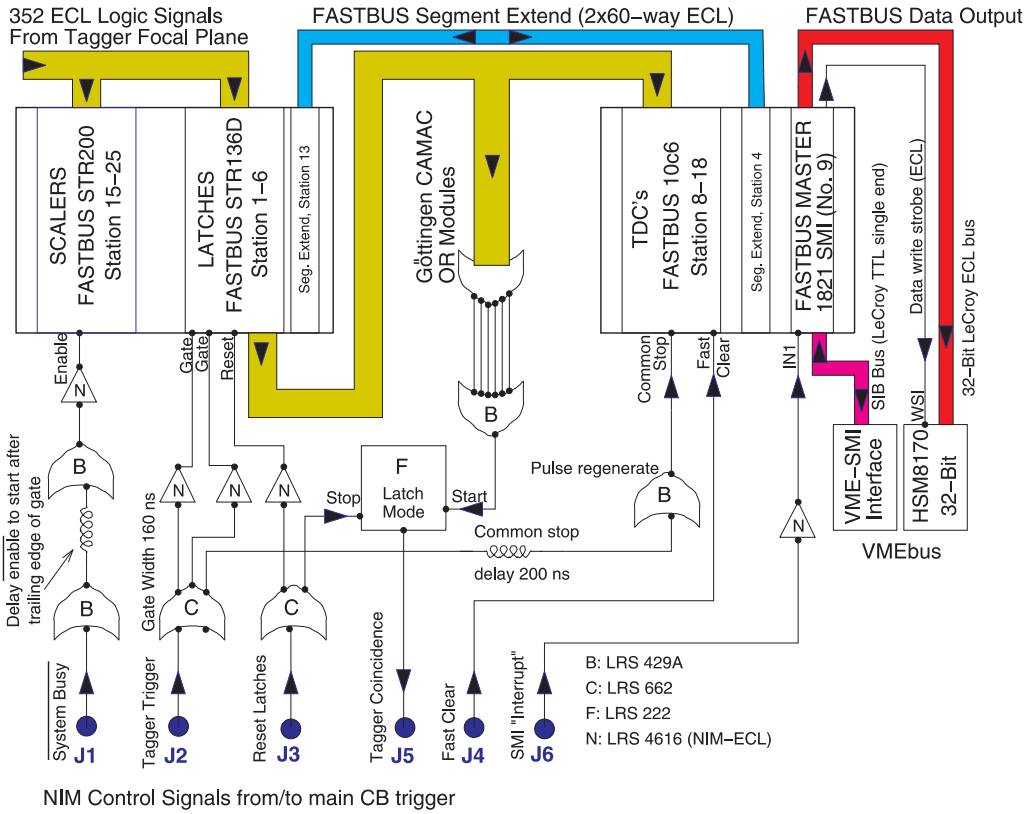

Figure 3.18: Tagger readout electronics. The connection J5, destined to establish coincidence between the tagger and the experimental trigger, is not used.

the relatively large distance to the target allows an efficient time-of-flight (TOF) measurement for further distinction of the particle type.

3.6 Detector electronics

The aim of the electronics is to read out the data from the photomultipliers and create the signal that initiates the readout. In the following sections, a description of the electronics of the experiment is presented. The tagger electronics are based mainly on FASTBUS[1] modules. Thereafter, the electronics of the Crystal Ball are described, in which the readout of the PID is integrated. Then follows a section about the TAPS electronics and finally the description of the experimental trigger. An overview of the conditions of the experiment closes this chapter.

3.6.1 Photon tagger electronics

The main focal-plane detector of the photon tagger consists of 353 scintillators, each of which half overlaps with both neighbors so that a tagging electron must always

[1]FASTBUS is a data acquisition system standard ANSI/IEEE STD 960-1986.

pass through the two neighboring scintillators giving 352 channels. Each scintillator is read out with an individual photomultiplier. In order to reject most of the background, the neighboring overlapping scintillators are operated in coincidence. The coincidence is made in a small electronics card mounted on the photomultiplier in which the signal is duplicated. One signal is discriminated with a low threshold, and the other with a high threshold. The first signal is used for timing, and the second one determines, if the signal is sufficiently large to result from an incident electron. The low threshold signal is delayed and effectively gated by the high threshold signal and then is sent to the next card, where a coincidence is demanded with the neighboring scintillator.

The logic signals from 352 tagger channels are fed to the main rack of the tagger electronics shown in fig. 3.18. The first stage of the main electronics system involves a delay of about 500 ns. Then the signals are delivered to FASTBUS scalers, which continuously count all incoming pulses from all channels. The counting process is interrupted only when the trigger electronics are busy and the data are being read out. The busy signal is generated in L1 (see fig 3.24) and is delivered to the tagger electronics over the connection J1. The tagger scalers are used to determine the total photon flux, which is necessary for determination of the cross sections.

Parallel to the scalers, the logic signals are delivered through a latch to TDC [2] units and to the logic OR of all 352 channels. The latch selects only signals in a 160 ns time window. The window is started by the L1 register of the experimental trigger via connection J2. The tagger signals within the time window are output from the latch and used to start the TDC units. The second arm of the J2 signal, additionally delayed by 200 ns, is used as common stop signal for the TDC units. Thus, it is possible to determine the time position of the incoming pulses within the time window. These time measurements produce spectra like that shown in fig. 6.1. The peak on the 160 ns wide background arises from the time correlated electron-trigger events. The background is produced by random tagger hits within the time window, which are not correlated with the event trigger.

The logic OR of all 352 channels is supplied to the main experimental L2 trigger logic unit. Optionally this signal can be combined with the experimental trigger to ensure that there is always a corresponding tagger signal for all of the experimental data readout, but this coincidence is not demanded in the experiments with the Crystal Ball. The readout of the data is performed by a FASTBUS master module via VMEbus[3].

Tagger microscope electronics

The tagger microscope is equipped with readout electronics independent from the main tagger detectors, and both can be employed simultaneously. The tagger microscope consists of 96 scintillator strips, which are read out by 6 16-channel multi-

[2] TDC stands for Time-to-Digital Converter.

[3] VMEbus is a computer bus standard ANSI/IEEE 1014-1987.

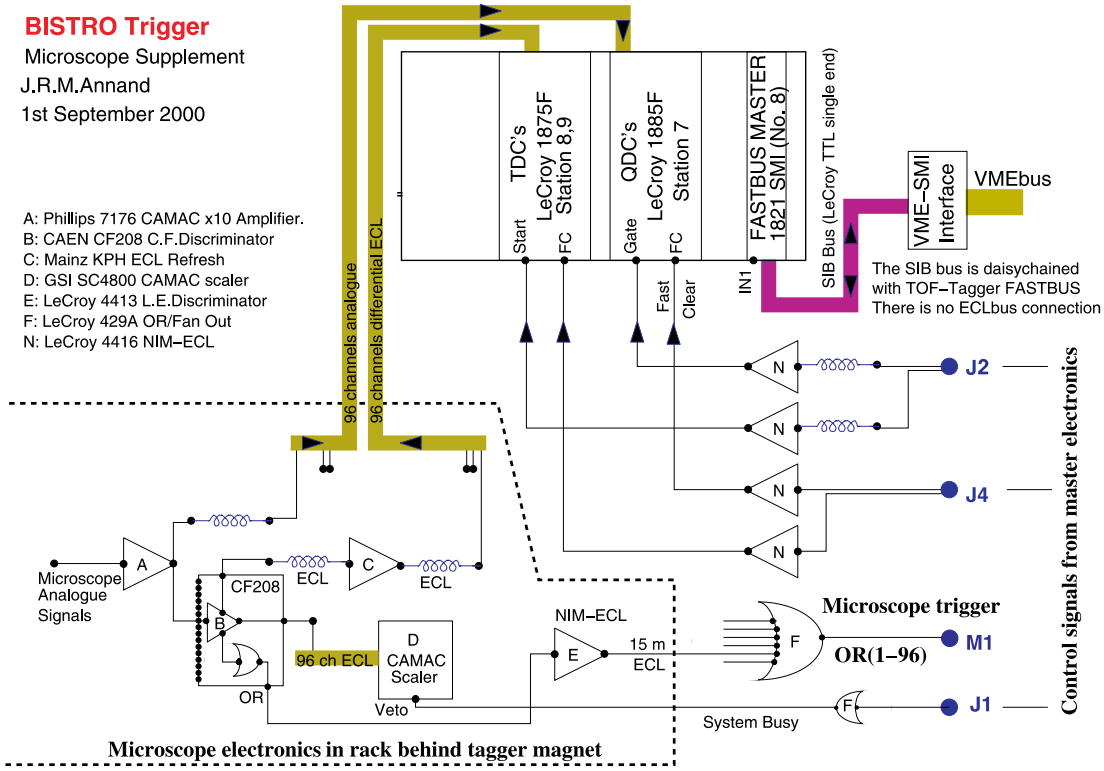

Figure 3.19: Readout electronics for the tagger focal-plane microscope detector.

anode photomultipliers. The electronics layout is shown in fig. 3.19. The 96 signals are amplified by a factor of 10 and duplicated. One signal is fed directly to a QDC [4] through a 400 ns delay. The other is connected to a constant fraction discriminator (CFD). The logic output of the CFD is delivered to the scalers, which continuously count all incoming pulses. This process is interrupted only when the busy signal from the experimental trigger is delivered via connection J1. Parallel to the scalers, the logic signal is delivered to a TDC and to the logic OR of all 96 channels.

The delayed analogue and logic signals are fed to the QDC and TDC cards in the main rack of the tagger microscope electronics. The QDC channel for each scintillator strip makes it easy to adjust the discriminator threshold at the start of the experiment and to monitor the gain of the device throughout the experiment. The logic signals provide the stop of the TDC units. In contrast to the main focal-plane detector, where the experimental trigger provides the stop signal for TDCs, in the tagger microscope electronics the trigger signal starts the TDCs.

3.6.2 Crystal Ball and PID electronics

A high event rate (a few kHz) is achieved in the Crystal Ball/TAPS setup at MAMI. Therefore, proper electronics, which can process such a rate, are installed. Mostly the electronics are based on the modules used in the COMPASS experiment and

[4] QDC stands for charge(Q)-to-Digital Converter.

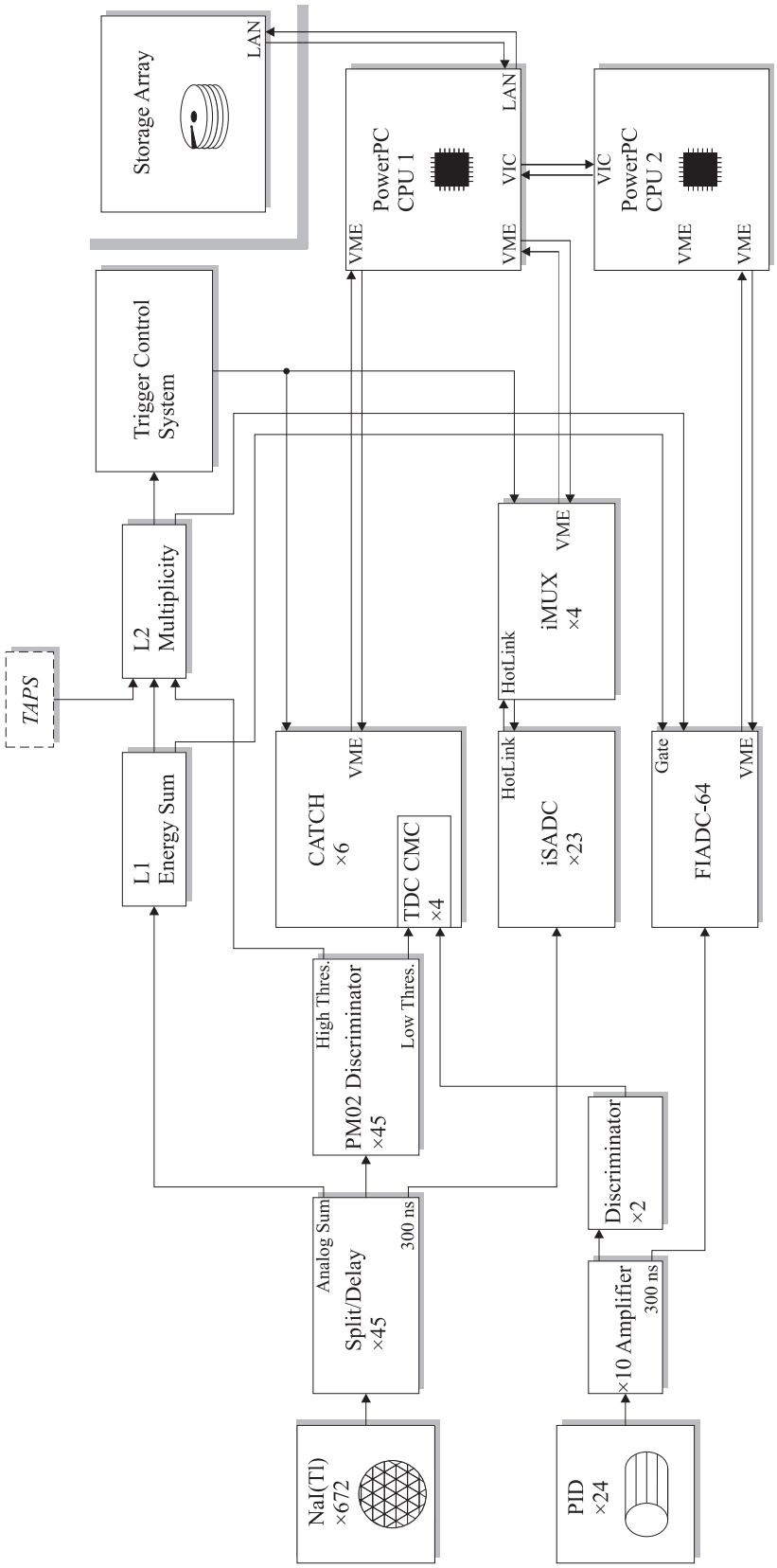

Figure 3.20: Overview of the electronics for the Crystal Ball experiment at MAMI.

in the WASA detector at CELSIUS. The PID uses the same TDC modules as are used in the CB electronics. The overview of the CB and PID electronics is shown in fig. 3.20.

Crystal Ball branch

The CB detector consists of 672 crystals supplied with 672 photomultiplier tubes (PMTs). The signals from the 672 PMTs are processed by the CB electronics. The 672 crystals are divided into 84 groups of 8 crystals (fig. 3.21). From symmetry considerations, the missing crystals in forward and backward directions of the CB are also numbered, making in total 720 channels in 90 groups. The signals from the PMTs are delivered to 45 Split/Delay modules. Here the groups of 8 channels are combined into groups of 16 channels, and each of the 45 Split/Delay outputs is split into three branches (fig. 3.20). One branch passes to the trigger electronics (see section 3.6.4); the signals from the other branches are connected to the 45 discriminators and via a 300 ns passive delay to 23 32-channel sampling ADC [5] modules. The second branch feeds PM02 16-channel dual threshold discriminators (a modified version of the PM98 Uppsala-designed discriminators from the WASA experiment, see [Mar01]). Each channel in these modules is equipped with two leading edge discriminators (MAX962 comparators), one with a low threshold and one with a high threshold. The signals, discriminated with the low threshold, are connected to the TDC cards, and the logic OR of the 16 high threshold discriminated signals passes to the L2 multiplicity trigger.

The TDC cards are read out with CATCH[6] modules, originally designed for the COMPASS experiment at CERN. Each TDC card is supplied with 4 TDC chips. They are free running 16-bit counters giving a channel to time conversion of approximately 117 ps per channel. The TDC cards are synchronized by a trigger control system (TCS) with one channel connected to the trigger. Each chip has a double hit resolution of some 20 ns without dead time, having a buffer for storing of up to 4 hits. To obtain the time of a TDC hit, the number stored in the reference TDC is subtracted from the number stored in the TDC of interest. The reference time is generated by the TCS using the L1 trigger signal.

The delayed signals from the splitter are fed to an array of 32-channel sampling ADC (i-SADC 108032) boards. The SADC boards continuously sample the analogue signals at a rate of 40 MHz. The boards are programmed to produce integrals of the input sample over three windows: the baseline integral of the sample before the scintillation pulse, the integral of the main body of the scintillation pulse, and the integral of the tail of the pulse. The timing for integration is derived from the experimental trigger. Use of these integrals reduces the volume of the data to be processed and allows subtraction of the pedestal (baseline integral). When the trigger pulse is received, the ADC looks in the multi-hit buffer and produces these

[5] ADC stands for Analog-to-Digital Converter.
[6] CATCH – COMPASS Accumulate Transfer and Control Hardware.

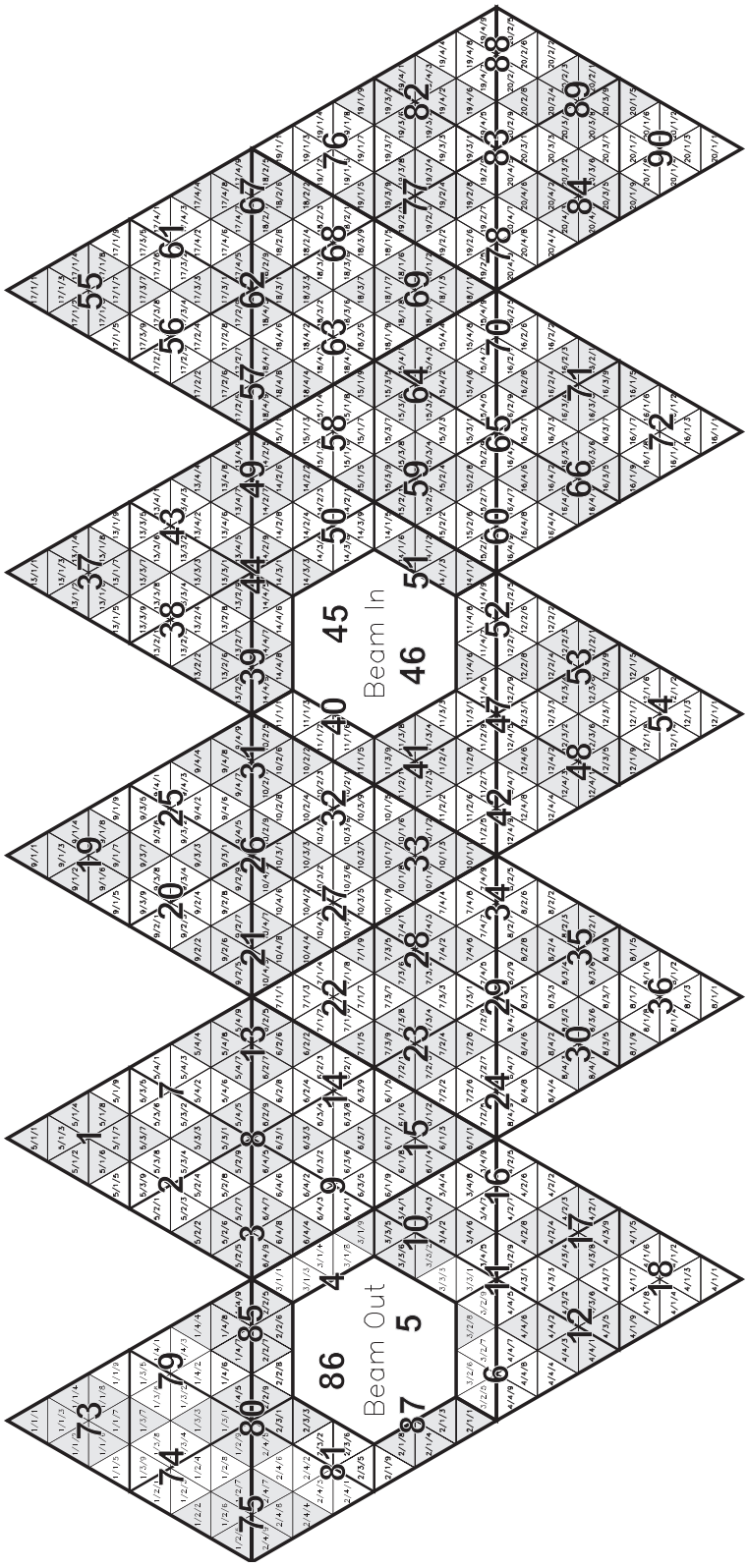

Figure 3.21: Projection of the Crystal Ball showing the numbering of the crystals. The areas marked with bigger numbers represent the groups of 8 crystals.

integrals for each channel. The pulses with amplitude greater than the baseline by a set threshold are read out. This threshold is set to approximately 0.5 MeV. The samples are processed and sent over an optical link (HOTLink[7]) to i-MUX8 readout modules. An i-MUX8 module can process the data stream from up to 8 SADC modules. It performs the following tasks:

- continuous combination of the 8 HOTLink data streams;
- combination of the TCS events with corresponding data from the detector;
- conversion of the data blocks into S-LINK[8] format;
- configuration of ADC units.

The TCS information passes through the optical fiber to the receiver, which is integrated in the module. Relevant information passes via the HOTLink to the SADC. The i-MUX8 modules are read out via VMEbus.

PID branch

The signals from the 24 scintillator strips of the PID are amplified by a factor of 10 and duplicated. One branch is fanned out to LeCroy 4413 leading edge discriminator modules. The discriminator output then passes to the CATCH TDC units. Another branch is fed to fast integrating ADC (FIADC) modules over a 300 ns delay. These modules were originally developed for the COMPASS experiment. If the event is not confirmed by the trigger within 300 ns after the conversion, the FIADCs throw the data away. The confirmation signal is built from the L2 trigger. Then the data are transferred to a computer (PC) over the VMEbus. The readout of the CB and PID data is performed with two PowerPC processors, which are synchronized with each other over a VIC[9] connection. The collected data are stored on the hard disks.

More detailed description of the single modules of the Crystal Ball and the PID readout electronics can be found in [Kra07], [Sch04], and [Unv04].

3.6.3 TAPS electronics

The readout electronics for TAPS are based on custom designed VME modules (CAEN V874A). Almost everything is implemented in a compact and fast extension board (fig. 3.22), which can perform digitization of the time, energy, and pulse shape data of four BaF_2 detectors at the same time. In the output the time and energy information is combined in one data stream.

The BaF_2 signal is discriminated via two leading edge discriminators (LED1, LED2) and one constant fraction discriminator (CFD). The discriminated signals

[7]HOTLink – high speed optical transceiver link.
[8]S-LINK – simple link interface, high-performance data acquisition standard.
[9]VIC – VME InterConnect.

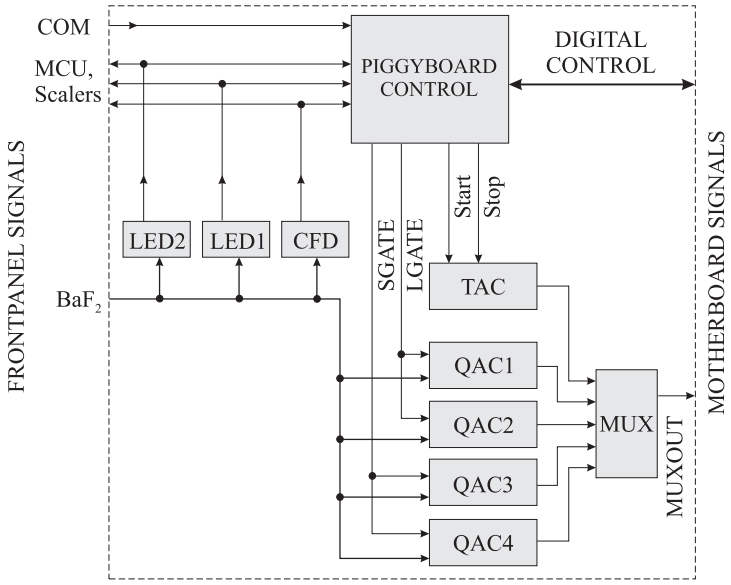

Figure 3.22: General block diagram of the readout board for one BaF_2 detector channel of the TAPS [Dre03].

pass to the scalers and TAPS multiplicity coincidence unit (MCU) as well as to the control of the extension board. The MCU serves for derivation of the trigger conditions, such as coincidences between BaF_2 modules or between photon and veto-detectors for identification of charged particles. No TAPS trigger was used in the η production experiment. In the experiment for determination of the magnetic moment of the Δ-resonance, TAPS contributes to the multiplicity trigger.

The CFD signal provides the start signal. The time measurement is stopped by the trigger signal, which serves as a common stop. For pulse-shape-analysis (PSA), the BaF_2 signal is distributed to the four integration circuits (QAC1 to QAC4). The integration of the slow and fast components is performed in parallel by 4 QAC [10] units. For this integration, two different time windows are produced, the short (20 ns) window (SGATE) to measure the fast component and the long (2.0 μs) window (LGATE) to measure the slow component. By comparison of the fast component with the total light output of the BaF_2, it is possible to distinguish between photons and nucleons. The pulses from the TAC (Time-to-Analog Converter) and 4 QAC units finally pass to the ADC of the extension board via a multiplexer. Further details about the TAPS readout electronics can be found in [Dre03].

3.6.4 Experimental trigger

In η photoproduction off the proton near threshold, the dominant reaction is single pion photoproduction. In order to avoid overwhelming the data storage with unwanted pion data, these events are filtered out already during the measurement by

[10] QAC stands for charge(Q)-to-Analog Converter.

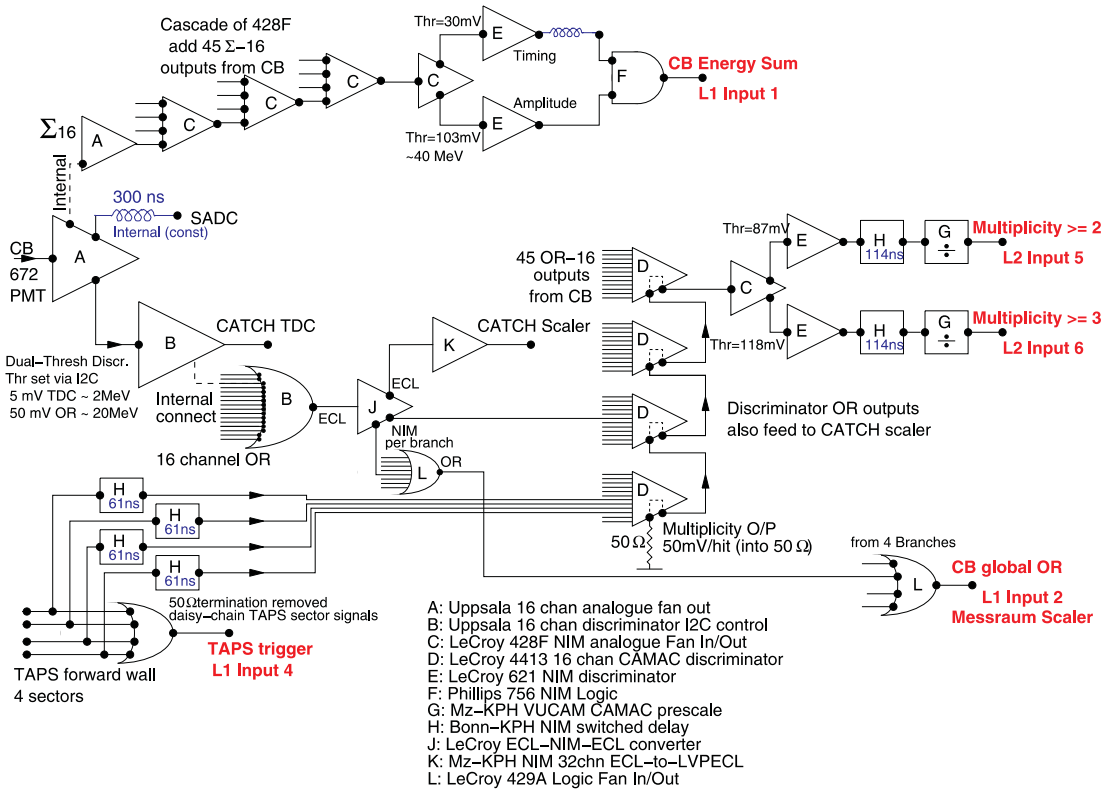

Figure 3.23: Scheme of the Crystal Ball energy sum trigger (L1) and the cluster multiplicity trigger (L2) electronics.

the trigger system, which fires on events of interest but not on most of the background. In the Crystal Ball a two-level trigger system is used, consisting of a 1st level energy sum trigger (L1) and a 2nd level cluster multiplicity trigger (L2). The L1 trigger is fast, while the L2 trigger allows more time for decisions to be made. An event that fires the L1 trigger starts the TDCs, gates the QDCs, and initiates the readout. However, the readout is aborted unless the L2 trigger also fires. If the L2 trigger did not fire, the TDCs and ADCs are reset, and the event is not stored. The L1 trigger is built from the Crystal Ball detector signals only, while the L2 trigger is built from the Crystal Ball and, if required, also TAPS signals.

Energy sum trigger

For the CB energy sum trigger (see fig. 3.23), the analogue sum of the signals from all NaI crystals of CB is built. The signals from the outputs of the 45 16-channel Split/Delay modules (A) are summed through the cascade of LeCroy 428F NIM analogue modules (C). At the output, rise time compensation is performed using two discriminators (E). In the η production experiment, the events with CB energy sum more than approximately 390 MeV are accepted.

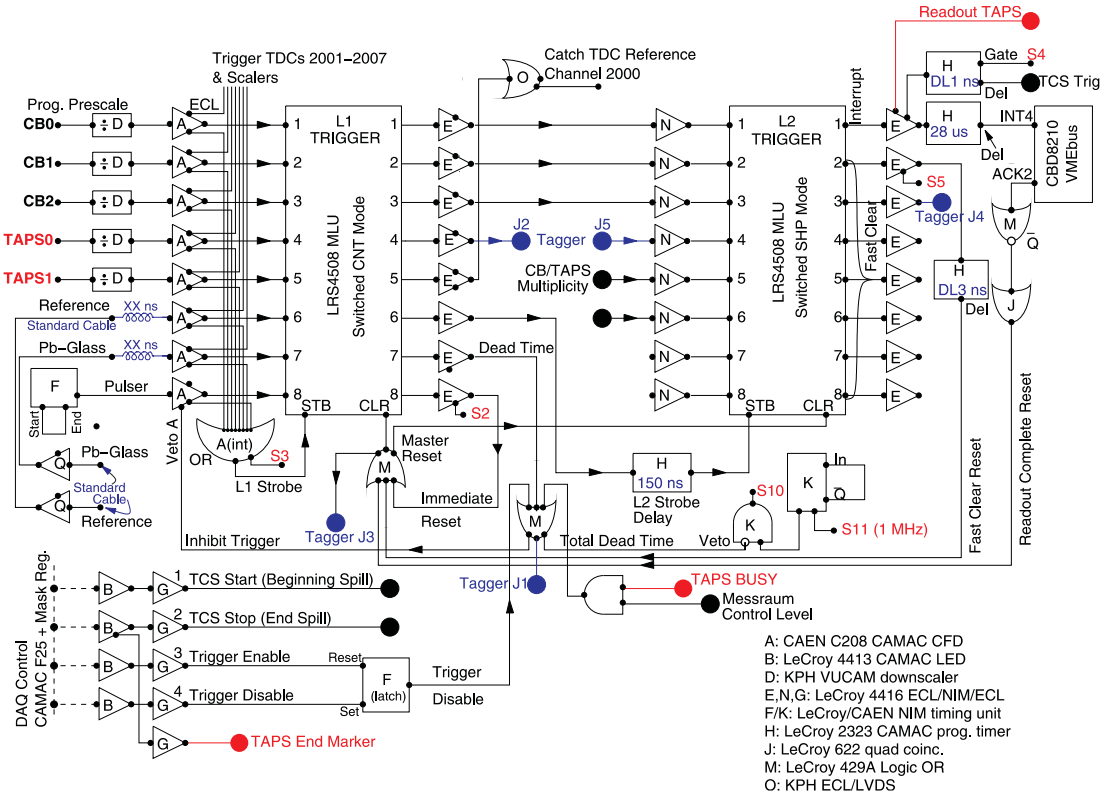

Figure 3.24: Scheme of the trigger register. The energy sum trigger (L1) and the cluster multiplicity trigger (L2) electronics.

Cluster multiplicity trigger

The scheme of the cluster multiplicity trigger is shown in fig. 3.23. For the cluster multiplicity trigger, the above mentioned outputs of the 16-channel Split/Delay modules (A) pass to the dual-channel discriminators (B). Each group of 16 channels corresponds to an area in the CB. The TAPS modules are divided into 4 groups of 127 or 128 crystals. From all channels within a sector, a logic OR is built. These $45 + 4 = 49$ logic OR signals are fed to the CAMAC discriminators (D). These four discriminators are connected in a chain, so that a sum of all signals is produced. Thus, the output signal is proportional to the number of hit areas in the CB and TAPS. In the LeCroy NIM analogue Fan In/Out module (C), the signal is duplicated and connected to the two discriminators. Here it is possible to set the multiplicity conditions by changing the thresholds. Cluster multiplicity conditions $M \geq 2$ and $M \geq 3$ are used in the η production experiment.

Trigger register

The scheme of the trigger register is shown in fig. 3.24. The trigger system is built on programmed memory registers (L1, L2). The registers assign each programmed input sample an output sample. The signal from the CB energy sum trigger passes

	η experiment	MDM experiment
Time period for η mass exp.	December 8-13, 2004	January 11-20, 2005
Real time	81 h	96 h
Collimator	3 mm	3 mm
MAMI beam current	35 nA	12 nA
Tagger magnetic field	1.04943 T	1.04904 T
Enabled tagger channels	1-80	1-284
Tagged photon energies	680-820 MeV	207-820 MeV
MAMI beam energy	883.057 MeV	883.113 MeV

Table 3.2: Main conditions of the experiments dedicated to determination of the η meson mass.

through the programmable downscaler (D) and discriminator (A) to the L1 register. Only the CB energy sum is allowed as the trigger in L1 during the measurements. The recognition of the input sample in the register is initiated by the OR in the discriminator. By a valid L1 signal at the input, the register generates a signal at output 7 of the register, which locks the discriminator. Additionally the tagger TDC is stopped via output 4, and the time reference for the CB is generated via output 5. Output 6 releases recognition of the sample in the L2 register. The outputs of register L2 depend on the signals at inputs 1-3. The cluster multiplicity signals are checked at inputs 5 and 6 of the L2 register. Both signals pass via prescalers, which decrease the rate of $M \geq 2$ events by a factor of 3 (or 49 in the MDM experiment) allowing every 3rd (or 49th) event to be accepted. This decreases the number of π^0 production events read out but does not suppress detection of the $\eta \to 3\pi^0$ decay. The cross section for π^0 production is well known. Thus, this channel can be used for calibrations and to improve the understanding of the detector setup. Every recognition of a valid sample in the L2 register generates a signal, which passes to the trigger control system (TCS, see fig. 3.20). The TCS produces the trigger confirmation for the FIADC and starts the readout of the Crystal Ball and TAPS.

3.7 Conditions of the experiment

The data for the η mass experiment were taken during the 2004/2005 round of experiments with the Crystal Ball/TAPS setup at MAMI. Mainly the experiments were dedicated to determination of the $\Delta^+(1232)$ magnetic moment (MDM experiment) [Dow07, Kra07, Sch07, Zeh08, Boi08]. During November and December of 2004, η production data were taken (η experiment) in order to study the rare $\eta \to \pi^0\gamma\gamma$ decay [Bru07] and to determine the Dalitz plot parameter α of the $\eta \to 3\pi^0$ decay [Unv08]. In this experiment, the tagger microscope detector was enabled, the beam intensity was increased, and higher channels of the tagger (81-352) were disabled in order to improve the tagging rate. In December 2004 and additionally in January

	η experiment	MDM experiment
CB energy sum threshold	390 MeV	60 MeV
Cluster multiplicity $M \geq 2$	3	49
Cluster multiplicity $M \geq 3$	1	1
TAPS	No	Yes

Table 3.3: Trigger conditions of the experiments dedicated to determination of the η mass. The last row shows if TAPS contributed to the trigger.

2005, the data for determination of the η mass were taken. During this period the MAMI energy was measured periodically, the position of the MAMI beam at the tagger radiator was monitored, and the tagger magnetic field was kept constant (see appendix B). Any dramatic change of these parameters could influence the measured η mass. The main conditions of the experiments are summarized in table 3.2.

The trigger conditions for both experiments are given in table 3.3. The thresholds for the CB total energy sum were determined using the method described in Ph. D. Thesis by M. Unverzagt [Unv08] of Mainz. He also determined the discriminator thresholds for the cluster multiplicity trigger and developed software simulation of the trigger. The multiplicity trigger $M \geq 2$ in the MDM experiment was scaled by a factor of 49 in order to suppress detection of $\pi^0 \rightarrow 2\gamma$ decays. In the η mass experiment this factor was smaller to allow detection of the $\eta \rightarrow 2\gamma$ decays. TAPS was not included in the trigger for the η production runs because of the high beam intensity, which produced a large electromagnetic flux in the forward direction and created high cluster multiplicities in the forward detector.

Chapter 4

Calibration of the detectors

The experimental data were collected using the experimental setup described in the previous chapter. From these data, represented by the detector signals saved into the file system, the decay particles and physical reactions must be reconstructed. The analysis of these data was performed with the program AcquRoot version 3v17 [Ann05], a data acquisition and analysis suite based on ROOT [Web01], the CERN object-oriented data analysis framework. The program has been written mainly by J. R. M. Annand of Glasgow and is used at several European laboratories. Additional classes, describing different parts of the detector setup, were written for the present experiment. This work was distributed among the members of the collaboration.

The use of the object-oriented approach makes the description of the experimental apparatus and understanding of the code easier. The simplified hierarchy of the detector classes in AcquRoot 3v17 is presented in fig. 4.1. The low-level single detector elements (class *HitD2A_t*) convert the digitally stored data about the electronic pulse heights and times from ADCs and TDCs into energies in MeV and times in ns. The detector classes (*e. g.* *TA2CalArray*, *TA2TAPS_BaF2*), inherited from *TA2Detector*, use the data of their single elements and determine such values as total energy of the electromagnetic shower or the direction of a charged particle. From the data of single detectors, the 4-vectors of the physical particles are reconstructed by the apparatus classes (*e. g.* *TA2CrystalBall*, *TA2TAPS*), inherited from *TA2Apparatus*. Finally, the reconstructed 4-vectors are available to the element of a class, inherited from *TA2Physics*, which processes these 4-vectors and reconstructs the physical reactions and observables such as energies, invariant and missing masses. This class is foreseen to be fully written by the user, who adjusts the program to his needs.

In order to convert the raw numbers, collected during the experiment, into physical quantities, much work on calibration of the experimental setup has been done. This task was distributed among the members of the collaboration. The calibration information is stored in the setup files, which are loaded by AcquRoot on start-up. In this chapter, the calibrations of single elements of the detector setup are presented. It is sought to give the reader an impression of the method, used to calibrate different

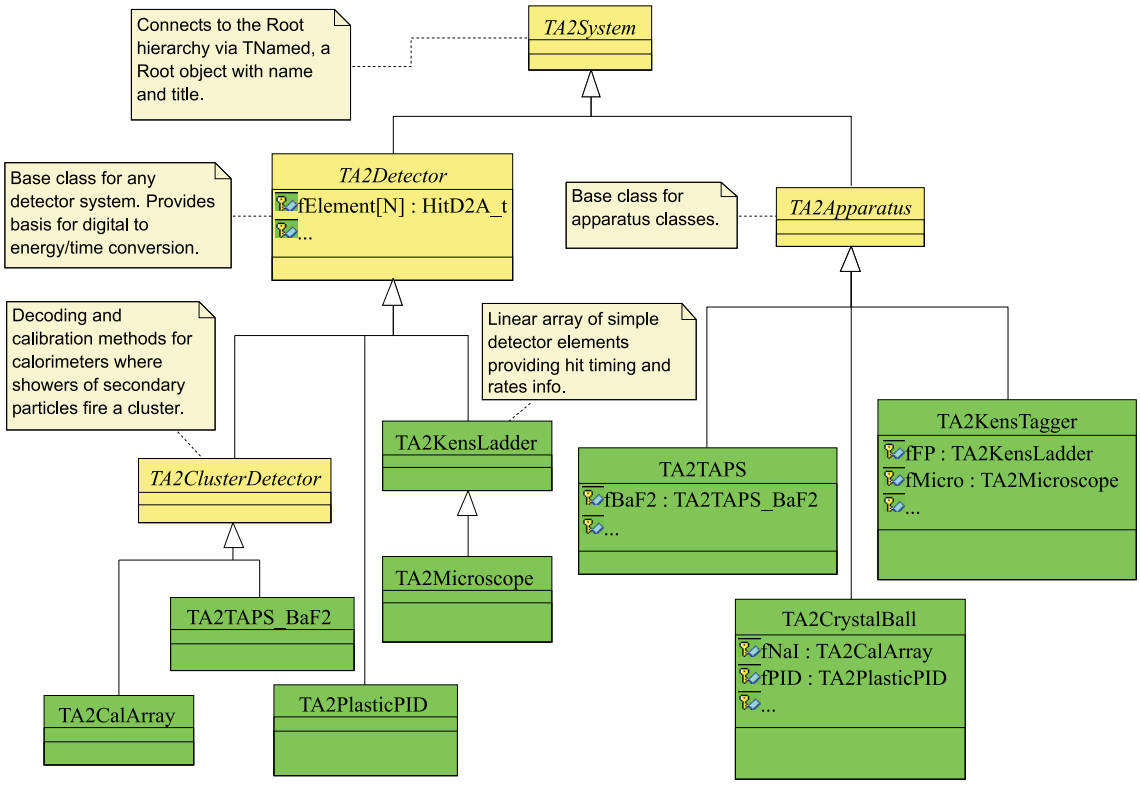

Figure 4.1: Very simplified hierarchy of the detector classes within AcquRoot 3v17. Each class handles the data of a certain element of the detector setup.

elements, rather than a full description of the process. The calibrations performed specifically by the author are given in more detail.

The next part of this chapter is dedicated to the photon energy determination and involves the MAMI energy determination and the energy calibration of the tagger microscope focal-plane detector. For determination of the η production threshold, the precise photon energy is important. Since the photon energy is determined as difference between the MAMI energy E_0 and the tagger electron energy E_{e^-},

$$E_\gamma = E_0 - E_{e^-}, \tag{4.1}$$

the determination of both energies is discussed. The absolute electron energy E_0 of the incident beam is determined in the 3rd race-track microtron (RTM3) of MAMI-B with the accuracy $\sigma_0 = 140\,\mathrm{keV}$. Special care was taken of the energy calibration of the tagger microscope which was used for the first time. It improves the tagged photon energy resolution.

The determination of such normalization values as the photon flux and the target density, which are important when determining the reaction cross sections, closes this chapter. The analysis of the photon flux measurements was performed by the author. This is the first study of the determination of the photon flux for an experiment using the microscope focal-plane detector.

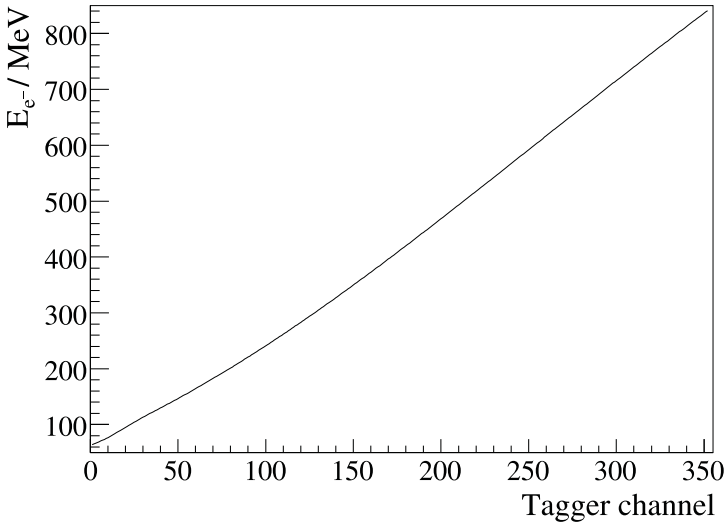

Figure 4.2: Energy calibration of the main focal-plane detector of the Glasgow-Mainz photon tagging spectrometer, obtained with the TAGCAL 6.0 calibration program, using the tagger magnetic field $B_{\text{exp}} = 1.049\,\text{T}$.

4.1 Calibration of the photon tagging facility

The photon tagging spectrometer (tagger) is used to determine the energy of the photon which has induced the reaction in the experimental target. The time and energy of the corresponding tagger electron must be found; therefore, the time information and the energies, corresponding to each tagger channel, are needed. The tagger energy and time calibrations for the main focal-plane detector array were performed by our colleagues from the University of Glasgow.

Tagger energy calibration

For determination of the photon energy from equation (4.1), the energy of the focal-plane electron must be determined from the place, where this electron hit the array of plastic scintillators. For the main focal-plane detector, a program, called TAGCAL 6.0, exists, which calculates the corresponding energies for each detector channel. This program assumes that the tagger magnetic field is uniform in a region whose effective edges are obtained from the measured field maps at magnetic field $B = 1.0\,\text{T}$ and $B = 1.4\,\text{T}$ and calculates the trajectories for different energies of the electron using the field value actually measured with an NMR probe located in the uniform field region. In the points where the trajectories cross the focal plane of the spectrometer, the average energy is assigned to each tagger channel. The output of TAGCAL 6.0 is plotted in fig. 4.2, using the tagger magnetic field set to the experimental value $B_{\text{exp}} = 1.049\,\text{T}$.

For a more accurate energy calibration of the main focal-plane detector in a specific region, it was scanned with the electron beam of three different energies

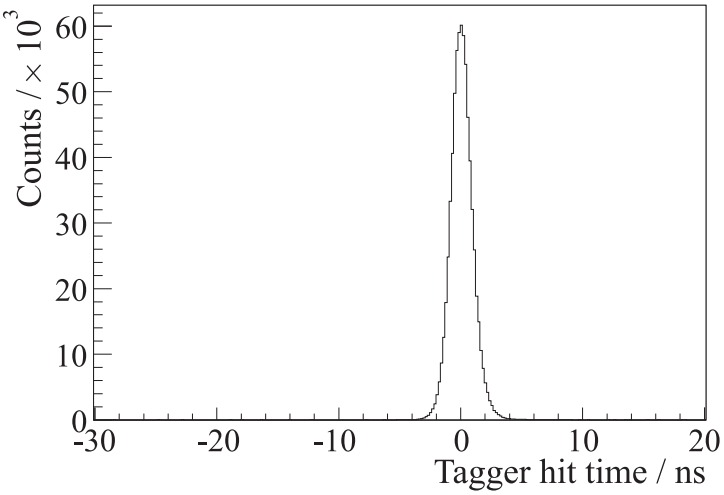

Figure 4.3: The timing distribution of the tagger hits taken during tagging efficiency measurement using the time of the Pb-glass detector as reference and after shifting the positions of the coincidence peaks of all tagger channels to the same position.

(180 MeV, 195 MeV, and 210 MeV). The beam was moved along the focal plane by gradually increasing the magnetic field, and the tagger hits distribution pattern was taken for each beam position. The scan covered tagger channels 69-85. The result of this calibration is summarized in appendix A. Energy calibration for the tagger microscope is discussed in section 4.5.

Tagger time alignment

Assignment of the tagging electron to the detected reaction is made through a coincidence between the tagging system and the detector setup. The tagger channels were aligned in time using measurements with the Pb-glass detector as the trigger, *i. e.* the measurements of the tagging efficiency, because the time behavior of the trigger signal in this case was much better than with the L1 energy sum trigger, during the normal production run. In the normal production runs the TDCs of the photon tagger were started by the electron detected in the focal plane and stopped by the L1 trigger signal. This means that the time information can be expressed through

$$t_{\text{tagger}} = t_{\text{L1}} - t_{e^-}. \tag{4.2}$$

Since the L1 trigger signal was built from many single contributions of the NaI detectors of the CB, and they had slightly different time responses (for example because of different cable lengths), the time behavior of the L1 trigger signal was not very precise. However, in the measurements of the tagging efficiency, the reference signal was generated by the Pb-glass detector driven into the beamline. This detector had very good time resolution (about 1.0 ns (FWHM)), and the achievable time resolution in t_{tagger} was better than the resolution obtained using the CB energy

sum trigger as the time reference. Because of low beam current the time spectrum was free of random coincidences (see fig. 4.3). The time alignment was performed by fitting a Gaussian function to the time spectrum of each tagger channel and shifting the coincidence peaks to the same position. After this procedure an overall tagger time resolution of about 2.0 ns (FWHM) was achieved.

4.2 Calibration of the Crystal Ball and PID

In the analysis of the data obtained from the 672 NaI crystals of the Crystal Ball (CB), the 4-vectors of the emitted particles have to be reconstructed. Therefore, calibrations which allow conversion of raw ADC and TDC data into physical quantities were necessary. Since the signals of the detectors, which originated from the same event, needed slightly different times to reach the TDCs, time alignment of the detectors was also necessary. Usually one particle induced the signals in a group (cluster) of detector elements, so that it was necessary to combine them in the software to obtain the signal for the particle.

Crystal Ball clustering algorithm

Due to a spread of an electromagnetic shower a single particle does not deposit energy just in one detector crystal, but the energy is distributed in a group of neighboring crystals. In order to reconstruct the energy and direction of the detected particle, the detector signals originating from the same shower has to be found and grouped into a so-called cluster. The information from the individual detectors in the cluster can be used to determine properties of the particle such as energy, direction and time.

The algorithm used for cluster determination is based on the fact that typically 98% of the shower energy is deposited in a group of 13 crystals. The energy deposits are stored in an array of detector elements which is processed by an AcquRoot detector class to find the crystal with the maximum energy deposit. This crystal is assumed to be the central crystal in a cluster. The detector setup file contains a list of the nearest neighboring crystals, and the array is scanned again to find the energy deposits which occurred in the neighboring crystals. The energy deposits of up to 12 neighboring crystals which exceeded a threshold of 2 MeV are added to the central crystal energy to form the total cluster energy. Assuming that the particle originated in the target center, the weighted mean of the vectors of the contributing crystals, using the square root of the energy in each crystal as the weight, is taken as the vector of the cluster. In the same way the cluster time is found as the energy weighted average. Once the cluster is found, the energy deposits are removed from the array, and the procedure continues until all elements in the array have been processed or the maximum permissible number of clusters is reached. Only clusters with energy larger than 20 MeV were accepted.

Sometimes the shower energy is distributed between more than 13 crystals. In this case the described algorithm can lead to loss of some energy in the cluster and identify the missed energy as another cluster. This problem is solved by extending the algorithm to scan through the neighboring crystals of neighboring crystals until the neighboring energy deposits are used up or a pre-determined (from the setup file) maximum distance to the central crystal is exceeded [Dow07].

Crystal Ball energy calibration

The energy calibration of the CB was based on measurements of the $\gamma p \to p\pi^0$ reaction, where the measured π^0 decay photon energies were compared to the energies expected from the kinematics of the reaction. The procedure and results of this calibration are described by J. Brudvik [Bru07]. Here a short summary of the calibration is presented.

In order to be able to observe the energies of the decay photons, one must know the full energy of the original π^0 meson. Due to two-body kinematics, the energy of the pion can be determined from the polar angle θ_{π^0} of the pion and the energy E_γ of the photon, incident on the target

$$2\,E_\gamma\,|\vec{q}_{\pi^0}|\cos\theta_{\pi^0} = 2\,E_{\pi^0}\,(E_\gamma + m_p) - 2\,E_\gamma\,m_p - m_{\pi^0}^2, \tag{4.3}$$

where $\vec{q}_{\pi^0} = \sqrt{E_{\pi^0}^2 - m_{\pi^0}^2}$ is the momentum of the π^0 and m_p, m_{π^0} are the proton and π^0 masses, respectively. This equation has two solutions for E_{π^0}, from which the solution closest to the measured value is taken. From this energy of the pion, the energies of the decay photons are determined by the Lorentz boost from the rest system of the pion, where each photon has the energy equal to half of the pion mass. The boost to the laboratory frame gives for the photon energy

$$E_\gamma = \frac{E_\gamma^{\mathrm{cm}}}{\gamma\,(1 - \beta\cos\theta_{\gamma\gamma})} \tag{4.4}$$

with opening angle $\theta_{\gamma\gamma}$ between the decay photons, and where β is the pion velocity in the laboratory frame in units of c, and $\gamma = 1/\sqrt{1-\beta^2}$. The energies, calculated in this way, serve for matching the measured photon energies. The reaction $\gamma p \to p\pi^0$ was selected by three conditions: 1) identification of the two photons in the CB 2) with the invariant mass $M_{\gamma\gamma} = (135 \pm 50)$ MeV and 3) missing proton mass $M_{\mathrm{miss}} = (938 \pm 100)$ MeV. For the crystal of the cluster which has collected more than 70% of the total cluster energy, a ratio between the expected and measured energies was taken. The distribution of the ratios for each single NaI crystal was fitted with a Gaussian, and the mean value μ at the peak was found. A new gain g_{new} (deposited energy in MeV per QDC channel) was calculated using

$$g_{\mathrm{new}} = g_{\mathrm{old}} \cdot \mu\,. \tag{4.5}$$

In the beginning of this procedure, all gains were set to a start value, and the process was repeated until the gain variations between iterations vanished. It was found that five iterations were enough.

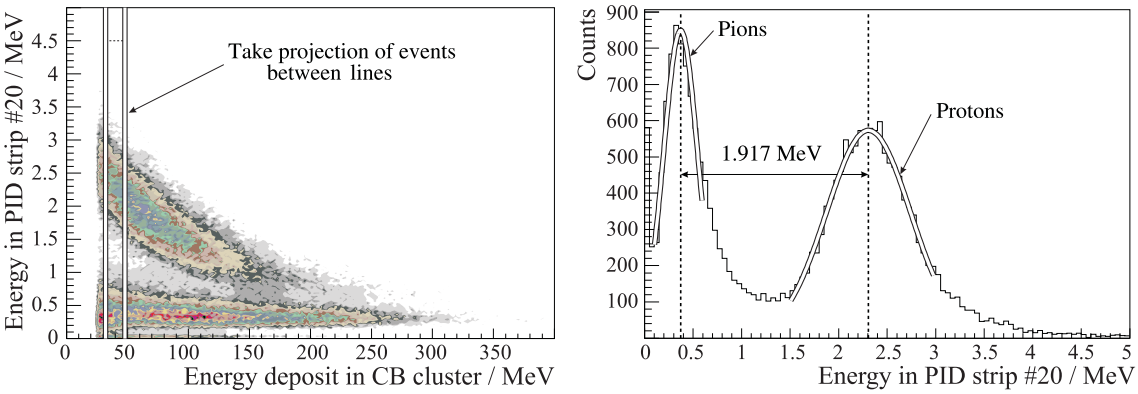

Figure 4.4: The energy calibration [Cod05], [Dow07] for one PID scintillator strip channel. Left: distribution of the energy deposited in one PID strip versus the total energy deposited in the CB cluster by the particle. Right: projection on to the PID axis with fit.

PID calibration

The particle identification detector (PID) provided the possibility to distinguish between the different particle species by comparison of the energy deposited in a CB cluster and the energy deposited in a plastic scintillator strip of the PID. The PID calibration procedures were designed and tested by E. Downie and performed by R. Codling of the University of Glasgow. These procedures are described in [Cod05] and [Dow07]. The energy calibration of the PID was based on fitting two Gaussian functions to the peaks on the exponential background in the distribution of the energy deposited in one PID strip (see fig. 4.4). The peak at higher energy results from protons and the lower energy peak from minimum ionizing particles such as $\pi^{\pm}$ mesons. Then the calibration factors of all plastic scintillator strips were aligned so that the positions and separations between the two peaks in all detector elements were identical.

The time alignment of the PID strip channels was performed by fitting a Gaussian to the time (with respect to the trigger) distribution obtained from the CATCH TDCs, and shifting the peaks for each strip channel to the same position. The intrinsic time resolution of a single strip was about $\approx 0.5\,\text{ns}$ (FWHM).

Crystal Ball time alignment

Although fast timing is provided by the low level PM02 discriminators in the CB electronics, the NaI hit time depends significantly on the pulse height, especially for small signals. This so-called *timewalk* behavior is shown in fig. 4.5. Therefore, for each of the 672 channels of the Crystal Ball, this energy dependence of the NaI hit time was determined and corrected. Due to the very good time response of the PID, it was selected as reference. The time was measured between the hit in the

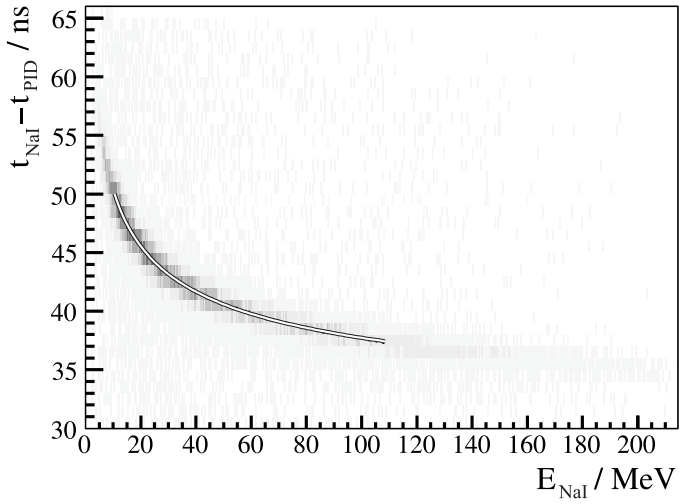

Figure 4.5: Dependence of the hit time in a NaI detector on the pulse height for one single channel of the Crystal Ball. The time difference between the NaI detector hit and the PID hit is shown versus the energy deposited in the NaI crystal. The correction function (4.6) was fitted to the data.

NaI crystal and the coincident hit in the PID. By building the difference between the two detector systems, the effect of the poorer trigger timing was eliminated.

The coincident hits in the CB and the PID were obtained by selection of the reaction $\gamma p \rightarrow p\pi^0$, using the following conditions: 1) two CB clusters detected as photons and one CB cluster detected as a proton; 2) the invariant mass of the photons $M_{\gamma\gamma} = (135 \pm 20)\,\mathrm{MeV}$. The measured difference between the average time t_{NaI} of the two photons in the CB and the time t_{PID} of the proton in the PID was plotted versus the energy E_{NaI} deposited in the NaI crystal for each of the 672 channels. The function

$$t(E) = a + \frac{b}{E^{0.33}}\,, \tag{4.6}$$

with parameters a and b, was fitted to the resulting plot, shown in fig. 4.5. The parameters were determined for each crystal. The correction was subtracted from the CB hit times in the analysis, so that the average time for all crystals after correction was around 0 ns. Thus, the dependence of the time on the pulse height was reduced, and no further calibration of the CB time was necessary.

4.3 Calibration of the TAPS detector

Since the TAPS forward detector was also built from scintillators, the basic data analysis was very similar to the Crystal Ball. In order to be able to reconstruct the energy, momentum, and time information for the detected particle, it was necessary to make energy and time calibrations for TAPS. The calibration procedures, described in [Boi08] and [Zeh08], are summarized in this section.

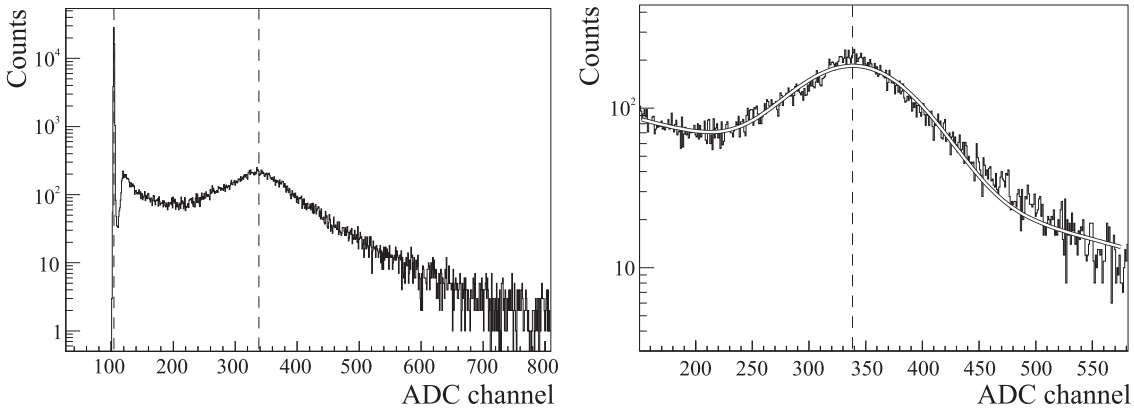

Figure 4.6: Energy calibration of the TAPS single detector with cosmic muons. Left: energy spectrum of cosmic muons measured with one BaF_2 detector. The dashed lines mark two calibration points at 0 MeV and 37.7 MeV which corresponds to the average energy deposited by the cosmic muons. Right: fitting Gaussian plus exponential distribution to the data to determine the precise position of the peak.

TAPS energy calibration

Since the BaF_2 crystals in connection with photomultipliers and readout electronics ensured a linear dependence between the measured pulse height and energy deposition, the knowledge of two calibration points (fig. 4.6 left) for each detector channel was enough to obtain the offset and gain. The first point was found from the pedestal peak channel (which corresponds to zero energy) in the ADC spectrum. Measurements of this zero were made regularly during the data taking using the pulse generator in the L1 trigger. The second calibration point was obtained from measurements of the cosmic radiation. Such calibration measurements were performed before and after each beamtime. Since all BaF_2 crystals have the same geometrical shape and are aligned horizontally, the energy deposition of the cosmic muons, which are minimum ionizing cosmic particles, in all crystals is identical. In BaF_2 these particles have a differential energy loss of $\mathrm{d}E/\mathrm{d}x = 6.39$ MeV/cm. From the thickness of the crystal of 5.9 cm, the average energy deposited is $E = 37.7$ MeV. The determination of this peak for the cosmic muons was done by fitting (fig. 4.6 right) a combination of Gaussian and exponential distributions to the ADC spectrum. The mean of the Gaussian gave the second calibration point. The two calibration points completely determined the MeV/channel conversion. This part of the calibration was performed by B. Boillat [Boi08] of the University of Basel. All TAPS detectors were calibrated in this way for both short and long gates.

Since the response of BaF_2 to photons differs from the response to cosmic muons, the calibration, described above, aligned the crystals, but did not give the correct MeV/channel conversion for photons. Moreover, the cluster energy had to be corrected for shower losses [Kot01]. For example signals below the CFD threshold were

filtered out and could not contribute to the cluster energy. After alignment of the crystals, the reaction $\gamma p \to p\pi^0$ was identified, and the two-photon invariant mass was derived for the case where one photon was detected in CB and the other in TAPS. Then all TAPS energies were multiplied by a factor that was adjusted until the measured peak moved to the correct π^0 mass value. This factor was found to be 1.14 and applied to all BaF_2 detectors.

TAPS time alignment

The BaF_2 crystals of TAPS have very good time resolution (about 0.5 ns (FWHM) [Nov91]). To benefit from this resolution it was necessary to align the TAPS detectors. The spectrum of time differences between hits in the BaF_2 crystals and in the photon tagger was generated to eliminate the relatively poor trigger timing resolution. The times of the tagger detector channels were already aligned (see section 4.1) with the aid of the tagging efficiency measurements. The time spectra of 510 TAPS channels were fitted with Gaussian, and the peak position was shifted for every channel to put the timing peaks at a common time. This alignment analysis only used TAPS hits identified as photons whose time of flight depends only on the almost constant distance to the target. This calibration was performed by F. Zehr [Zeh08] of the University of Basel.

4.4 Precise determination of the MAMI beam energy

The procedure for a precise MAMI-B beam energy measurement was implemented as a standard MAMI operator menu (MOPL routine), which allowed this measurement to be made in a computer supported and controlled manner [Jan06a]. The principle of the absolute energy measurement of the MAMI electron beam relied on accurate determination of the beam curvature in one of the two bending magnets of the RTM3 of MAMI. Since the magnetic field of the bending magnets is known, precise measurement of the bending radius of the electron determines the energy in the observed return track. The energy gain $\Delta E = 7.50\,\text{MeV}$ from turn to turn, known in the optimized microtron with an uncertainty of $\pm 20\,\text{keV}$ [Her92], gives the energy in the extraction path. The measurement of the absolute energy of the MAMI beam, summarized in this section, was established within the framework of two diploma thesis, by K. Herter [Her92] and Th. Dörk [Dör96]. The uncertainty of this measurement according to [Dör96] has been estimated to be $\sigma_0 = 140\,\text{keV}$.

The operating principle of a microtron has been presented in chapter 3. In the 3rd race-track microtron (RTM3) of MAMI, the beam makes 90 recirculations through the linac to reach the final extraction energy of 855 MeV (or 883 MeV). By precise measurement of the bending radius R_n of the electron beam in turn n, the beam energy E_n in return track n can be calculated. This procedure is performed [Dör96]

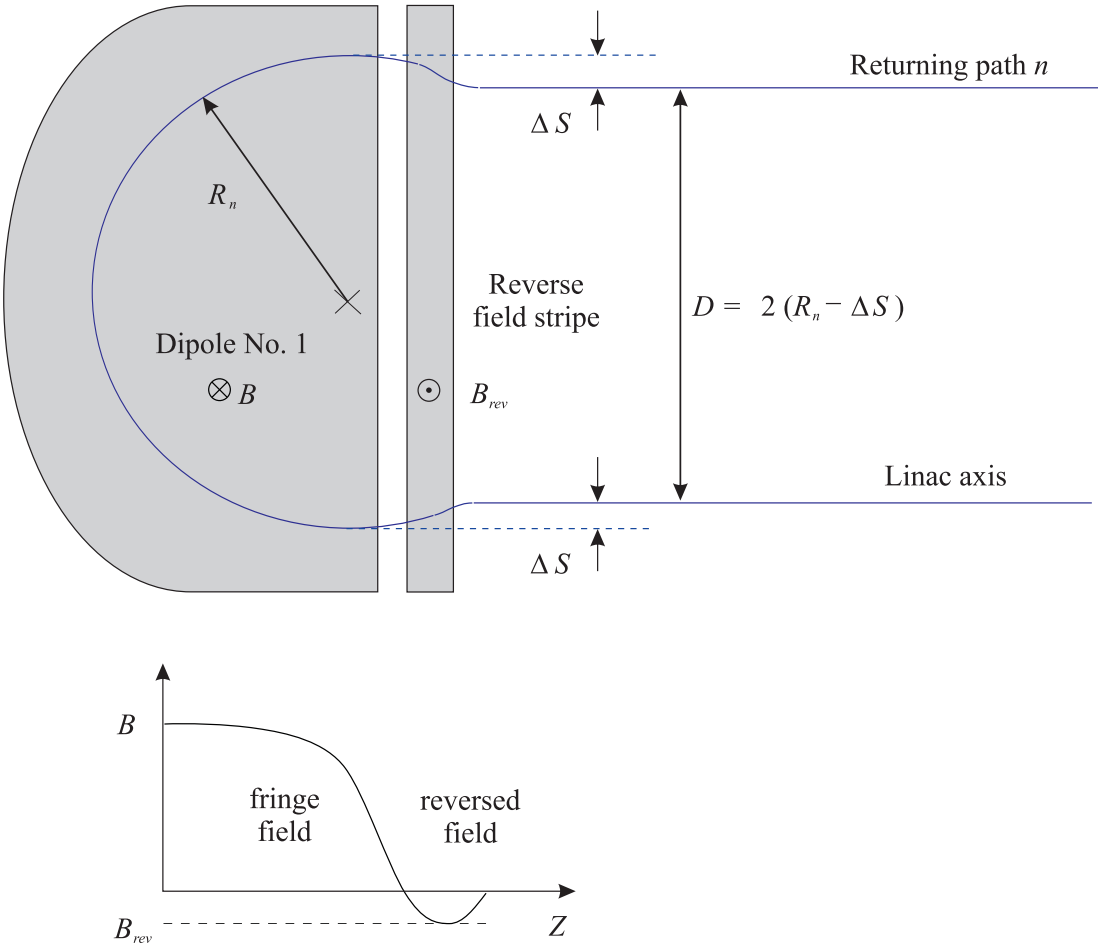

Figure 4.7: Schematic illustration of the path of the electron in the uniform field area of the bending magnet in RTM3. Additionally the magnetic field distribution B in the fringe field area as function of the beam path coordinate is shown. The reverse field stripe allows adjustment of the vertical focusing properties of the magnet.

in return track $n = 73$ of RTM3. The extraction energy E_0 after 90 recirculations through the linac can then be extrapolated using the data from PTRACE [Kai87], the proven and benchmarked particle tracking program used at MAMI.

The bending radius R_{73} in the uniform magnetic field B of the dipole can be expressed from the equality of the Lorentz force and the centrifugal force. For high energy relativistic electrons with $\beta \simeq 1$, one can write

$$E_{73} = e\,c\,B\,R_{73}\,, \tag{4.7}$$

where c is the speed of light in vacuum, e is the charge and E_{73} the energy of the electron. The beam path through the 180° bending magnet is schematically shown in fig. 4.7. The electron beam, leaving the linac axis, enters the reversed field stripe, which allows the vertical focusing properties of the magnet to be adjusted. In the horizontal direction the reversed field stripe causes a beam shift ΔS between the

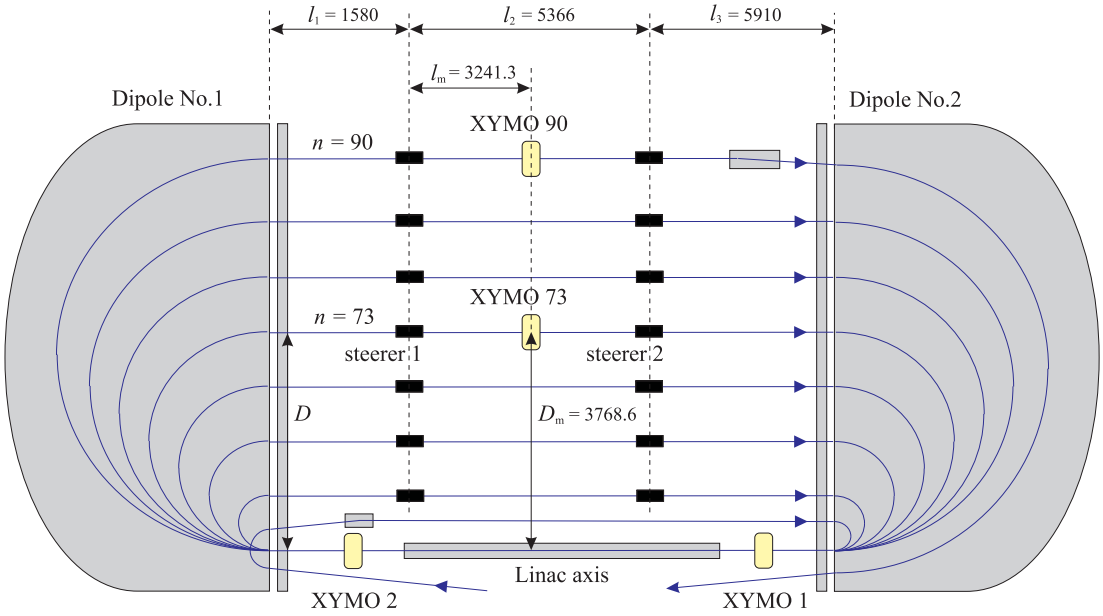

Figure 4.8: Determination of the distance D in the 3rd race-track microtron (RTM3) of MAMI-B. The X-Y position-sensitive HF monitors (XYMOs) were placed [Dör96] in return tracks 73 and 90. The steerers (dipole magnets) correct the beam, so that it is centered along the linac axis (monitored by XYMOs there).

linac axis and the tangent to the beam path in the uniform field area of the bending magnet. The same shift occurs as the beam leaves the uniform field area. The shift ΔS is determined with the PTRACE program via step by step integration and depends on the energy of the electron beam. In first order the ΔS in return track 73 can be approximated

$$\Delta S(E_{73}) = \Delta S_0 + g \cdot (E_{73} - E_{73\,\mathrm{PTRACE}})\,, \tag{4.8}$$

with $E_{73\,\mathrm{PTRACE}} = 727.658\,\mathrm{MeV}$, $\Delta S_0 = 6.03\,\mathrm{mm}$, and $g = -8.297 \cdot 10^{-3}\,\mathrm{mm/MeV}$. The second term is very small and in principle can be neglected (100 keV energy deviation results in 0.8 μm shift). Thus, the bending radius R_{73} can be determined by measuring the distance D between the beam position in the linac axis and the beam position in return track 73, in case of ideal 180° bending, and using the value of ΔS from equation (4.8),

$$R_{73} = D/2 + \Delta S = D/2 + \Delta S_0 + g \cdot (E_{73} - E_{73\,\mathrm{PTRACE}}). \tag{4.9}$$

From equations (4.7) and (4.9) follows

$$E_{73} = e \cdot c \cdot B \cdot \frac{D/2 + \Delta S_0 - g \cdot E_{73\,\mathrm{PTRACE}}}{1 - e\,c\,B\,g} \tag{4.10}$$

as the formula for determination of the beam energy in return track 73.

Figure 4.8 schematically illustrates the determination of D in RTM3 of MAMI. The measurement is performed in diagnostic mode [Jan06a], so that the position and phase of the beam can be observed. During the optimization procedure, the electron beam is steered through the microtron, so that it is centered along the linac axis, which is monitored by XYMO[1] 1 and XYMO 2. When the optimization has been completed, the angles θ_1 and θ_2 of the horizontal steerers 1 and 2 of the 73rd return track can be read out at the control panel. In the next step the beam is centered in XYMO 73 with the aid of steerer 1. The angle θ_m of the steerer is also stored. The value of D is determined from the distance D_m between the center of XYMO 73 and the linac axis. From simple geometry, described in detail in [Her92], D can be found as

$$D = D_\mathrm{m} + (l_1 + l_\mathrm{m})\,\alpha - l_\mathrm{m}\,\theta_\mathrm{m}\,, \tag{4.11}$$

with $\alpha = c_1\,\theta_1 + c_2\,\theta_2$, where l_1 is the distance between center of steerer 1 and the dipole edge, l_m is the distance between the center of steerer 1 and the center of XYMO 73, and c_1 and c_2 are geometric factors,

$$c_1 = \frac{l_2 + l_3}{l_1 + l_2 + l_3} = 0.877 \quad \text{and} \quad c_2 = \frac{l_3}{l_1 + l_2 + l_3} = 0.460. \tag{4.12}$$

Since the angles θ_1 and θ_2 can be determined only if the beam returns to the linac and passes through the XYMOs again, the procedure, described above, can not be performed for return track $n = 90$ which is used to extract the beam. Therefore, the energy is determined in return track $n = 73$ and the final energy E_0 after 90 recirculations can be extrapolated using

$$E_0 = E_{73} + \Delta E_{90}\,, \tag{4.13}$$

where the difference ΔE_{90} is calculated by PTRACE. This tracking calculation is based on the standard magnetic field profiles measured at $B_0 = 1.2842\,\mathrm{T}$. Finally, the PTRACE data for E_n versus n are fitted with a 3rd order polynomial and slightly scaled using the magnetic field values measured in the dipoles during the experiments.

The use of four 9.8 MHz high-frequency TM_{110} resonators [Dör96] as XYMOs, which were located in the linac axis and in return tracks 73 and 90 (see fig. 4.8), avoids degradation of the beam quality. The monitors were mounted on stable calibration tables, which were fixed in the middle vacuum chamber of the RTM3. The total uncertainty of the XYMO position was estimated to $\pm 0.2\,\mathrm{mm}$, and the electron beam position in it was determined with $\pm 10\,\mu\mathrm{m}$ precision.

Equations (4.10), (4.11), and (4.13) can be written as

$$E_0 = e\,c\,B\,\frac{(D_\mathrm{m} + \delta D)/2 + \Delta S_0 - g\,E_{73\,\mathrm{PTRACE}}}{1 - e\,c\,B\,g} + \Delta E_{90}\,, \tag{4.14}$$

[1] XYMO – X-Y position-sensitive high-frequency MOnitor.

Parameter	Typical value	Error	σ, keV	Procedure
B	1.2842 T	0.00013 T	$86_{\text{[part. syst.]}}$	Measured field uniformity
ΔS	6.03 mm	0.1 mm	$45_{\text{[syst.]}}$	PTRACE calculation
D_{m}	3768.6 mm	0.4 mm	$90_{\text{[syst.]}}$	Geodetic measurement
δD	< 0.2 mm	0.17 mm	$38_{\text{[non}-\text{syst.]}}$	Error propagation
ΔE_{90}	127.5 MeV	13$\oplus$10 keV	$17_{\text{[syst.]}}$	PTRACE calculation
		Total σ_0	140 keV	

Table 4.1: Contributions to the total uncertainty of the MAMI electron beam energy [Dör96, Jan06a]. In estimation of the uncertainty of $\delta D = (l_1 + l_{\text{m}})\,\alpha - l_{\text{m}}\,\theta_{\text{m}}$, the uncertainties of l_1, l_2, l_3, l_{m} of about 5 mm and uncertainties of θ_1, θ_2, θ_{m} of about 0.03 mrad (typical steerer angles during the measurement ~ 0.3 mrad) were adopted. The second uncertainty in ΔE_{90} of 10 keV is the systematic fit error. The typical values of the parameters are valid for the output MAMI energy $E_0 = 855$ MeV. The symbol $\oplus$ indicates summation in quadrature.

where $\delta D = (l_1 + l_{\text{m}})\,\alpha - l_{\text{m}}\,\theta_{\text{m}}$. The five parameters, contributing to E_0, are summarized in table 4.1. Using the law of error propagation one can show that the total uncertainty $\sigma_0 = 140$ keV is dominated by the measured field uniformity of the RTM3 magnet and by the uncertainty of the geodetic measurement of D_{m}. Therefore, the distance D_{m} was measured [Jan08] again in 2008 on two different days, and the result, reported in [Her92], was reproduced to a precision of ± 0.1 mm.

Since the majority of the parameters in table 4.1 do not change from one measurement to another, they make a systematic contribution to the total uncertainty. The distance D_{m} did not change significantly since 1996. The calculations based on PTRACE are constant for all measurements. The PTRACE simulation already includes the measured profile of the magnetic field, and this profile changes just slightly depending on the actually measured magnetic field B. The uncertainty of the absolute value of B measured with an NMR system is negligible. The only non-systematic contribution is the uncertainty of δD, estimated to be about 38 keV, caused by the determination of the beam position in the XYMOs and by the measurement of the angular deviations, produced by the steerer magnets. In order to obtain an objective estimate of the non-systematic contribution, the RMS deviation from the average of the 106 values of the MAMI energy, E_{73}, measured in the period 04/2004 - 07/2009 (see fig. 4.9) was calculated, which resulted in

$$\sigma_{\text{MAMI}} = 40\,\text{keV}. \tag{4.15}$$

This is probably an overestimate because slight differences in the MAMI tuning could have made the energies slightly different. The systematic uncertainty of the MAMI energy is then 134 keV.

For the operation of MAMI-B at the maximum output energy $E_0 = 883$ MeV, the slightly increased magnetic field $B = 1.3260$ T is used. This change slightly

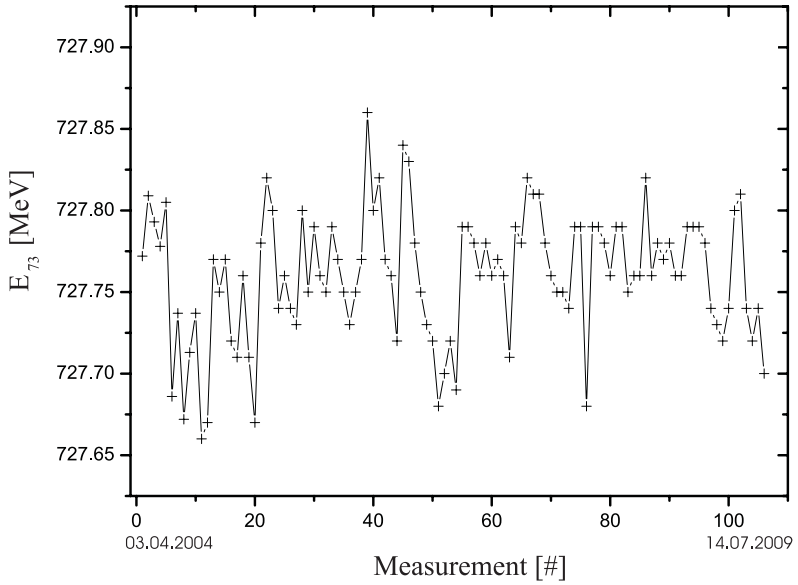

Figure 4.9: Measured energy E_{73} in the period 04/2004 - 07/2009. The RMS deviation of the 106 points from the average is $\sigma(E_{73}) = 40\,\text{keV}$.

affects the shape of the magnetic field and, thus, the calculation of ΔS and ΔE_{90} by PTRACE, but has no influence [Jan06a] on the estimation of the uncertainty. For the η mass experiment in 12/2004, the MAMI beam energy was measured four times with the average value

$$E_0 = (883.057 \pm 0.024_{\,\text{RMS}} \pm 0.134_{\,\text{syst.}} \pm 0.040_{\,\text{non-syst.}})\,\text{MeV}. \tag{4.16}$$

4.5 Energy calibration of the tagger microscope

Special care was taken of the energy calibration of the tagger microscope with electrons of different known energies from MAMI. The MAMI accelerator crew can produce beam energies from 180 MeV upwards in steps of 15 MeV and make accurate measurements of the beam energy. Originally designed to produce electrons of maximum energy 855 MeV, MAMI can also produce a beam of energy 883 MeV by slightly increasing the magnetic field of the bending magnets and slightly raising the energy gain per circulation. The η mesons in the experiment are produced above the production threshold energy of about $E_\gamma = 707\,\text{MeV}$ in photon energy. At the beam energy $E_0 = 883\,\text{MeV}$, this corresponds to the region below 176 MeV in terms of tagging electron energies, and all energies that MAMI can produce are above this region. Thus, in order to get calibration points above the η threshold, it is necessary to vary the magnetic field of the tagger and correct for the effects of the field shape change in the fringe field region of the magnet.

The energy calibration of the tagger microscope was originally studied and performed by A. Reiter [Rei04, Rei06] and our colleagues from the University of Glas-

gow. For the η mass experiment, the analysis of the calibration data has been carefully performed by the author. The main differences of the analysis, presented in this section, in comparison to the previous analysis are listed below.

- The determined microscope hit positions were systematically larger in comparison to the old analysis by about 0.1-0.2 channels or 30-60 keV. A small error in the old code was found to be the reason for this difference.
- In 05/2004 the MAMI operator menu was slightly changed, and a new fit for determination of the value of ΔE_n [Jan06a] was implemented. Unfortunately, this fit was based on slightly different PTRACE data that led to an incorrect determination of the MAMI energy for the scans made in 05/2004. Later they reported a more accurate value of 195.13 MeV instead of 195.24 MeV for these scans.
- The corrected analysis, performed with PTRACE, reduced the measured MAMI energies for the setup with $B = 1.3260$ T by about 130 keV [Jan06a]. For the energy measured in 12/2004 this analysis gave the more accurate value of 186.06 MeV instead of 185.9 MeV, which was obtained by simple interpolation using a calculator.

4.5.1 Calibration procedure

Before the calibration procedure (scan), it was necessary to take data with the Pb-glass detector providing the trigger in order to adjust the high voltage of the multianode photomultipliers in the microscope and set the discriminator thresholds for the scintillator strips appropriately. The calibration procedure was performed at low beam current and without radiator. However, the scattering in the diamond radiator used in the experiment (see section 3.2) could change the distribution of the electrons at the tagger focal plane and influence the energy calibration. Tests with a 20 μm thick Ni radiator foil showed that the effect of scattering in the radiator was negligible (see fig. 4.10). The tagger magnetic field was gradually increased until the beam reached the position of the tagger microscope. At low beam current the typical event rate in the tagger microscope was 3-5 kHz. The cycle for each step of the scan consisted of an increase of the tagger magnetic field B_{cal} in small steps. This simulated equivalent electron energies E_{equiv} for the magnetic field B_{exp} of the experiment:

$$E_{\mathrm{equiv}}(i) = E_{1,2,3} \times \frac{B_{\mathrm{exp}}}{B_{\mathrm{cal}}(i)}\,, \tag{4.17}$$

where i denotes the i-th measurement in a scan, and $E_{1,2,3}$ is the energy of the calibration beam. A period of 5-10 minutes was required, during which the magnetic field stabilized, then a short run (about one minute) was enough to obtain data on the channel hits distribution. The field was changed in finer steps around $B_{\mathrm{cal}} \approx B_{\mathrm{exp}}$ for the accurate absolute calibration of the main tagger focal-plane detector,

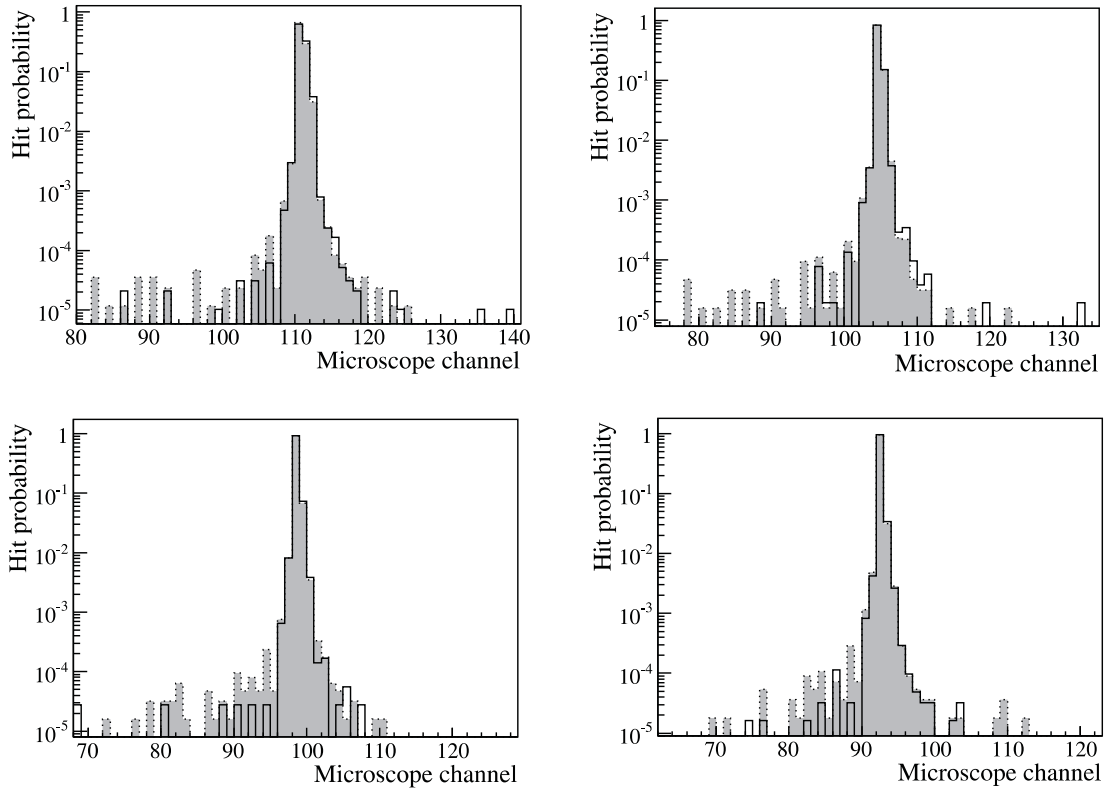

Figure 4.10: Microscope channel hits distributions with (dotted) and without (solid) the 20 μm thick Ni radiator for four different field settings during the scan with the 180.12 MeV MAMI beam.

presented in appendix A, where the beam was gradually moved through the overlap between two adjacent tagger channels. The tagger magnetic field was measured by the NMR probe and displayed on the NMR monitor. For a complete scan of about 30 calibration points, a beamtime of about 8 hours was required. The MAMI energy was measured before or after the scan. Online monitoring of the electron/photon beam position during the scans was impossible due to the very low beam current.

In the period 2003/2004, seven calibration scans were performed, which are summarized in table 4.2. Three scans were done with the beam energy 180 MeV to check the reproducibility of the calibration, two scans with 195 MeV, one with 210 MeV, and one with 186 MeV beam. During scan 5 (see table 4.2) a jump of the beam was observed. First few points of the scan agreed with the previous scans and at some point the position of the beam in the focal plane jumped by about 3 microscope channels (about 1 MeV). The reason for this jump has not been found, and the scan was not used in the analysis. Measurement 6 with the same energy performed two days later seemed to be more successful at first glance. But later it was found that the beam energy was measured two times with the value 195.13 MeV instead of 195.24 MeV, used earlier in [Rei04] and [Rei06], which was the average value of the same two measurements, earlier reported to be 195.10 MeV and 195.38 MeV, one

#	Date	$E_{1,2,3}$, MeV	B_{cal}, T	Comments
1.	12.12.2003	180.12	$1.01 - 1.07$	Good
2.	20.01.2004	180.13	$0.89 - 1.08$	Good
3.	21.01.2004	210.21	$1.05 - 1.21$	Good
4.	23.01.2004	180.15	$0.90 - 1.21$	Good
5.	*25.05.2004*	*195.25*	$0.98 - 1.24$	*Shift by about 1 MeV* ($\approx 17\sigma$)
6.	*27.05.2004*	*195.13*	$0.98 - 1.21$	*Shift by about 200 keV* ($\approx 3.5\sigma$)
7.	07.12.2004	186.06	$0.92 - 1.23$	Good

Table 4.2: The list of scans for the tagger microscope calibration. The shifts in scans 5 and 6 were not explained, and these scans were not used for the calibration.

of which was just linearly interpolated and, therefore, was much too high [Jan06a]. Analysis using the new energy for these data has shown that the scan deviated by about 200 keV from the others. The question of excluding this scan from the calibration is discussed later in section 4.5.5.

4.5.2 Determination of the hit position

The information collected by any tagging device such as the tagger microscope is a hits distribution pattern which stores the number of counts for each element, given by the content in the respective TDC spectrum. From the microscope strip hit information (96 scintillator strips) a channel hit pattern (191 channels) was constructed, taking into account the 1/3 overlap between adjacent strips. A typical strip-hits distribution in the tagger microscope is shown in fig. 4.11. The solid histogram in the left panel shows the full spectrum. The tails caused by the scattering in the 1 mm aluminum window (see fig. 3.6) can be suppressed if only the events with a single hit (multiplicity 1) or with two hits in adjacent strips (multiplicity 2) are accepted (left dotted histogram) and all other events are rejected. Multiple scattering in the aluminum window and backscattering off the main focal-plane detector array caused an asymmetric distribution of the hits. The tail towards higher strip numbers is characterized by a higher multiplicity due to reduced incident angles at the microscope plane that causes an electron to hit more than one strip, and, therefore, a cut on multiplicities of 1 and 2 eliminates these events from the spectrum. The right histogram in fig. 4.11 represents the corresponding pattern in microscope channels. From this pattern, the hit position P_i was determined as the sample mean over the full spectrum,

$$P_i = \sum_{j=1}^{j=N} \left\{ (j-1)\,\frac{H[j]}{A[j]} \right\} \Big/ \sum_{j=1}^{j=N} \frac{H[j]}{A[j]}\,, \tag{4.18}$$

where $N = 191$ is the number of tagger microscope channels, and $H[j]$ is the TDC hits distribution pattern (fig. 4.11 right). Since the single- and double-hit channels are of unequal width (see section 3.3), the number of hits is divided by the relative

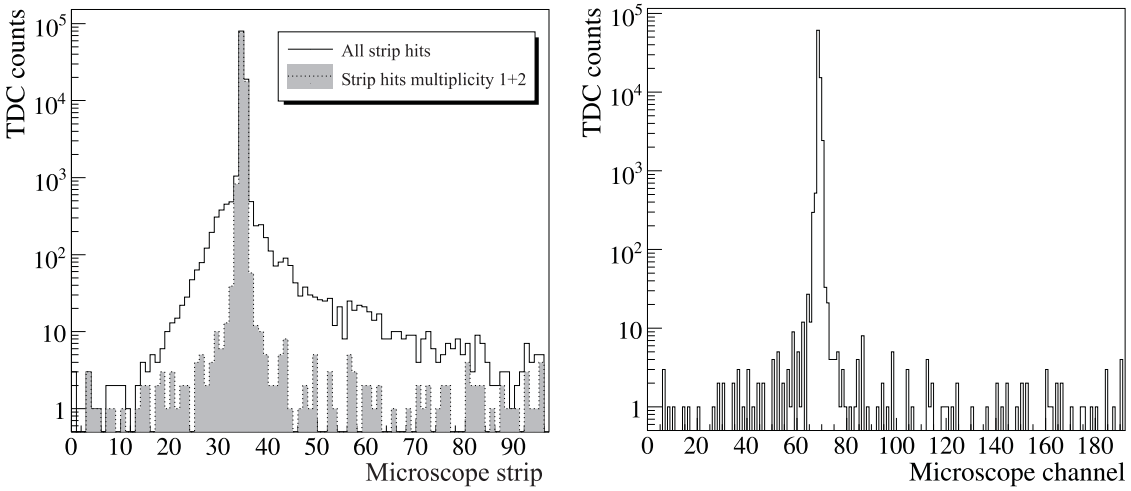

Figure 4.11: Left: microscope strip-hits distribution (solid) and the same distribution for multiplicities 1 and 2 (dotted) in logarithmic scale. Right: corresponding channel-hits distribution.

channel acceptance, $A[j]$. This acceptance was measured in the experiment as the number of hits in the corresponding TDC (see fig. 4.24 right) in the random window of the tagger time spectrum. In equation (4.18), $(j-1)$ is used because the channels numbering ranges from 0 to 190, and the hits in the pattern $H[j]$ are stored in bins 1-191. The equivalent energies $E_{\mathrm{equiv}}(i)$, calculated with equation (4.17), were then plotted versus the measured hit positions P_i.

4.5.3 Estimate of the uncertainty of the hit position

For each beam position in a scan the microscope hits distribution spectrum and the tagger magnetic field were measured. The beam position was determined for each measurement as the mean value over the full spectrum using equation (4.18). The uncertainty of the hit position was estimated from the standard deviation of the calibration data points from the fit function. The linear fit function

$$E_{e^-}(x) = a + b\,x \tag{4.19}$$

was used, where x is the microscope channel, and $E_{e^-}(x)$ is the corresponding energy of the electron. The values of the fit parameters a and b were obtained from the fit to the data. In order to simplify the error propagation and reduce covariance between the fit parameters, the fit was performed at the center of microscope hit positions, *i. e.* the mean value of all measured microscope hit positions, $\overline{P_i}$, was subtracted from the microscope channel x,

$$E_{e^-}(x) = a + b\,(x - \overline{P_i})\,. \tag{4.20}$$

This made the covariance between the two fit parameters vanish. The straight line (4.20) was fitted to each of the seven calibration scans, and the uncertainty was

#	Date	N	σ, keV
1.	12.12.2003	18	63.9
2.	20.01.2004	26	32.5
3.	21.01.2004	33	35.3
4.	23.01.2004	11	67.1
5.	25.05.2004	32	89.8
6.	27.05.2004	33	57.8
7.	07.12.2004	19	61.9
		Average σ_P	58.3 keV

Table 4.3: Standard deviations of the data points from the fits for each scan. N is the number of points. The average value of $\sigma_P = 58.3\,\text{keV}$ was used as the uncertainty of all data points in the analysis.

estimated as the standard deviation of the data points from the fit function,

$$\sigma = \sqrt{\frac{1}{N-2}\sum_{i=1}^{N}\left\{E_{\text{equiv}}(i) - E_{e^-}(P_i)\right\}^2}\,. \tag{4.21}$$

The seven uncertainties, calculated individually for each of the seven scans, are summarized in table 4.3. The uncertainty σ_P of the microscope hit position has been found as the average of the seven values, which resulted in $\sigma_P = 58.3\,\text{keV}$. This value includes all relevant effects apart from the uncertainty of the MAMI energy.

4.5.4 Reproducibility of the calibration scans

Since the MAMI accelerator and beamlines to the A2 hall must be set up and optimized for each scan, the results of repeated scans need not necessarily be consistent. It is important that the MAMI beam optimization procedure results in a reproducible, stable beam trajectory. This was tested by doing the beam optimization and scan three times at virtually the same MAMI energy (180 MeV) in 01/2004 (the scans listed in table 4.2).

When the data points of different scans are compared, besides the hit position uncertainty, σ_P, an additional uncertainty should be taken into account. This uncertainty is composed of the uncertainty in determination of the MAMI energy and initial misalignment of the beam at the radiator at the beginning of a scan. The two mentioned factors can slightly differ from one scan to the next, and a small change of one of them causes all data points of the scan to move by the same amount. Here only the non-systematic uncertainty of the MAMI energy, $\sigma_{\text{MAMI}} = 40\,\text{keV}$ (see section 4.4), contributes. The uncertainty of the initial beam misalignment was estimated to be about $\sigma_B = 40$ keV (see appendix B.4). The total uncertainty is

$$\sigma_C = \sqrt{\sigma_{\text{MAMI}}^2 + \sigma_B^2} = 56.6\,\text{keV}. \tag{4.22}$$

This uncertainty is correlated for all points in the same scan.

The fit function defined by equation (4.20) was fitted to each scan individually and to the combined data of the three scans. The parameters of the fit are summarized in table 4.4, and the resulting fits are shown in fig. 4.12. In the case when data of different scans are fitted together, the correlation between the data points in the same scan leads to a block-diagonal form of the covariance matrix [Bar89] used in the fit procedure. Therefore, the fit was performed by a least squares minimization with the aid of the MINUIT package using function (4.23) for minimization,

$$\chi^2 = \sum_{i=1}^{N}\sum_{j=1}^{N}\left\{\mathcal{M}^{-1}(i,j)\left(E_{\text{equiv}}(i) - E_{e^-}(P_i)\right)\left(E_{\text{equiv}}(j) - E_{e^-}(P_j)\right)\right\}, \qquad (4.23)$$

where N is the total number of the data points, $E_{e^-}(x)$ is the fit function defined in (4.20), and $\mathcal{M}$ is the covariance matrix,

$$\mathcal{M} = \begin{pmatrix} \mathcal{D}_1 & 0 & 0 \\ 0 & \mathcal{D}_2 & 0 \\ 0 & 0 & \mathcal{D}_3 \end{pmatrix}, \qquad (4.24)$$

with blocks $\mathcal{D}_{1,2,3}$ representing the covariance matrices of the scans. The squared uncertainty, σ_C^2, was assigned to the off-diagonal elements of the $\mathcal{D}_{1,2,3}$ matrices, and the squared total uncertainty, $\sigma_C^2 + \sigma_P^2$, was assigned to the diagonal elements, so that the blocks $\mathcal{D}_{1,2,3}$ had the following structure:

$$\mathcal{D}_{1,2,3} = \begin{pmatrix} \sigma_C^2+\sigma_P^2 & \sigma_C^2 & \sigma_C^2 & \cdots & \sigma_C^2 \\ \sigma_C^2 & \sigma_C^2+\sigma_P^2 & \sigma_C^2 & \cdots & \sigma_C^2 \\ \sigma_C^2 & \sigma_C^2 & \sigma_C^2+\sigma_P^2 & \cdots & \sigma_C^2 \\ \vdots & \vdots & \vdots & \ddots & \\ \sigma_C^2 & \sigma_C^2 & \sigma_C^2 & & \sigma_C^2+\sigma_P^2 \end{pmatrix}. \qquad (4.25)$$

Such a fit procedure delivered the best result and realistic estimation of the uncertainties of the fit parameters.

For all measurements, shown in fig. 4.12, the tagger magnetic field had to be varied in range 0.9-1.2 T. Figure 4.12 shows good agreement between the three data sets obtained with 180 MeV beam. In two regions, around 180 MeV and 210 MeV, the step size was reduced to scan the beam through the overlap between two adjacent tagger channels for accurate calibration of the main detector array.

4.5.5 "Direct" calibration

In a so-called "direct" calibration, the points are all measured at the same tagger field. Data from five scans were used to obtain five "direct" calibration points. For each beam energy, one point corresponding to the tagger magnetic field $B_{\text{cal}} = B_{\text{exp}}$ was determined using a linear fit to all points in the scan.

Date	a, MeV	b, keV/ch	$\overline{P_i}$, ch	$E_{e^-}(75)$, MeV
12.12.2003	178.815 ± 0.014	290.21 ± 0.42	85.724	175.702 ± 0.014
20.01.2004	193.487 ± 0.011	291.24 ± 0.27	135.921	175.744 ± 0.020
23.01.2004	178.234 ± 0.018	290.92 ± 0.29	83.720	175.697 ± 0.018
Combined	185.626 ± 0.034	290.95 ± 0.18	109.052	175.718 ± 0.034

Table 4.4: The fit results for the scans with 180 MeV beam. The last column is the energy corresponding to microscope channel 75 (near η threshold).

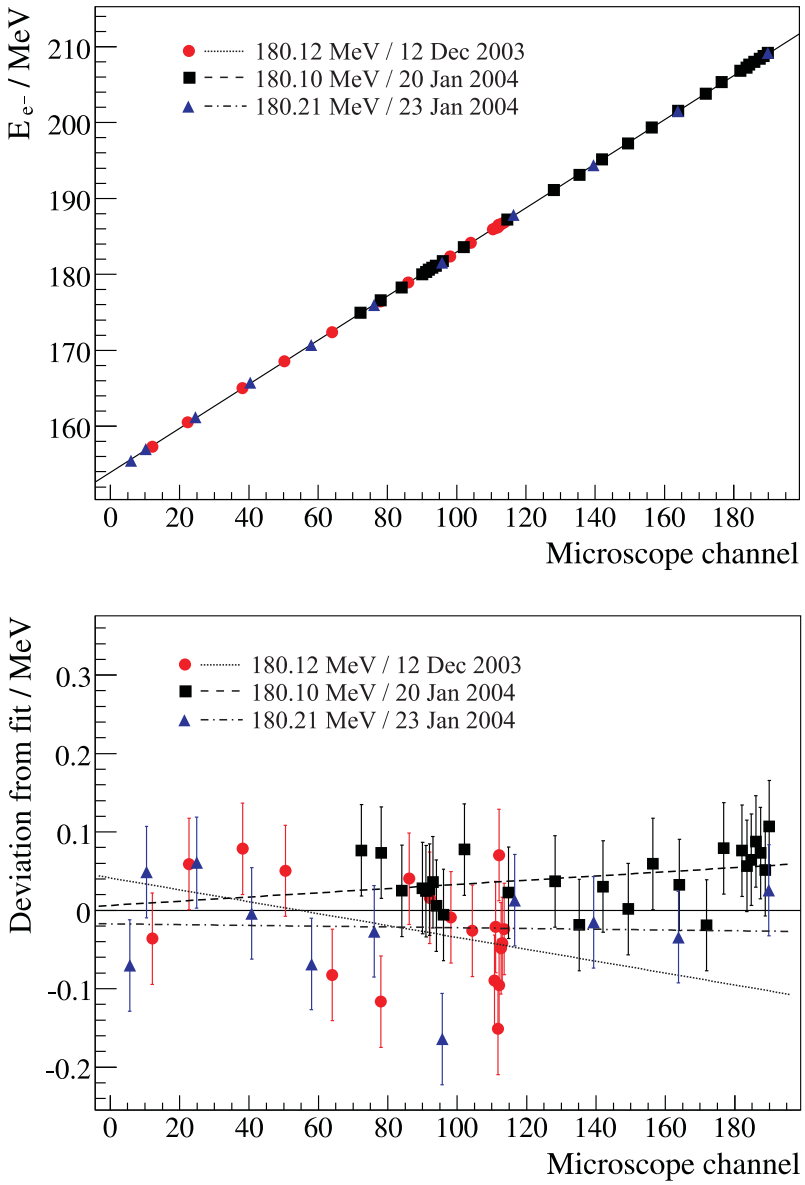

Figure 4.12: Tagger microscope energy calibration with 180 MeV beam including 3 scans (top), and deviations of the data points from the linear fit to the combined data set (bottom). The lines represent individual fits to the data of each scan.

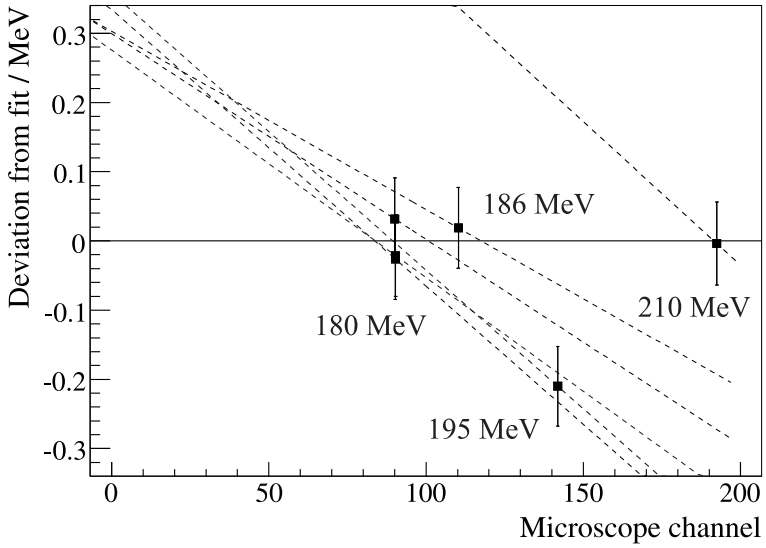

Figure 4.13: Deviation of the data points from the linear fit in the "direct" calibration. Straight lines represent individual fits to each scan. The "direct" point from the scan with 195 MeV beam differed by about 3.5 standard deviations from the others and therefore was not used in the "direct" fit.

The relevant uncertainty of each single point in the "direct" calibration consists of two parts, the uncertainty of the hit position and the uncertainty σ_C from eq. (4.22). The first uncertainty was estimated from the fit parameters of each single scan to be about ±10-20 keV. Thus, the total uncertainty of each single point in fig. 4.13 does not exceed ±60 keV. This means that the 195 MeV point differs from the others by about 3.5 standard deviations (see fig. 4.13), strongly suggesting that something was wrong with this scan as well as with the other 195 MeV scan made two days earlier, which deviated by about 1 MeV from the others. A possible explanation of such a deviation is a shift of the MAMI beam position, which could not be monitored during the scans due to the very small beam current. Unfortunately, no beam position check was made after the scans. Therefore, the inconsistency of both 195 MeV scans remained unexplained. Neither was used in the energy calibration of the tagger microscope.

4.5.6 Correction for the effect of the field shape change

Equation (4.17) (repeated here for convenience as equation (4.26)) is based on the assumption that the shape of the field profile along the electron trajectory does not change if the field strength is varied.

$$E_{\mathrm{equiv}}(i) = E_{1,2,3} \times \frac{B_{\mathrm{exp}}}{B_{\mathrm{cal}}(i)} \tag{4.26}$$

This is not strictly correct, especially in the fringe field region of the tagger, where the field profile can change significantly if the magnetic field B_{cal} is varied. For

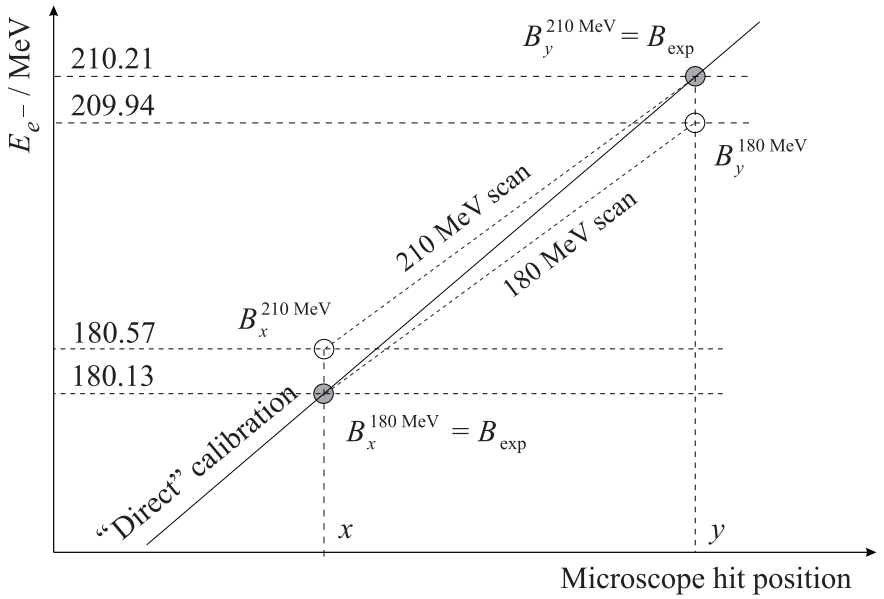

Figure 4.14: Schematic of the beam swap test. Due to the change of the effective field integral, the slope from the beam scans is slightly smaller than that given by the two points for which the tagger field is B_{exp} used in the η production experiment ("direct" calibration).

example, if the magnetic field as measured by the NMR, which is located in the uniform field region of the tagger, is increased by a factor 1.4, the field in the fringe region of the magnet increases by a factor of up to 2.5 [Rei04]. This leads to a larger effective field (integral along the electron trajectory), hence the bending power increases with the magnetic field by slightly more than expected on the basis of eq. (4.26). Therefore, the measured hit position is shifted slightly along the focal plane toward lower microscope channels. This effect was observed in the "direct" calibration – see section 4.5.5, fig. 4.13 – and is schematically illustrated in fig. 4.14.

In order to estimate a correction term for this effect, a test of the variation of the field integral has been made. First, the hit position x (fractional channel number) was found, where the 180 MeV beam hits the focal-plane detector for the field $B_x^{180\,\mathrm{MeV}} = B_{\mathrm{exp}}$, at which the η production data were taken (see fig. 4.15 left), and the field $B_x^{210\,\mathrm{MeV}}$ that makes the 210 MeV beam hit this position (see fig. 4.15

Beam energy	B_x, T	B_y, T
180.13 MeV	B_{exp}	0.900412
186.06 MeV	1.083743	0.929702
210.21 MeV	1.222032	B_{exp}

Table 4.5: Measured magnetic fields required to move the beam of different energies to the same position in the focal-plane detector. $B_{\mathrm{exp}} = 1.04943\,\mathrm{T}$.

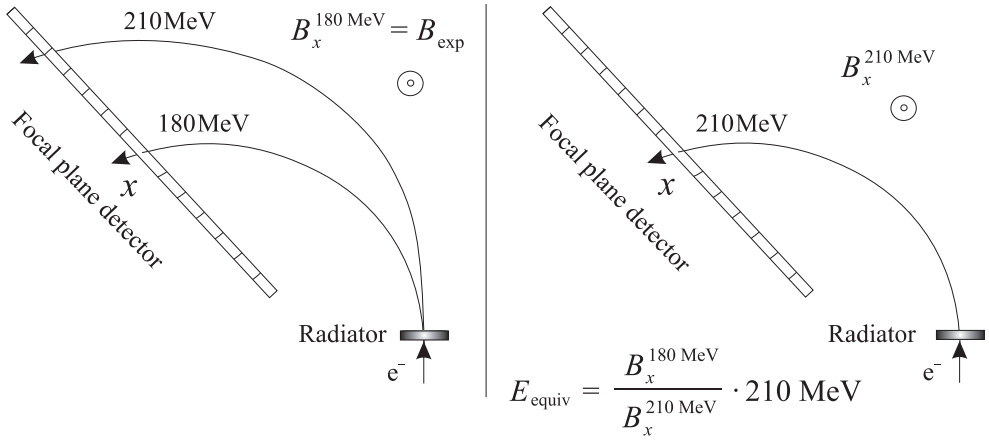

Figure 4.15: The 180 and 210 MeV beam trajectories for the tagger field B_{exp} used in the η production experiment (left) and at the field, $B_x^{210\,\mathrm{MeV}}$, at which the 210 MeV beam hits the same point along the focal plane simulating equivalent energy $E_{\mathrm{equiv}} \approx 180\,\mathrm{MeV}$ (right).

right). Then the hit position y was found, where the 210 MeV beam hits the focal-plane detector for the field $B_y^{210\,\mathrm{MeV}} = B_{\mathrm{exp}}$, and the field $B_y^{180\,\mathrm{MeV}}$ that makes the 180 MeV beam hit this position. In ideal circumstances (no fringe field effect), the electron trajectories are identical, and the ratios of the beam energies and NMR values should be equal. Since the NMR value can be determined quite precisely, and many systematic effects are eliminated in the ratio, any deviation is thought to be due to a change of the field distribution along the particle trajectory. The field values $B_x^{210\,\mathrm{MeV}}$ and $B_y^{180\,\mathrm{MeV}}$ were obtained from linear fits to the scans and are summarized in table 4.5.

Using the data in table 4.5, the equivalent electron energy of the 180 MeV beam at the 210 MeV position can be calculated:

$$E_{\mathrm{equiv}} = 180.13\,\mathrm{MeV} \cdot \frac{B_y^{210\,\mathrm{MeV}}}{B_y^{180\,\mathrm{MeV}}} = 209.938\,\mathrm{MeV}. \tag{4.27}$$

The same calculation for the 210 MeV beam at the 180 MeV position leads to

$$E_{\mathrm{equiv}} = 210.21\,\mathrm{MeV} \cdot \frac{B_x^{180\,\mathrm{MeV}}}{B_x^{210\,\mathrm{MeV}}} = 180.566\,\mathrm{MeV}. \tag{4.28}$$

This procedure is illustrated in fig. 4.14. Above the magnetic field B_{exp}, the 210 MeV scan (dashed line) is systematically higher than the solid line drawn through the points at the magnetic field B_{exp}. Qualitatively this is explained by the increased effect of the fringe field in the region, where the electrons enter and exit the tagger magnet, so that the 210 MeV beam impinges the position x at slightly lower magnetic field than expected, and the beam simulates a higher electron energy. Similarly, the 180 MeV scan is shifted because of a reduced fringe field integral.

$E_{1,2,3}$	a, MeV	b, keV/ch	$\overline{P_i}$, ch	$E_{e^-}(75)$, MeV
180.12 MeV	178.795 ± 0.014	293.50 ± 0.42	85.724	175.647 ± 0.014
180.13 MeV	193.610 ± 0.011	293.91 ± 0.27	135.920	175.705 ± 0.020
210.21 MeV	190.902 ± 0.010	293.96 ± 0.26	126.702	175.704 ± 0.016
180.15 MeV	178.195 ± 0.018	294.00 ± 0.29	83.720	175.632 ± 0.018
186.06 MeV	183.089 ± 0.013	294.30 ± 0.22	100.215	175.668 ± 0.014
Combined	186.821 ± 0.026	294.04 ± 0.12	112.927	175.670 ± 0.027

Table 4.6: Calibration results for the corrected data. The last column is the photon energy corresponding to microscope channel 75 (near η threshold).

The effect mentioned above can be reduced if a correction term is applied, assuming that the offset depends linearly on the difference between the scanning magnetic field B_{cal} and the value of the magnetic field B_{exp}. The correction for the 180 MeV scan can be written as

$$\Delta E_{180\,\text{MeV}} = \left(210.21 - 180.13 \cdot \frac{B_y^{210\,\text{MeV}}}{B_y^{180\,\text{MeV}}}\right) \cdot \frac{B_{\text{cal}} - B_{\text{exp}}}{B_y^{180\,\text{MeV}} - B_{\text{exp}}}\ \text{MeV}. \tag{4.29}$$

Thus, at the field $B_{\text{cal}} = B_{\text{exp}}$ the correction is zero and increases to the maximum of 272 keV at the field $B_{\text{cal}} = B_y^{180\,\text{MeV}}$. The correcting term for the 210 MeV data is given by

$$\Delta E_{210\,\text{MeV}} = \left(180.13 - 210.21 \cdot \frac{B_x^{180\,\text{MeV}}}{B_x^{210\,\text{MeV}}}\right) \cdot \frac{B_{\text{cal}} - B_{\text{exp}}}{B_x^{210\,\text{MeV}} - B_{\text{exp}}}\ \text{MeV}. \tag{4.30}$$

This term is zero at the field $B_{\text{cal}} = B_{\text{exp}}$ and decreases to the minimum of -436 keV at the field $B_{\text{cal}} = B_x^{210\,\text{MeV}}$.

The simulated electron energies for the 186 MeV data at the positions x and y gave 180.216 MeV and 210.049 MeV, respectively. Since this energy is quite close to the 180 MeV, the scan was corrected using the position of the 210 MeV beam at magnetic field B_{exp}. This correcting term is given by

$$\Delta E_{186\,\text{MeV}} = \left(210.21 - 186.06 \cdot \frac{B_y^{210\,\text{MeV}}}{B_y^{186\,\text{MeV}}}\right) \cdot \frac{B_{\text{cal}} - B_{\text{exp}}}{B_y^{186\,\text{MeV}} - B_{\text{exp}}}\ \text{MeV}, \tag{4.31}$$

where $B_y^{186\,\text{MeV}}$ is the field at which the 186 MeV beam hits position y. The correcting terms (4.29) - (4.31) were applied to correct the measured data.

4.5.7 Results of the calibration

The five calibration scans gave the 107 data points shown in fig. 4.16. The correlation between the data points in the same scan, originating from the uncertainty of the MAMI energy, lead again to a block-diagonal form of the error matrix used in the fit procedure. Therefore, the fit was performed by a least squares minimization with the

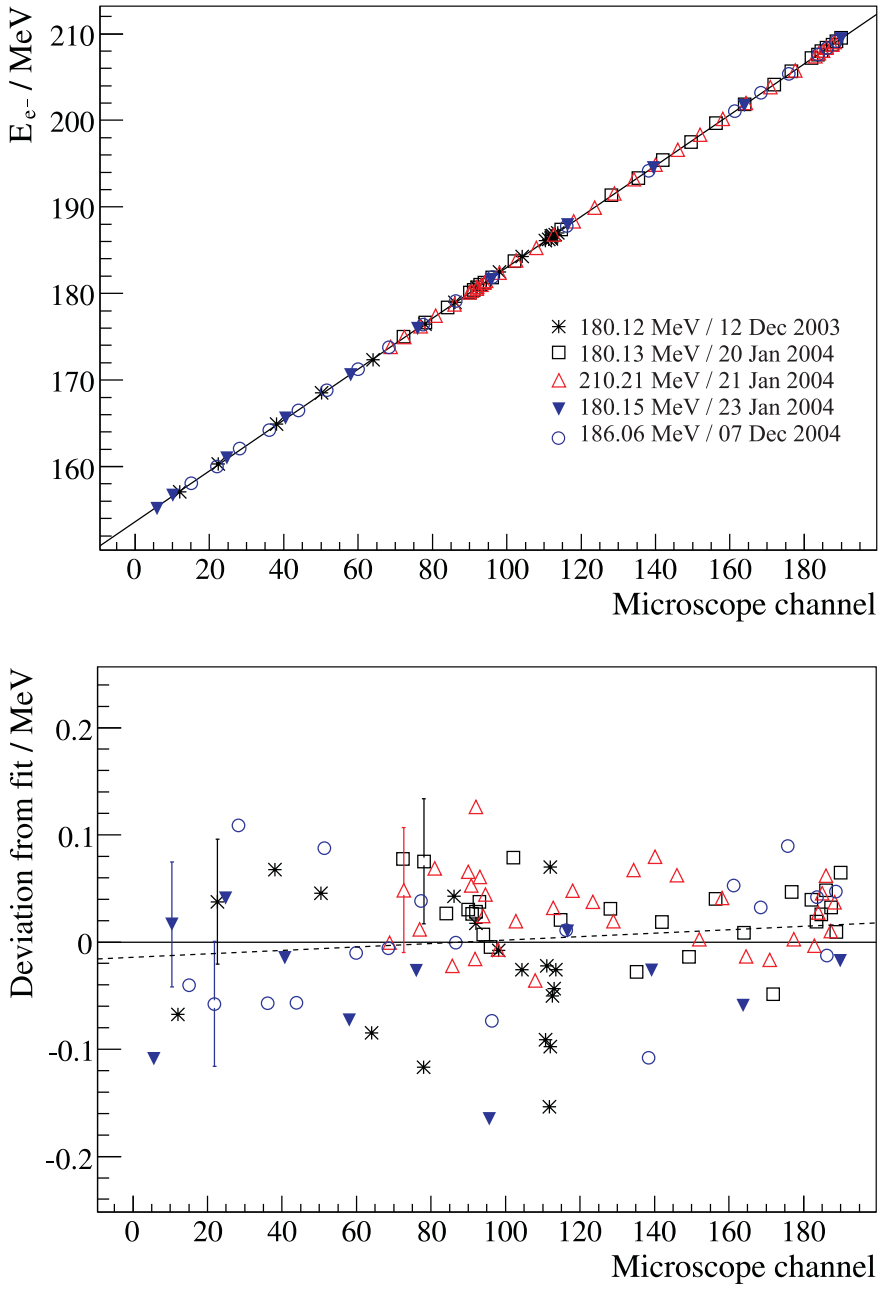

Figure 4.16: Energy calibration of the tagger microscope with the five scans. Corrections for changes in the shape of the tagger magnetic field were applied. The solid line represents a linear fit to all the data points, and the dashed line shows the difference from the "direct" fit.

aid of the MINUIT package, using for minimization the χ^2 function defined earlier in equation (4.23) but with the covariance matrix, $\mathcal{M}$, consisting of five blocks. The minimum value $\chi^2 = 70.2$ was obtained, so that $\chi^2/(N-2)$ was less than 1. This is probably because some of the uncertainties were overestimated (see section 4.4). The fit parameters for each single scan and for all data are summarized in table 4.6.

4.5.8 Systematic uncertainty of the calibration

With the known energy E_0 of the MAMI electron beam (see equation (4.16)) and the energy E_{e^-} of the tagging electron, the energy E_γ of the Bremsstrahlung photon is determined using

$$E_\gamma = E_0 - E_{e^-}. \tag{4.32}$$

For tagging electron energies E_1, E_2, or E_3, the photon energy E_γ is given by

$$E_\gamma = E_0 - E_{1,2,3}\,. \tag{4.33}$$

Taking into account equation (4.13) one can write

$$E_\gamma = E_{73}(\text{exp.}) + \Delta E_0 - E_{73}(\text{cal.}) - \Delta E_{1,2,3}\,, \tag{4.34}$$

where $E_{73}\,(\text{exp.})$ is the E_{73} value measured during the η production experiment, $E_{73}\,(\text{cal.})$ is the value measured for each of the calibration scans, and ΔE_0 and $\Delta E_{1,2,3}$ are the differences (calculated by PTRACE) between the measured energy E_{73} and the output MAMI energies E_0 and $E_{1,2,3}$, respectively. As the calibrations for E_0 and E_{e^-} are both based on measurement of E_{73}, the systematic uncertainty in determination of E_{73} cancels, and only the non-systematic uncertainty of E_{73} is necessary, and it contributes twice.

The main contributions to the total uncertainty of the MAMI energy are the uncertainty of the distance D_m (see fig. 4.8), measured by the geodetic method, which is a systematic contribution, and the measured magnetic field uniformity of the MAMI magnets – see section 4.4. Since the PTRACE simulation already includes the measured profile of the magnetic field, this contribution is also systematic. The non-systematic contribution, due to the uncertainty in the beam position and in the measurement of the angular deviations produced by the steerer magnets, was estimated to be about 38 keV, and the uncertainty due to the measurement of the absolute magnetic field B_0, made with the NMR system, was negligible. In order to obtain an independent and less subjective estimate of the non-systematic contribution, the RMS deviation from the average of the 106 values of the MAMI energy E_{73} measured in the period 04/2004 - 07/2009 was calculated (see fig. 4.9), which resulted in $\sigma_\text{MAMI} = 40\,\text{keV}$.

All contributions to the uncertainty of the photon beam energy are summarized in table 4.7. The values of ΔE_0 and $\Delta E_{1,2,3}$ were calculated by PTRACE with uncertainties 13 keV and 55 keV [Jan06a], respectively. The second uncertainty, added in quadrature, is the uncertainty of the 3rd order polynomial fit to the PTRACE

Parameter	Procedure	Contribution
E_{73}(exp.)	Non-systematic MAMI uncertainty	40 keV
E_{73}(cal.)	Non-systematic MAMI uncertainty	40 keV
ΔE_0	PTRACE calculation	$13 \oplus 10$ keV
$\Delta E_{1,2,3}$	PTRACE calculation	$55 \oplus 20$ keV
Systematic uncertainty of the calibration fit	Fit parameters	27 keV
Initial beam misalignment	MAMI optimization	40 keV
Beam position drift in the experiment	RF cavities	20 keV
Total $\sigma(E_\gamma)$		98 keV

Table 4.7: List of contributions to the total uncertainty $\sigma(E_\gamma)$ of the photon beam energy calibration. The symbol $\oplus$ indicates summation in quadrature.

data, mentioned in section 4.4. The systematic uncertainty of the calibration fit was estimated from the fit parameters from table 4.6 by applying the law of error propagation to the linear fit function (4.19). Possible slight misalignment of the beam at the beginning of the scans introduced the uncertainty $\sigma_B = 40\,\text{keV}$ (see section 4.5.4). The contribution caused by the drift of the beam position at radiator during the experiment (see appendix B.2) was estimated to be $\pm 20\,\text{keV}$. Added in quadrature, all contributions resulted in a total uncertainty of

$$\sigma(E_\gamma) = 98\,\text{keV} \tag{4.35}$$

in the determination of the photon energy E_γ. The value (4.35) can be converted to the systematic uncertainty of the η mass by applying the law of error propagation to equation (1.1) that gives

$$\sigma(m_\eta) = 62\,\text{keV}. \tag{4.36}$$

4.6 Determination of the target density

In order to determine reaction cross sections, such normalization factors as the density of the liquid hydrogen (ℓH_2) target are necessary. This value is given as the number of protons N_p per cm^2 which is seen by the incident photon beam and can be calculated from the properties of the ℓH_2 target,

$$N_p = \frac{N_\text{A}}{M_\text{mol}} \cdot \rho_{\ell\text{H}_2} \cdot L_\text{cell}. \tag{4.37}$$

Beside such constants as the molar mass $M_\text{mol} = 1.00794$ g/mol of the liquid hydrogen and Avogadro's number $N_\text{A} = 6.0221415 \cdot 10^{23}$ mol^{-1}, knowledge of the length L_cell of the target cell and the density $\rho_{\ell\text{H}_2}$ of the liquid hydrogen is also necessary.

Under normal working conditions the target was at temperature $T = (20.5 \pm 0.5)\,\mathrm{K}$ and pressure $p = (1080 \pm 0.5)\,\mathrm{mbar}$, for which the density of the liquid hydrogen is $\rho_{\ell\mathrm{H}_2} = (0.0706 \pm 0.0007)\,\mathrm{g/cm^3}$ [Web04]. The geometric length of the target cell was measured to be $L_{\mathrm{cell}} = (4.76 \pm 0.03)\,\mathrm{cm}$ [Tho07]. Putting these values in (4.37) gives

$$N_p = (2.008 \pm 0.024) \cdot 10^{23}\ \mathrm{cm}^{-2}. \tag{4.38}$$

The uncertainty of N_p contributes 1.2% (σ) to the systematic uncertainty of the cross sections.

4.7 Determination of the photon flux

Another normalization factor, which is necessary for determination of reaction cross sections, is the number of photons hitting the target. The number of photons produced by the Bremsstrahlung process in the radiator is proportional to the total number of counts $N_{e^-}(i)$ in the tagger scalers for each tagger channel i. But some photons are lost due to collimation at the tagger exit and do not reach the target. The ratio between the number of tagged photons passing through the collimator, N_γ, and the number of tagger electrons, N_{e^-}, is known as tagging efficiency, $\varepsilon_{\mathrm{tagg}}$. Each tagger channel had a scaler which counted the total number of tagger electrons, N_{e^-}. Thus, the photon flux, N_γ, can be determined from

$$N_\gamma(i) = N_{e^-}(i) \cdot \varepsilon_{\mathrm{tagg}}(i). \tag{4.39}$$

The value of $\varepsilon_{\mathrm{tagg}}(i)$ depends on the photon energy and, therefore, should be determined for each tagger channel i. The tagging efficiency is influenced by such factors as the diameter of the collimator, alignment of the electron beam compared to the collimator axis and the beam energy. Since the tagging efficiency could slightly change during the experiment, it must be periodically measured. The fluctuations were monitored during production runs using the ratio between the counting rate in a P2 ionization chamber, placed behind the target to measure the photon beam intensity, and the counting rate in the tagger electron scalers.

4.7.1 Determination of the tagging efficiency

Since $\varepsilon_{\mathrm{tagg}}$ depends on how well the beam is aligned, the tagging efficiency was taken during the experiment at least once between the optimizations of the MAMI beam. For these measurements a Pb-glass detector, an almost 100% efficient detector of photons, driven into the photon beam (see fig. 4.17) generated the trigger signal. The use of small MAMI beam current avoided detector damage and excessive loss of events while the hardware was busy with reading out and storing the data. As one can see in fig. 4.17, not all Bremsstrahlung photons reach the Pb-glass, as some photons are removed by the collimator at the tagger exit. Therefore, the number of photons N_γ detected in the Pb-glass is less than the number of electrons N_{e^-},

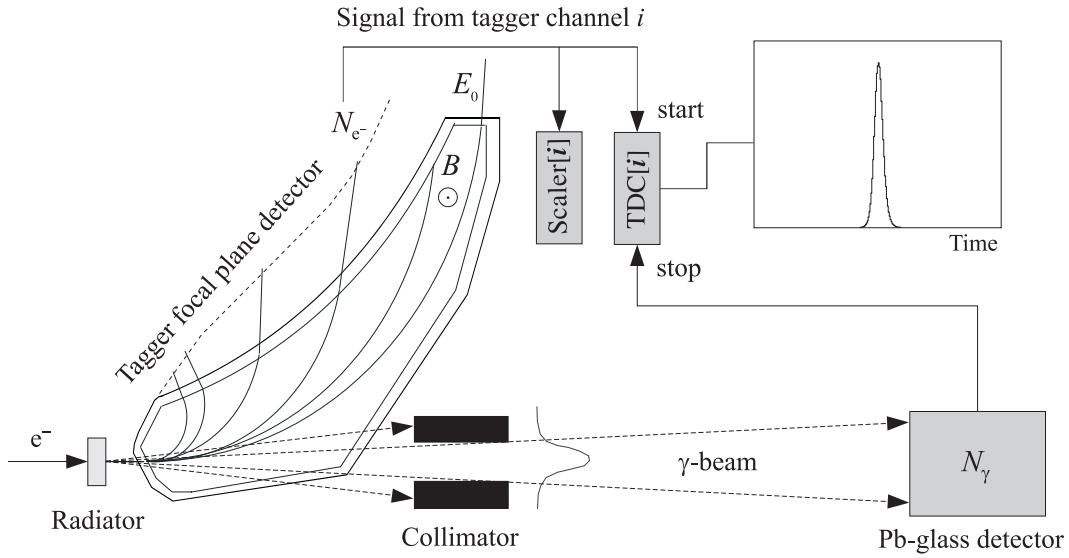

Figure 4.17: Schematic illustration of the experimental setup for measuring the tagging efficiency using the Pb-glass detector driven into the photon beam.

detected in the tagger focal-plane spectrometer, and the tagging efficiency is always less than 100%.

The tagger focal-plane detector receives the tagging electron earlier than the photon generates a reaction in the target. The electron, which hits channel i of the focal-plane detector, starts the clock TDC(i). The common stop signal for all TDC clocks comes from the experiment trigger which is initiated by the Pb-glass detector. At low beam current the random coincidence background in the tagger time spectrum was negligible (see fig. 4.3). Therefore, it was always possible to determine the electron hit for each photon detected in the Pb-glass. The number of TDC hits in tagger channel i, which had a coincident photon, gave the number of tagged photons, $N_\gamma(i)$ (see fig. 4.18 top), and the scaler for channel i gave $N_{e^-}(i)$ (see fig. 4.18 bottom). The tagging efficiency was calculated using

$$\varepsilon_{\text{tagg}}(i) = \frac{\text{TDC}(i)}{\text{Scaler}(i)} = \frac{N_\gamma(i)}{N_{e^-}(i)} = \frac{N_\gamma(i)}{(N_{e^-}(i) - N_\gamma(i)) + N_\gamma(i)} \,. \tag{4.40}$$

Applying the law of error propagation to equation (4.40) one obtains

$$\sigma(\varepsilon_{\text{tagg}}(i)) = \frac{1}{N_{e^-}^2(i)} \cdot \sqrt{N_{e^-}(i) \cdot N_\gamma(i) \cdot (N_{e^-}(i) - N_\gamma(i))} \tag{4.41}$$

for the statistical uncertainty of $\varepsilon_{\text{tagg}}$. In order to take the correlation between N_γ and N_{e^-} into account and apply the law of error propagation, the denominator in equation (4.40) was decomposed into two independent parts.

The tagging efficiency was measured six times during the first beamtime and five times during the second beamtime of the η mass experiment. Usually the measurements were made with the radiator used in the experiment for about 30

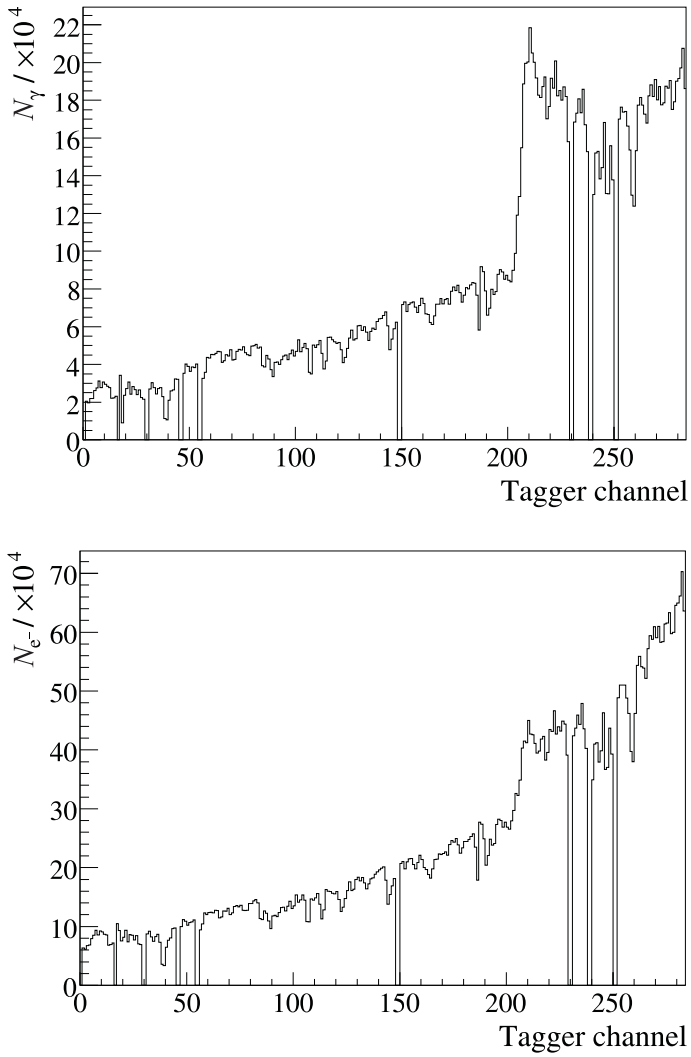

Figure 4.18: Tagger TDC hits and scaler spectra in the tagging efficiency measurements with the diamond radiator. Top: the TDC hits, which gave the number of tagged photons, N_γ, for each tagger channel. Bottom: the tagger scaler counts, which gave the total number of tagger electrons, N_{e^-}, for each tagger channel.

minutes each run. In order to estimate the influence of the tagger background on the tagging efficiency, measurements of the tagger scaler hits distribution without MAMI beam were made for about 10 minutes before and after the tagging efficiency runs. Since the conditions that influence the tagging efficiency might change while taking data, the value of $\varepsilon_{\text{tagg}}$ could evolve in time. But due to the excellent MAMI beam stability these changes were small. In fig. 4.19 (top) five measurements of the tagging efficiency taken during the second beamtime are plotted. The peak at channels 200-250 and the structure seen at smaller channel numbers are caused by the coherent photons which are concentrated in the forward direction. A good approximation to the tagging efficiency in the η production runs was obtained by averaging over all the measurements in each of the two beamtimes. Figure 4.19

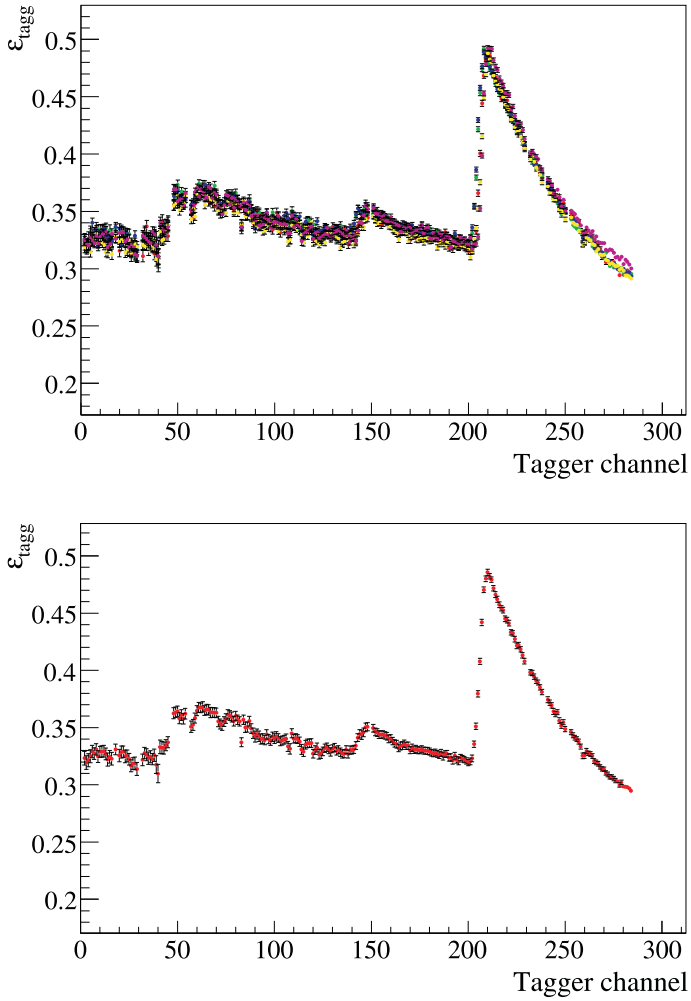

Figure 4.19: Top: five measurements of the tagging efficiency measured with the diamond radiator during two weeks in 01/2005 (MDM experiment) plotted versus tagger channel. Bottom: the tagging efficiency averaged over the five measurements.

(bottom) shows the resulting tagging efficiency for the MDM experiment beamtime after subtraction of the tagger background. During the η experiment only tagger channels 1-80 were enabled.

During the production runs of the MDM experiment a problem was observed in the TDCs of the main focal-plane detector. A comparison of the tagger TDC hits distribution in the random time window of the tagger time spectrum (see fig. 6.1) with the distribution of the tagger scaler counts made the problem apparent. Since at a TDC hit in the random time window no coincidence is required between the TDC start and stop signals, the Bremsstrahlung photon which stopped the clock was produced by a different electron, and the number of such TDC hits should be proportional to the number of scaler counts with an almost constant factor for all channels. This TDC/Scaler ratio is shown in fig. 4.20 versus the tagger channel using the data from the MDM experiment. The periodic structure every 4 and 32

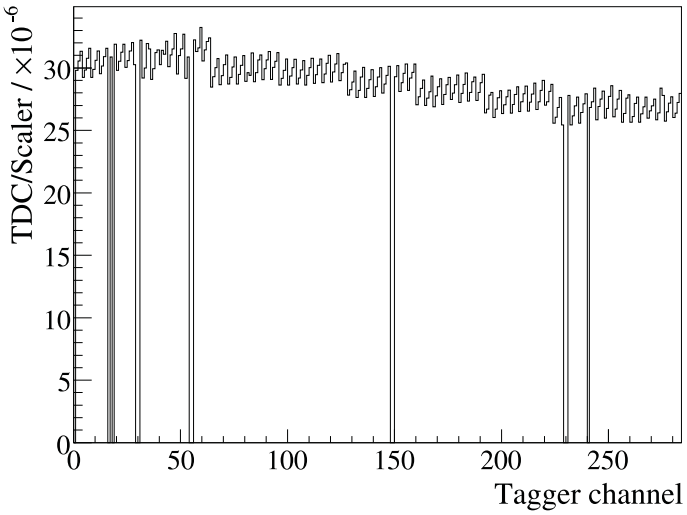

Figure 4.20: Ratio between the tagger TDC hits in the random time window and the scaler counts from the data taken in 07/2004. The periodic structure was observed systematically in all beamtimes of the MDM experiment.

channels was identical in all MDM beamtimes and also appeared in the measured total cross sections, strongly suggesting that there was a fault in the main tagger focal-plane detector electronics. The effect was systematically observed in the analyses done by other collaborators (*e. g.* [Sch07], page 110) and, unfortunately, was not adequately explained. The random TDC/Scaler ratio was used for determination of correction factors for each tagger channel obtained by dividing the value in the channel by the average value in each 4 channel group. This correction was applied to the measured total cross sections from the MDM experiment which introduced an additional systematic uncertainty estimated to be about 5%.

4.7.2 Influence of the tagger background

The main tagger focal-plane detector array consists of 353 half-overlapping scintillators. In order to minimize the background, coincident hits in adjacent scintillators, were demanded in the electronics. Nevertheless, after switching off the MAMI beam, the counting rate in the tagger was not zero. This background came mainly from activation of the beam dump after long periods of production running. At the low beam current used for the tagging efficiency measurements, this background made a significant contribution to the tagger scaler counts. To obtain a correction, this background rate was measured immediately after switching the MAMI (production) beam off and is shown as a function of time in fig. 4.21. After approximately 10-15 minutes the background rate decreased to a constant level and thereafter remained quite stable. Figure 4.22 shows typical distributions of the background in the tagger channels taken before and after a tagging efficiency measurement. The background rate is larger for higher channel numbers which are closer to the beam dump. Since

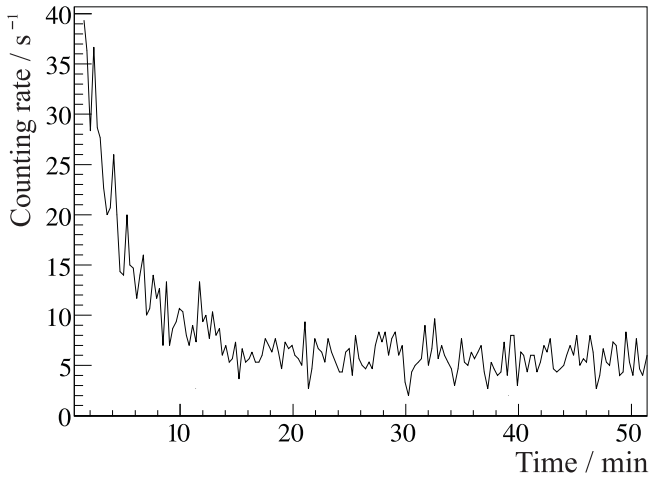

Figure 4.21: Background counting rate (16 channels OR) versus time in the main focal-plane detector directly after switching off the MAMI electron beam.

the first background measurement was taken usually directly after switching off the beam, it could give an overestimate of the background during the tagging efficiency measurement. Therefore, the second background measurement was always used in the analysis. It was normalized to the livetime of the tagging efficiency measurement and subtracted from the total counts, N_{e^-}, in the tagger scalers:

$$\varepsilon_{\mathrm{tagg}}(i) = \frac{N_\gamma(i)}{N_{e^-}(i) - N_{\mathrm{backgr}}(i)}, \tag{4.42}$$

where $N_{\mathrm{backgr}}(i)$ is the normalized measured background number of counts. For this normalization the computer clock provided the background counting time, and it was assumed that there was no deadtime at low trigger rate (about 5 Hz) used in the background runs. The background subtraction increased the resulting tagging efficiency by about 0.5%.

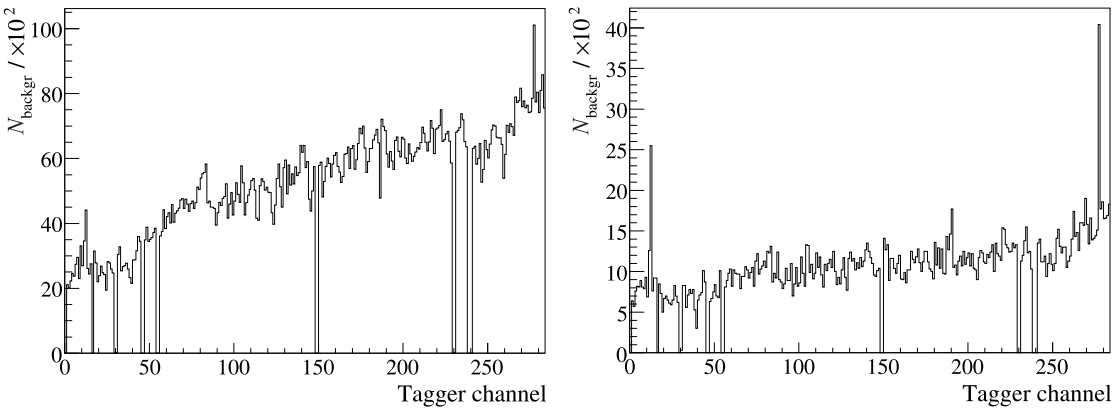

Figure 4.22: The number $N_{\mathrm{backgr}}(i)$ of background counts in the tagger scalers taken before a tagging efficiency measurement (left) and after it (right), both measured for about 10 min.

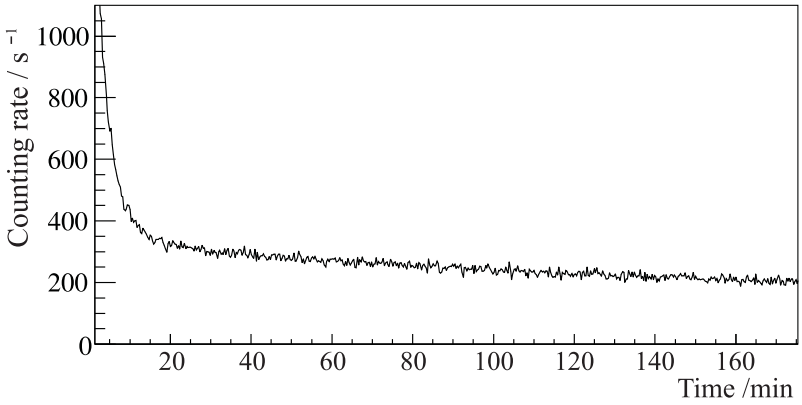

Figure 4.23: Tagger microscope background counting rate (96 strips OR) taken directly after switching off the MAMI beam. The counting rate, caused by emission from the beam dump, decreased slowly for several hours.

4.7.3 Effective tagging efficiency for the tagger microscope

In this experiment, the tagger microscope was used for the first time for determination of nuclear cross sections. It provided better photon energy resolution than was available from the main focal-plane detector. The tagger microscope was equipped with electronics independent from the main tagger readout (section 3.6.1); therefore, the photon flux had to be determined separately.

In contrast to the main focal-plane (FP) detector, the electronics of the tagger microscope did not require a coincidence between adjacent single microscope strips, and, therefore, the microscope detector was prone to background and electronic (or optical) noise to a greater extent than the main FP detector. Similar to the main FP detector, each microscope strip was equipped with a scaler. At low incident electron beam current during the tagging efficiency measurements, the counting rate in the scalers of the microscope strips was about $15\,\mathrm{s}^{-1}\,\mathrm{MeV}^{-1}$. In the main FP detector array it was possible to correct for the small background contribution using the time-normalized measurement without beam as explained in section 4.7.2. In the microscope, however, the background was much higher and decreased only slowly over several hours (see fig 4.23). Estimates based on "beam off" measurements before and after the tagging efficiency runs gave background rates of up to $8\,\mathrm{s}^{-1}\,\mathrm{MeV}^{-1}$ in the microscope scalers, *i. e.* up to about 50% of the scaler counts in the "beam on" runs. Since this rate was not constant, it was not possible to determine and subtract time-normalized background as was done for the main FP detector. This made the determination of the photon flux for the microscope detector using the tagging efficiency measurements as described in section 4.7.1 inappropriate; an alternative method for determination of the photon flux had to be investigated.

Similar to equation (4.39) for the main FP detector, the photon flux $n_\gamma(i)$ for the 191 channels of the tagger microscope was determined using

$$n_\gamma(j) = n_{e^-}(j) \cdot \varepsilon'_{\mathrm{tagg}}(j), \tag{4.43}$$

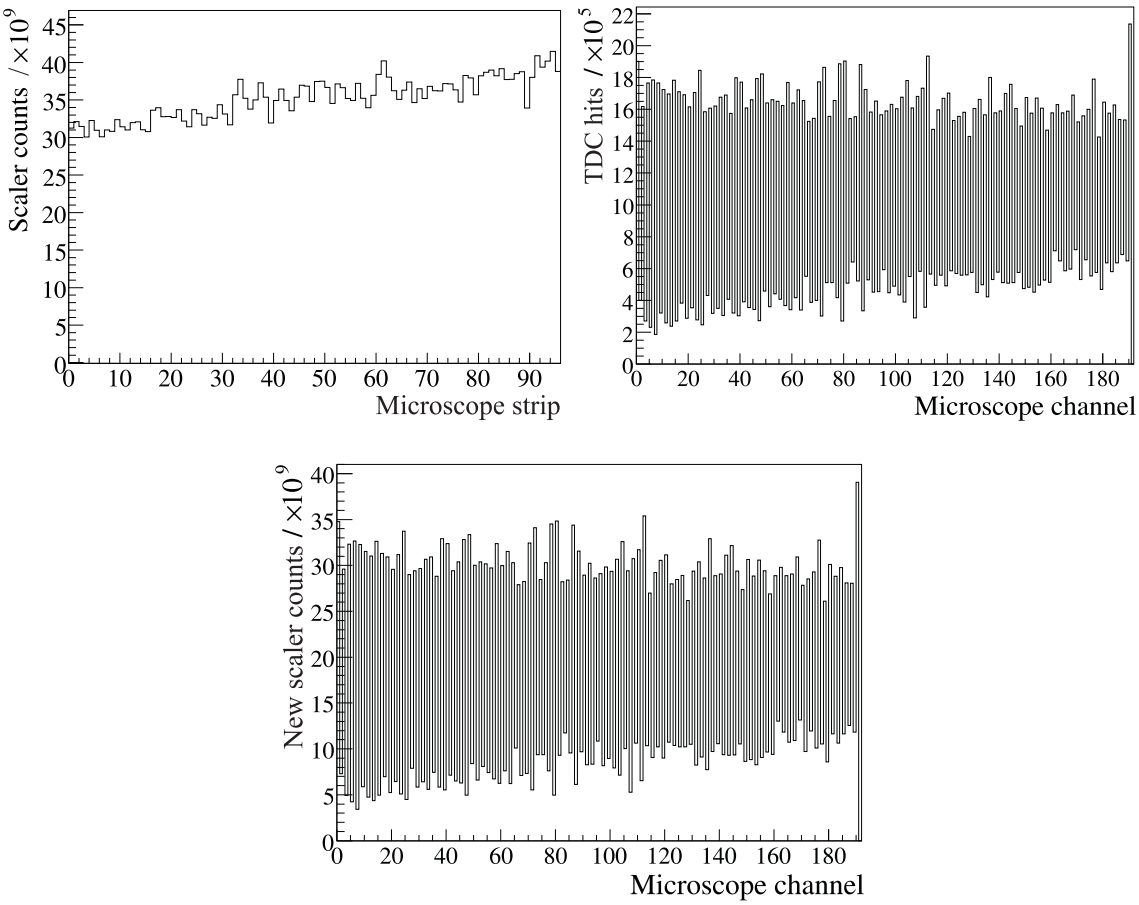

Figure 4.24: Top: the distribution of counts in the scalers of the 96 microscope strips in the production runs (left) and the TDC hits distribution in the random window of the tagger time spectrum in the 191 channels (right). Bottom: the distribution of the microscope scaler counts rebinned from 96 strips to 191 channels.

where $n_{e^-}(j)$ is the number of tagger electrons for microscope channel j, given by the scaler counts, and $\varepsilon'_{\text{tagg}}(j)$ is an effective tagging efficiency. However, the scalers in the tagger microscope gave the counts for the 96 strips rather than for the 191 channels, and tagging electrons in the microscope double-hit channels (see section 3.3) were registered in both adjacent strip scalers. Thus, the hits distribution in the 96 scalers (see fig. 4.24 left) had to be rebinned to give the scaler counts for the 191 channels. This rebinning was done with the aid of the distribution of the microscope TDC hits in the production runs (see fig. 4.24 right) in the random region of the tagger microscope coincidence spectrum (random TDC hits). The scaler counts should be proportional to the random TDC hits with a constant factor for all channels, since in this case no conditions on the tagged photons are demanded. Therefore, the sum of the 96 strip scalers was distributed between the 191 channels, so that the ratio between the random TDC hits and the scaler counts was constant for all channels. This gave the values $n_{e^-}(j)$ for the 191 microscope channels shown in

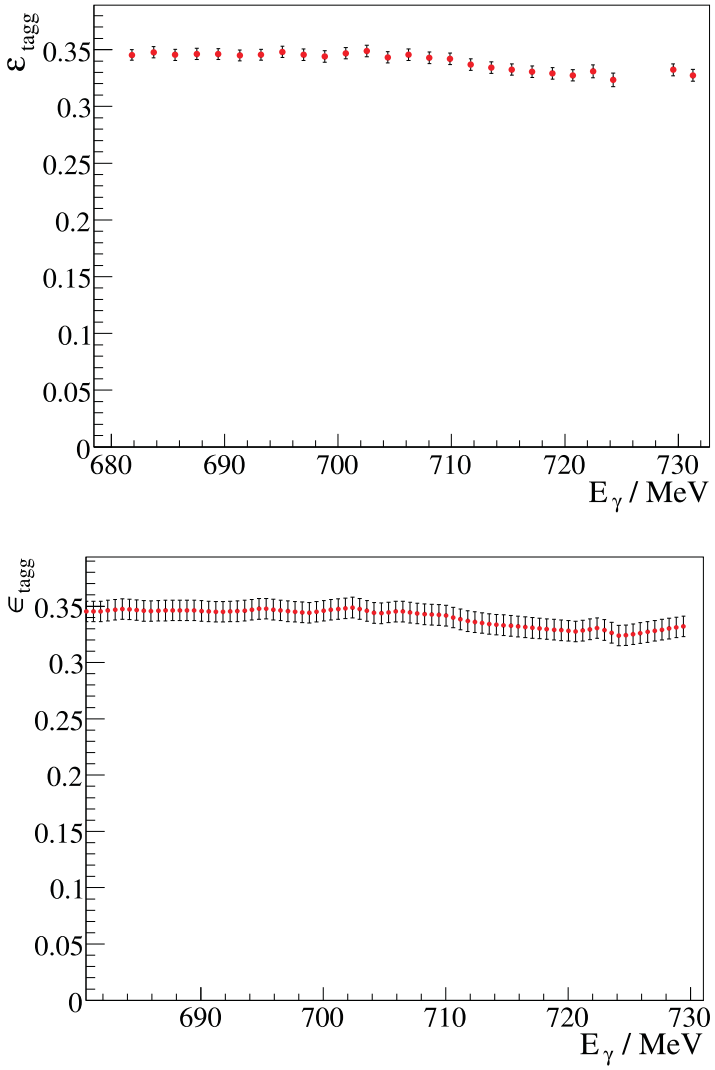

Figure 4.25: Top: the tagging efficiency for the main focal-plane detector in the region overlapping with the tagger microscope. Bottom: the tagging efficiency interpolated for the tagger microscope.

fig. 4.24 bottom. However, $n_{e^-}(j)$ is not the actual number of tagging electrons, but is proportional to it. Therefore, the effective tagging efficiency $\varepsilon'_{\text{tagg}}(j)$ in equation (4.43) can differ from the tagging efficiency $\varepsilon_{\text{tagg}}(i)$, discussed in section 4.7.1, by a constant factor,

$$\varepsilon'_{\text{tagg}}(j) = \lambda \cdot \varepsilon_{\text{tagg}}(i) = \lambda \cdot \epsilon_{\text{tagg}}(j), \tag{4.44}$$

where i is the main FP detector channel corresponding to microscope channel j, and $\epsilon_{\text{tagg}}(j)$ is the tagging efficiency $\varepsilon_{\text{tagg}}(i)$ (see fig. 4.25 top) interpolated for microscope channel j. The interpolated tagging efficiency $\epsilon_{\text{tagg}}(j)$ for the 191 microscope channels is shown in fig. 4.25 bottom.

In order to find the factor λ and to ensure that the microscope and the main FP array produce identical results for the cross sections, the number of random-

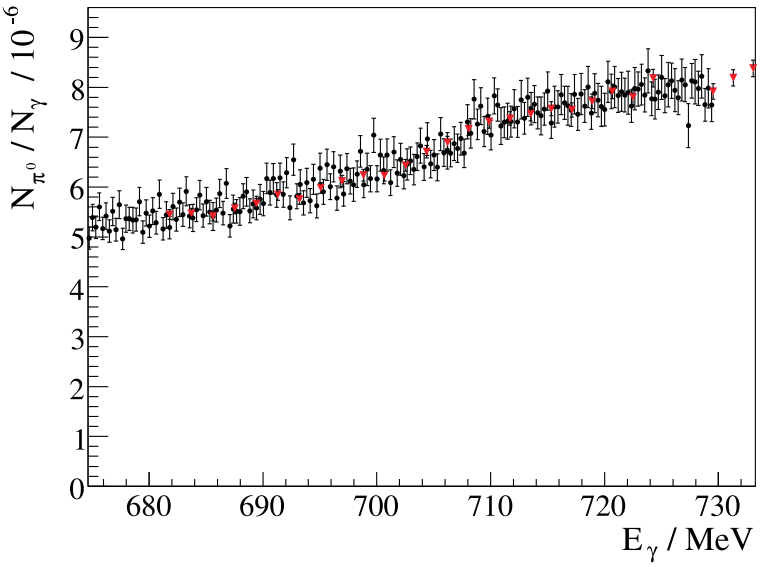

Figure 4.26: The random-subtracted prompt number of π^0 events divided by the photon flux obtained with the main tagger focal-plane array (red triangles) and with the microscope focal-plane detector (black circles) after optimizing the value of λ (see text).

subtracted prompt events from the reaction $\gamma p \to p\pi^0$ was found. This reaction has a well-known smoothly changing cross section in the η threshold region. The number of π^0 events divided by the photon flux should give the same result for both detectors,

$$\frac{N_{\pi^0}(i)}{N_{e^-}(i)\ \varepsilon_{\mathrm{tagg}}(i)} = \frac{n_{\pi^0}(j)}{n_{e^-}(j)\ \varepsilon'_{\mathrm{tagg}}(j)}\,, \tag{4.45}$$

where $N_{\pi^0}(i)$ is the number of π^0 events for the main FP detector channel i, and $n_{\pi^0}(j)$ is the number of π^0 events for the microscope channel j, respectively. This ratio is plotted in fig. 4.26. The factor λ was found by minimizing the RMS deviation of the points obtained with the microscope from the kinked line which connects the points of the main FP detector, and the result

$$\lambda = 0.790 \pm 0.004 \tag{4.46}$$

was obtained. The very good agreement between the points in fig. 4.26 ensured that the main FP detector and the microscope produce consistent results. The effective tagging efficiency for the tagger microscope introduced additional systematic uncertainty of about 0.5% to the total cross sections.

Chapter 5

Simulation

For determination of the absolute cross section of a physical reaction from the number of reconstructed events, the acceptance of the experimental detector was important. While taking the data, some of the events can be lost already during the experiment because of the detection efficiency of single detectors or the energy thresholds of the trigger or readout electronics. Other events are removed by the kinematic cuts needed to select a specific reaction. Thus the number of surviving reconstructed events must be normalized in order to determine the real number of events produced by a specific reaction in the experimental target.

The total acceptance of the detector setup and analysis can be found by simulation of the experiment with an exactly known number of events. The simulation of the detector response is a two step process as shown in fig. 5.1. In the first step the event generator is implemented which produces the 4-vectors of the decay photons from the kinematics of the investigated reaction. In this step it is necessary to generate initial distributions, based on the real cross section and angular distribution for the reaction concerned. The next step is performed using a program written in FORTRAN, using the CERN GEANT 3.21 simulation library, where all features of the detector setup and target are modeled in a virtual detector setup. The program tracks the reaction products through the virtual detector setup, where they interact with the detector materials. The energy deposition in the detector components is registered and stored in binary files, which then are analyzed with AcquRoot 3v17 [Ann05], as explained in chapter 4. Comparisons of the distributions of different observables, obtained from the real and simulated data, are presented in chapter 6.

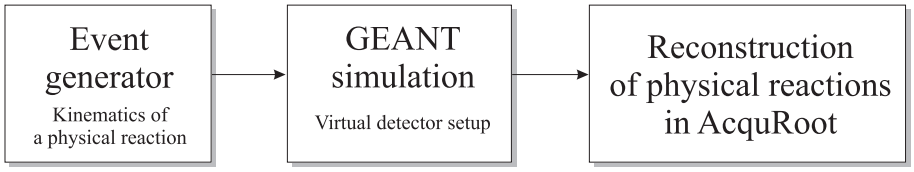

Figure 5.1: Simulation of the experiment was performed in two steps: event generation and simulation of the detector response in the GEANT based program.

The experiment trigger made also a contribution to the overall efficiency of the data analysis, thus its simulation was implemented in the analysis step. The software simulation of the trigger system is described in [Unv08].

5.1 Event generation

In order to produce the large number of events, needed as input for the GEANT simulation, an event generator program was used. A reliable simulation of the experiment can be performed only if the properties (energy and angular distributions) of the simulated reactions correspond well to the real physical reactions. This section shows how the appropriate start distributions of the events were constructed from the kinematical description of the physical process.

The input channel for every possible reaction in the hydrogen target is γp, where the rest target proton p has well-known mass m_p and the incident Bremsstrahlung photon γ is described by its energy E_γ (in the laboratory frame). The energy of the photon is generated from the reaction production threshold up to the maximum energy $E_\gamma = 820\,\mathrm{MeV}$ for the main tagger or up to $E_\gamma = 730\,\mathrm{MeV}$ for the tagger microscope using the Bremsstrahlung $1/E_\gamma$-weighted distribution.

5.1.1 Reaction $\gamma p \to p\pi^0$

The simulation of the $\gamma p \to p\pi^0$ reaction was necessary for determination of the acceptance for the cross section and the background contribution that it made to the selected η events. The energy and angular distribution of the simulated π^0 production was based on the theoretical prediction of the MAID [Web02, Dre99] model for the unpolarized differential cross section given by

$$\frac{d\sigma}{d\Omega_{\pi^0}} = \frac{1}{2\pi \sin\theta_{\pi^0}} \cdot \frac{d\sigma}{d\theta_{\pi^0}}\,. \tag{5.1}$$

Because of the azimuthal symmetry, the kinematics of the 2-body process $\gamma p \to p\pi^0$ is completely determined by two variables: the incident photon energy E_γ and the polar angle θ_{π^0} of the pion. For a given photon energy, E_γ, and polar angle, θ_{π^0}, the magnitude of the cross section represents the probability that the reaction occurs. Using the MAID prediction for the π^0 photoproduction cross section, the 2-dimensional distribution of the probability $d\sigma/d\theta_{\pi^0}$ was produced according to equation (5.1) and then normalized to the maximum within the investigated parameter space (see fig. 5.2). This distribution was used by the event generator to simulate the cross section for the physical process.

For each incident photon energy E_γ, generated earlier using the Bremsstrahlung distribution, and randomly generated pion polar angle $\theta_{\pi^0} \in [0, \pi]$ in the center-of-mass frame, a random azimuthal angle $\phi_{\pi^0} \in [0, 2\pi]$ was also selected. For each set of the parameters (E_γ, θ_{π^0}, ϕ_{π^0}), the probability $P(E_\gamma, \theta_{\pi^0})$ was calculated using the 2-dimensional distribution in fig. 5.2, which was compared to a random number

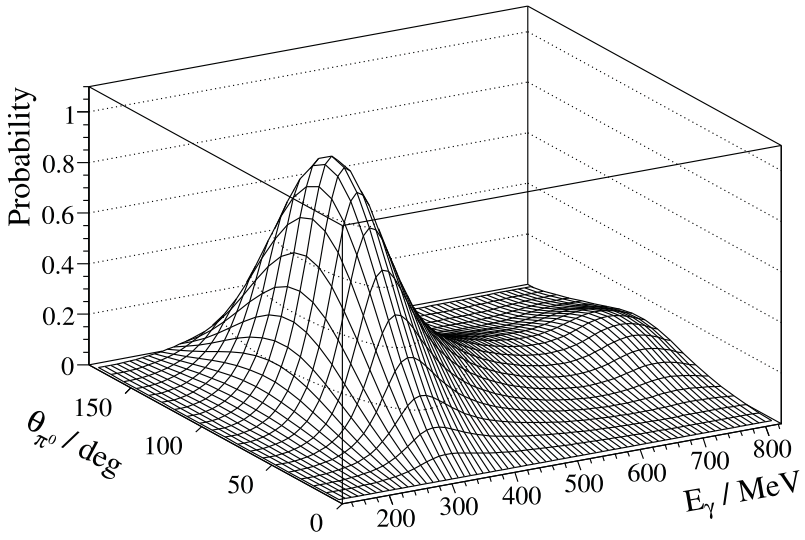

Figure 5.2: Two-dimensional distribution of the probability for reaction $\gamma p \to p\pi^0$ as a function of the incident photon energy E_γ and the polar angle θ_{π^0} of the pion, based on the prediction of the MAID [Web02, Dre99] model.

$p \in [0, 1]$. The event was accepted if the value of p was smaller than the predicted probability $P(E_\gamma, \theta_{\pi^0})$, otherwise a new set of the parameters was generated.

The set of the parameters (E_γ, θ_{π^0}, ϕ_{π^0}) was enough to completely define the kinematics of the process. The energy and momentum conservation laws allowed determination of the 4-vectors of the pion (E_{π^0}, $\vec{p}_{\pi^0}$) and proton (E_p, $\vec{p}_p$) in the output channel. In the center-of-mass (c. m.) frame the energy E_{π^0} of the pion and energy E_p of the proton give the total energy W of the system before the collision,

$$E_{\pi^0} + E_p = W\,, \tag{5.2}$$

with the total energy W in the c. m. frame

$$W = \sqrt{m_p^2 + 2\,m_p E_\gamma}\,. \tag{5.3}$$

From momentum conservation in the c. m. frame follows

$$\vec{p}_{\pi^0} + \vec{p}_p = 0 \quad \Rightarrow \quad \vec{p}_{\pi^0}^{\,2} = \vec{p}_p^{\,2} \quad \Rightarrow \quad E_p^2 - m_p^2 = E_{\pi^0}^2 - m_{\pi^0}^2\,. \tag{5.4}$$

By solving the equations (5.2) and (5.4), one obtains the energies

$$E_p = \frac{W^2 + m_p^2 - m_{\pi^0}^2}{2W} \quad \text{and} \quad E_{\pi^0} = \frac{W^2 + m_{\pi^0}^2 - m_p^2}{2W}\,. \tag{5.5}$$

The absolute values of the momenta are given by

$$|\vec{p}_p| = \sqrt{E_p^2 - m_p^2} \quad \text{and} \quad |\vec{p}_{\pi^0}| = \sqrt{E_{\pi^0}^2 - m_{\pi^0}^2}\,, \tag{5.6}$$

where the vectors $\vec{p}_p$ and $\vec{p}_{\pi^0}$ have opposite directions, defined by the angles θ_{π^0} and ϕ_{π^0}. Then the 4-vectors (E_{π^0}, $\vec{p}_{\pi^0}$) and (E_p, $\vec{p}_p$) were transformed to the laboratory

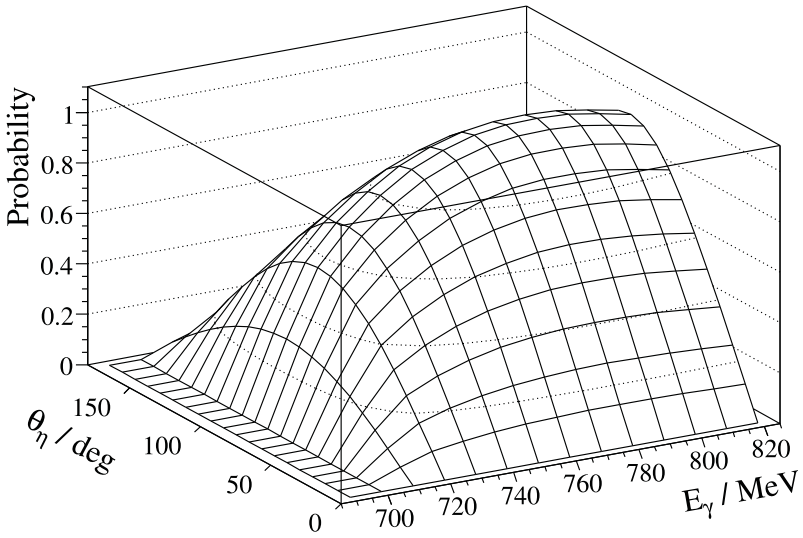

Figure 5.3: Two-dimensional distribution of the probability for reaction $\gamma p \to p\eta$ as a function of the incident photon energy E_γ and the polar angle θ_η of the η meson, based on the prediction of the ETA-MAID [Web03, Chi03] model.

frame using the Lorentz boost. The 4-vector of the proton and π^0 meson were stored in a data file, which then was used by the GEANT simulation program, which handled the decay of the pion into two photons and finally tracked the particles through the virtual detector system.

5.1.2 Reaction $\gamma p \to p\pi^0\pi^0$

$\pi^0\pi^0$ photoproduction was simulated in order to determine the background contribution that it made to the selected η events. For this reaction a phase space distribution of the 3-body decay was assumed. The calculation of the decay was performed using the utility class *TGenPhaseSpace*[1], included in the ROOT libraries, which allowed generation of n-body decay of a particle with constant cross section. The dependence of the cross section on the photon energy was based on the experimentally measured cross section from [Kot01].

The cross section for the reaction $\gamma p \to p\pi^0\pi^0$, normalized to the maximum, gave a 1-dimensional distribution of the probability $P(E_\gamma)$, which was compared to a randomly generated factor $p \in [0, 1]$. This led to a combination of the Bremsstrahlung distribution of the incident photon with the cross section of the $\pi^0\pi^0$ production. The intermediate state, which resulted from absorption of the photon by the proton, then decayed into a proton and two π^0 mesons. The 4-vectors of the final state, transformed to the laboratory frame, were passed to the simulation.

[1]This class takes the 4-vector of the intermediate state, which results from absorption of the photon by the proton, in the laboratory frame and the masses of decay particles as input parameters, calculates the decay in the center-of-mass frame, and finally transforms the 4-vectors of the decay particles into the laboratory frame.

Reaction	E_γ	Number of events	Reason
$\gamma p \to p\pi^0$	200 - 820 MeV	$10 \cdot 10^6$	Acceptance
$\gamma p \to p\eta \to p\gamma\gamma$	707 - 820 MeV	$10 \cdot 10^6$	Acceptance
$\gamma p \to p\eta \to p\gamma\gamma$	707 - 730 MeV	$10 \cdot 10^6$	Acceptance (microscope)
$\gamma p \to p\eta \to p\,3\pi^0$	707 - 820 MeV	$10 \cdot 10^6$	Acceptance
$\gamma p \to p\eta \to p\,3\pi^0$	707 - 730 MeV	$10 \cdot 10^6$	Acceptance (microscope)
$\gamma p \to p\pi^0$	670 - 820 MeV	$5 \cdot 10^6$	Background
$\gamma p \to p\pi^0\pi^0$	670 - 820 MeV	$5 \cdot 10^6$	Background

Table 5.1: Number of generated events for the investigated reactions. The events in the photon energy region, covered by the microscope, were generated separately.

5.1.3 Reaction $\gamma p \to p\eta$

The event generation for the η photoproduction was very similar to the π^0 photoproduction, described earlier. A 2-dimensional energy-angular distribution of the simulated η mesons was based on the theoretical prediction of the ETA-MAID [Web03, Chi03] model for the unpolarized differential cross section. The 2-dimensional distribution of the probability $P(E_\gamma, \theta_\eta)$, normalized to the maximum within the investigated parameter space, is shown in fig. 5.3. Finally, the two neutral decays $\eta \to 2\gamma$ and $\eta \to 3\pi^0$ were generated.

The decay $\eta \to 2\gamma$ is described by simple 2-body kinematics. In the η meson c. m. frame the two photons with 4-vectors $(E_{\gamma 1}, \vec{p}_{\gamma 1})$ and $(E_{\gamma 2}, \vec{p}_{\gamma 2})$ have the total energy and momentum

$$\begin{cases} E_{\gamma 1} + E_{\gamma 2} &= m_\eta \\ \vec{p}_{\gamma 1} + \vec{p}_{\gamma 2} &= 0\,. \end{cases} \tag{5.7}$$

Since the mass of the photon is zero, solving the equations (5.7), one obtains

$$E_{\gamma 1} = E_{\gamma 2} = |\vec{p}_{\gamma 1}| = |\vec{p}_{\gamma 2}| = m_\eta/2\,. \tag{5.8}$$

In the η meson rest frame the decay photons are emitted in opposite directions, defined by the polar, θ_γ, and azimuthal, ϕ_γ, angles and have an isotropic distribution given by

$$\begin{aligned} \theta_\gamma &= \arccos(-1 + 2\,c_1)\,, \\ \phi_\gamma &= 2\pi\,c_2\,, \end{aligned} \tag{5.9}$$

where the numbers $c_1, c_2 \in [0, 1]$ are randomly generated. The Lorentz boost into the laboratory frame delivered the 4-vectors of the two decay photons, which together with the 4-vector of the proton were stored in a data file, passed to the simulation.

The kinematics of the $\eta \to 3\pi^0$ decay was calculated with the *TGenPhaseSpace* utility class, which took the 4-vector of the η meson in the laboratory frame and the π^0 rest mass and returned the three 4-vectors of the decay pions. The decays of the pions into photons were handled by the GEANT simulation. Table 5.1 gives an overview of all generated events.

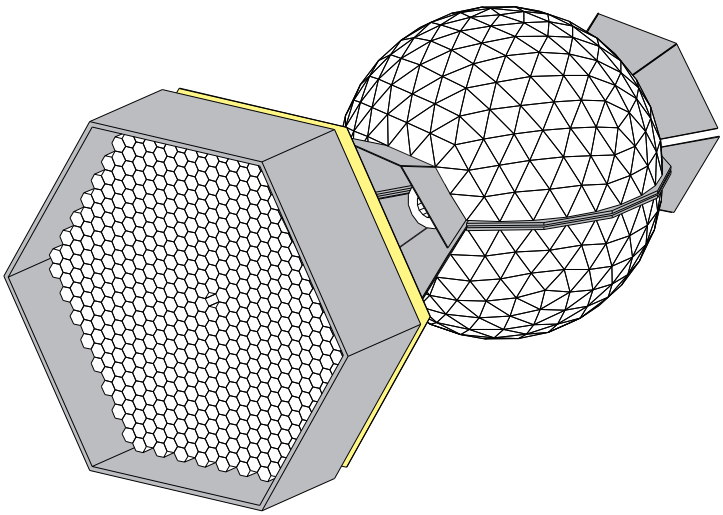

Figure 5.4: Geometry of the experimental detector setup in the GEANT simulation.

5.2 Experimental setup geometry

All descriptions presented in the previous section were implemented in the event generator program, which produced the 4-vectors of all decay products and stored them in binary files. These files were used by the simulation program written in FORTRAN using the CERN GEANT 3.21 library. As starting point for implementation of the virtual detector setup for the GEANT simulation, the existing Crystal Ball geometry [Cla97] was used, which was changed and adapted for the experimental setup in Mainz. Various improvements were necessary which included not only the detector itself, but also the elements (support frames, cables, and electronics) that could influence the response of the detector. Especially the beam out region and tunnel needed to be thoroughly revised. These changes were implemented and tested by V. Kashevarov, S. Lugert [Lug07], S. Schumann [Sch07], and M. Unverzagt [Unv08] and are briefly summarized below.

The geometry of the experimental detector setup is shown in fig. 5.4. The implementation of the geometry was made according to the detector descriptions, presented in chapter 3. Simulation of the photon tagger was not necessary, since the Bremsstrahlung photons were already defined in the event generator. Thus the components to be modeled included the target, MWPCs, PID, CB, and TAPS. The passive materials of the target and MWPCs were also included, but only to reproduce the correct energy loss of the particles before they reached the detector. Support structures included the CB stainless steel frame, passive material in the CB beam out region (to mock-up the cables), the aluminum frame of TAPS, blind BaF_2 detectors and the light guides for readout of the TAPS veto system.

Chapter 6

Reconstruction of physical reactions

The calibration of the detector setup, described in the previous chapter, allowed conversion of the raw experimental data, consisting of detector ADC and TDC hits, into physical values like energies and times. Usually a particle, which hit the detector, produced an electromagnetic shower and induced a signal not just in one crystal but in a group of adjacent crystals forming a cluster (see section 4.2). Clusters were identified as photons in the Crystal Ball detector with the aid of the PID. The azimuthal angle of the Crystal Ball cluster was compared with the ϕ-angle of a hit in a PID element. If the difference between the angles of the cluster and a PID hit was less than about 8-10°, the cluster was identified as a charged particle. All other clusters were taken to be photons. Using the energy and angle of the cluster, the 4-vectors of the detected particles were determined without any assumption concerning the reaction. With the 4-vectors it was possible to calculate different properties of the original decaying particles such as angles, energies, invariant masses *etc.* Calculation of the missing mass required the information about the input channel of the observed reaction, which consisted of a target proton and an incident photon. The energy of the photon was determined with the photon tagger. Clear assignment of the energy information of the tagging system to the photon was not possible, since usually several tagging electrons were registered for each event in the Crystal Ball/TAPS. In the beginning of this chapter it is shown how this ambiguity was resolved using time coincidence analysis.

All reconstruction steps, described in this chapter, were applied not only to the experimental data but also to the simulated data, which were reconstructed in the same way in order to determine the acceptance for the observed reactions. All plots obtained from the simulated data were compared to the experimental data in order to verify that the simulation gave a good description of the experiment.

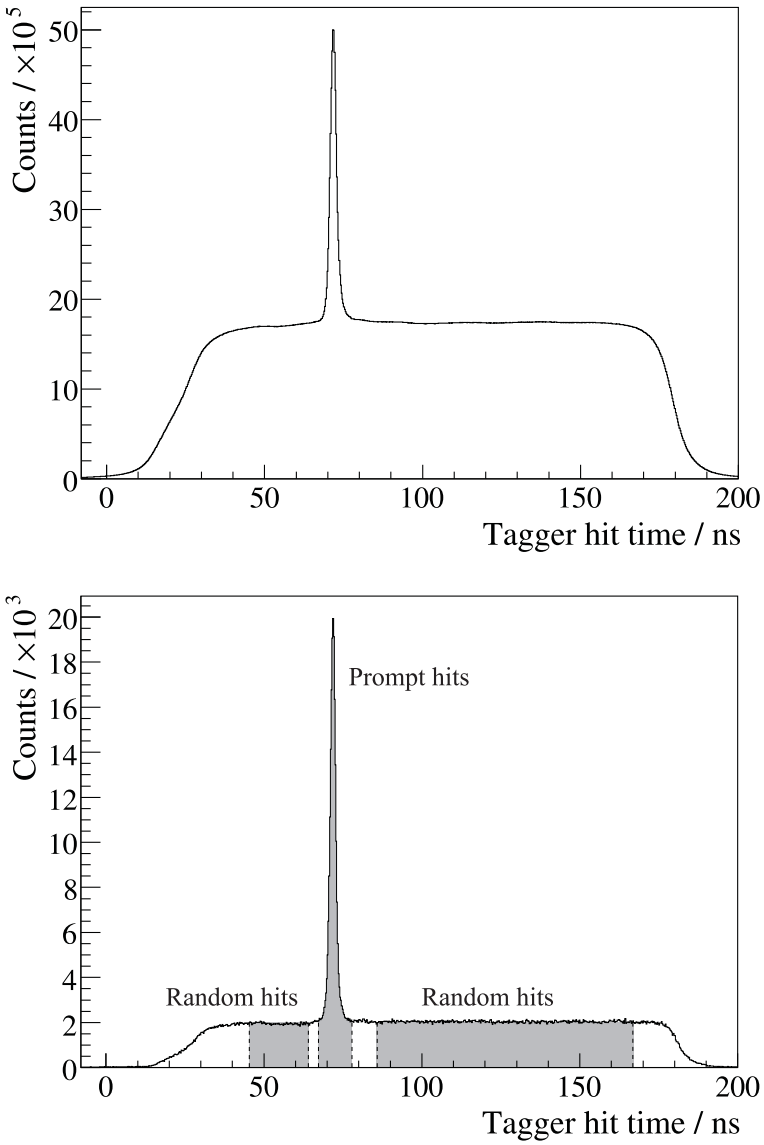

Figure 6.1: The timing distribution of the tagger hits. The x axis is the relative time of the tagger hits with respect to the average time of the Crystal Ball event. Top: all tagger hits. Bottom: tagger hits for events registered as $\gamma p \to p\eta$.

6.1 Coincidence analysis

The high electron beam current (about 35 nA) during the η experiments caused several hits to be registered in the tagger focal-plane detector for each event. These electron hits originated from the 160 ns wide time window of the tagger latches, which were started by the L1 trigger, but only one of these electrons was correlated to the photon which induced the reaction and generated the trigger for the event. This electron hit came at a fixed time relative to the trigger. The aligned time distribution of all tagger hits with respect to the trigger is shown in fig. 6.1. It can

be seen that the spectrum is composed of two parts: a flat background of random coincidences and a prompt peak, which is due to the coincident photons involved in the reaction. If it is assumed that the random background under the prompt peak is a continuation of the background on either side, one can obtain the number of true coincidences by sampling events for two regions: the prompt region, containing the peak and the random background underneath it, and the random region, containing the random background only. These time windows are shown as gray areas in fig. 6.1. The number of random hits was scaled using the ratio of the region widths to give a sample equivalent to that expected under the prompt peak. The relative width of the prompt and random region was 1:7 for π^0 production and 1:11 for η production. In the production of any physical spectrum, *e. g.* the invariant mass of the detected particle, this scaled random sample was subtracted from the prompt sample to obtain the result due to the prompt photons.

Figure 6.1 shows that the relative number of random coincidences can be changed by selection of events from a specific reaction. The top figure shows all events in the tagger, and the bottom one shows the distribution for events identified as coming from the reaction $\gamma p \to p\eta$ (decay $\eta \to 3\pi^0$). Each tagger hit was converted to the corresponding photon energy, and only kinematically possible tagger hits were accepted as shown in the following sections.

6.2 Reaction $\gamma p \to p\pi^0$

The reaction $\gamma p \to p\pi^0$, due to its large cross section in the region of the $P_{33}(1232)$ resonance and simple two body kinematics, was the simplest reaction available for reconstruction. In this work single π^0 production was used for tests of different absolute normalization factors and to check the analysis of the data by comparing the results with known cross sections and theoretical predictions.

The reconstruction of the reaction $\gamma p \to p\pi^0$ concentrated on events with a cluster multiplicity $\mathrm{M} \geq 2$ in the L2 trigger. This trigger condition was usually already fulfilled by the decay photons of the π^0 meson, so that unlike the events with trigger condition $\mathrm{M} \geq 3$, detection of the third particle was not needed. The first analysis step consisted of identification and reconstruction of the π^0 meson by the decay $\pi^0 \to 2\gamma$. Having a branching ratio of 98.8%, this decay channel is dominant. The information about the two detected photons, the incident photon, and the target proton completely defines the kinematics of the reaction. The 4-vectors of the decay photons $(E_{1,2}, \vec{p}_{1,2})$ were used to find the invariant mass $M_{\gamma\gamma}$ of the original particle:

$$M_{\gamma\gamma} = \sqrt{(E_1 + E_2)^2 - (\vec{p}_1 + \vec{p}_2)^2}. \tag{6.1}$$

The input channel of the reaction is defined by the target proton with mass m_p and the incident photon with energy E_γ, which can be treated as a known value with the aid of the coincidence analysis. Since the two body reaction with known input channel can be fully determined by measuring the 4-vector of one particle in the

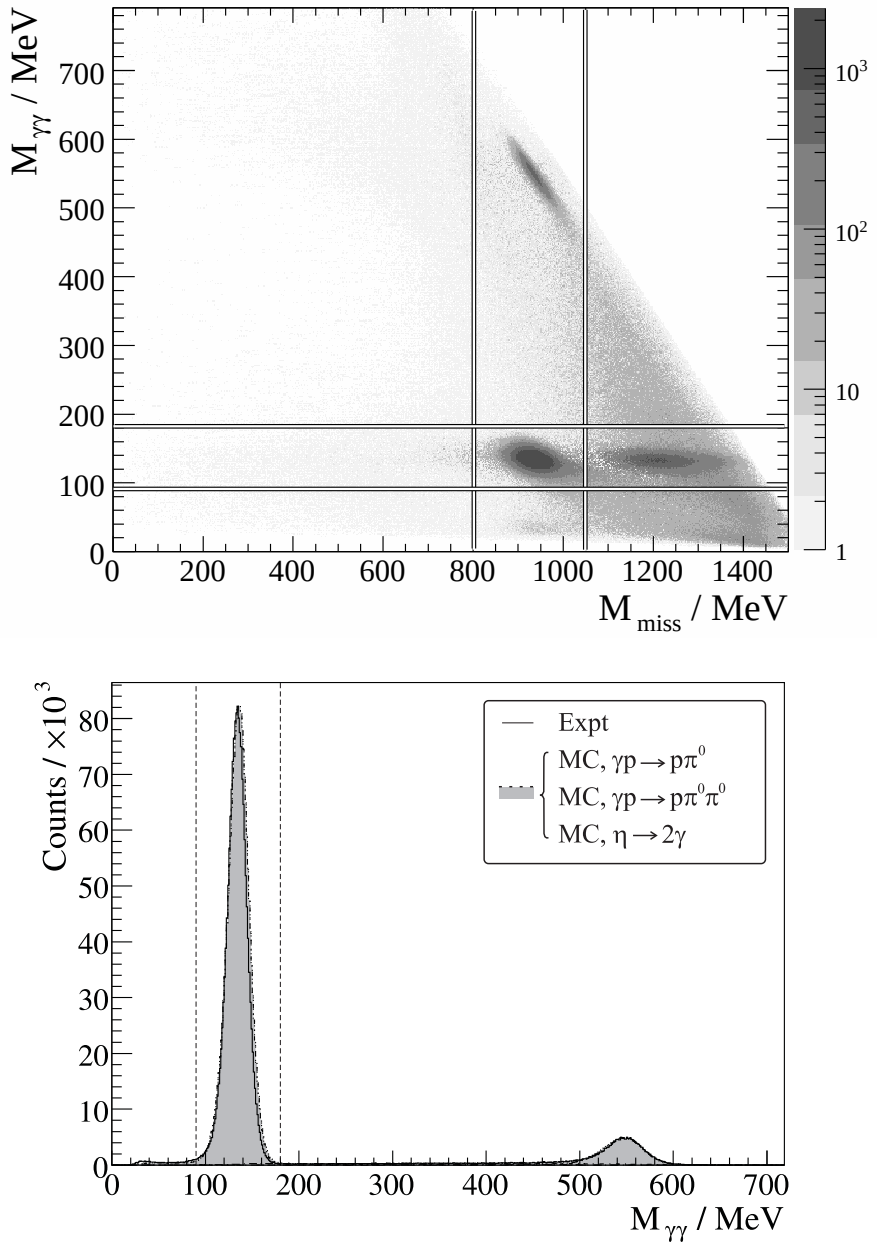

Figure 6.2: Top: two-photon invariant mass $M_{\gamma\gamma}$ plotted versus the missing mass M_{miss} for photon energies 682 MeV $< E_\gamma <$ 820 MeV. Bottom: two-photon invariant mass after a cut on the missing mass 800 MeV $< M_{\text{miss}} <$ 1020 MeV. The shaded histogram was produced by the Monte Carlo simulation.

final state, one can calculate, for example, the missing mass M_{miss} of the undetected particle, a proton in our case, from the difference between the 4-vectors $(E_{i,f}, \vec{p}_{i,f})$ in the initial and final states:

$$M_{\text{miss}} = \sqrt{(E_f - E_i)^2 - (\vec{p}_f - \vec{p}_i)^2}. \tag{6.2}$$

Since the coincidence analysis implies several values for E_γ in prompt and random time windows, the value of M_{miss} was found for each photon energy. This resulted in several "prompt" and "random" values of the missing mass for each value of the invariant mass. The distribution of the missing mass was found in prompt and random tagger time windows and finally subtracted. The 2-dimensional distribution of the missing mass versus the two-photon invariant mass after subtraction is plotted in fig. 6.2 top. It can be seen that the majority of the observed events generated a missing mass close to the proton mass $m_p = 938.27\,\text{MeV}$. Another peak at $M_{\text{miss}} \approx 1200\,\text{MeV}$ is presumably due to the $P_{33}(1232)$ resonance, which is produced only at high incident photon energy. The background, widely distributed at high missing masses, is mainly due to competitive reactions with more than two particles in the final state, such as $\pi^0\pi^0$ production, which had no defined missing mass to expect. Such background reactions were suppressed by a cut on the missing mass 800 - 1020 MeV. After the cut, the distribution of the two-photon invariant mass $M_{\gamma\gamma}$ is shown in fig. 6.2 bottom. The distribution is dominated by a peak at $M_{\gamma\gamma} \approx 135\,\text{MeV}$ corresponding to the mass of the π^0 meson. Another peak at $M_{\gamma\gamma} \approx 548\,\text{MeV}$ originates from the η meson decay $\eta \to 2\gamma$. The events, reconstructed from the two photons with an invariant mass $M_{\gamma\gamma}$ between 90 MeV and 180 MeV, were accepted as candidate π^0 mesons.

The main source of background events was $\pi^0\pi^0$ production with two escaping photons. Despite of the large angular acceptance of the Crystal Ball, these events could not be fully filtered out in the analysis. However, such a combination of the photons originating from different π^0 mesons usually generated an invariant mass larger than 150 MeV, and the simulation showed that after all the cuts the background $\pi^0\pi^0$ events made only about 0.5% of the π^0 events.

6.3 Reaction $\gamma p \to p\eta$

The η mesons were identified via their two main decay modes, $\eta \to 2\gamma$ (BR = 39.31%) and $\eta \to 3\pi^0$ (BR = 32.56%). In the first step of the analysis, events with two and six coincident photons were selected to pick out candidate η events.

6.3.1 Decay channel $\eta \to 2\gamma$

The identification of the $\eta \to 2\gamma$ decay concentrated on events with a trigger multiplicity $\text{M} \geq 2$ and two clusters detected as photons, ignoring all other particles. The standard invariant mass analysis using equation (6.1) showed a peak at the η mass with a resolution of $\sigma \approx 20\,\text{MeV}$. Using the tagger hits in the prompt and random time windows, the distribution of the missing mass M_{miss} of the undetected particle (proton) was produced (fig. 6.3 bottom). Cuts were applied on the invariant mass at $M_{\gamma\gamma} > 480\,\text{MeV}$ and on the missing mass at $M_{\text{miss}} > 880\,\text{MeV}$. The two-photon invariant mass $M_{\gamma\gamma}$ distribution after the cut on the missing mass and subtraction

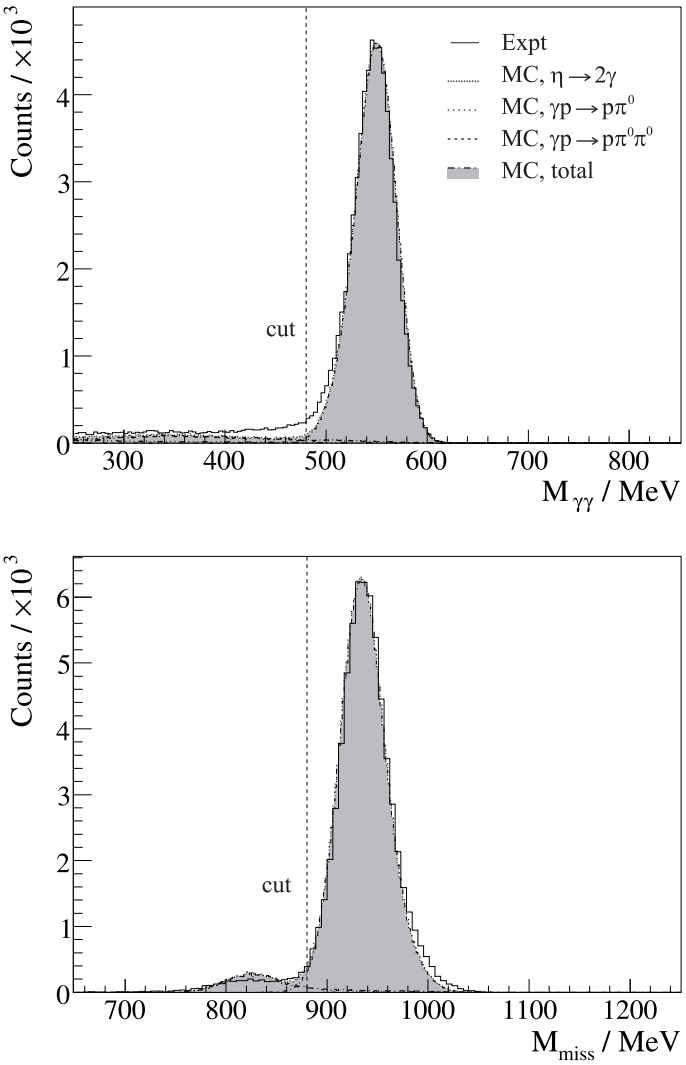

Figure 6.3: Top: two-photon invariant mass distribution for 707 MeV $< E_\gamma <$ 820 MeV after a cut on the missing mass. Bottom: two-photon missing mass distribution after a cut on the invariant mass. The shaded histograms were produced by the Monte Carlo simulation.

of the random tagger hits is shown in fig. 6.3 top as the solid histogram. The combinatorial background at smaller invariant masses arises mainly from π^0 production, for example, if two photons from different π^0 mesons are detected within the time resolution or if $\pi^0\pi^0$ events are produced with two escaping photons. The simulation of π^0 and $\pi^0\pi^0$ photoproduction showed that the contribution of the background to the η meson candidates was less than 1.5%. Simulated η events generated an invariant mass distribution in good agreement with the measured data. Though the agreement between simulated and measured background was not as good, the inconsistency was small above $M_{\gamma\gamma} \approx 480$ MeV. After subtraction of the background caused by the random coincidences between the Crystal Ball and the tagger microscope, the η yield below production threshold was very close zero.

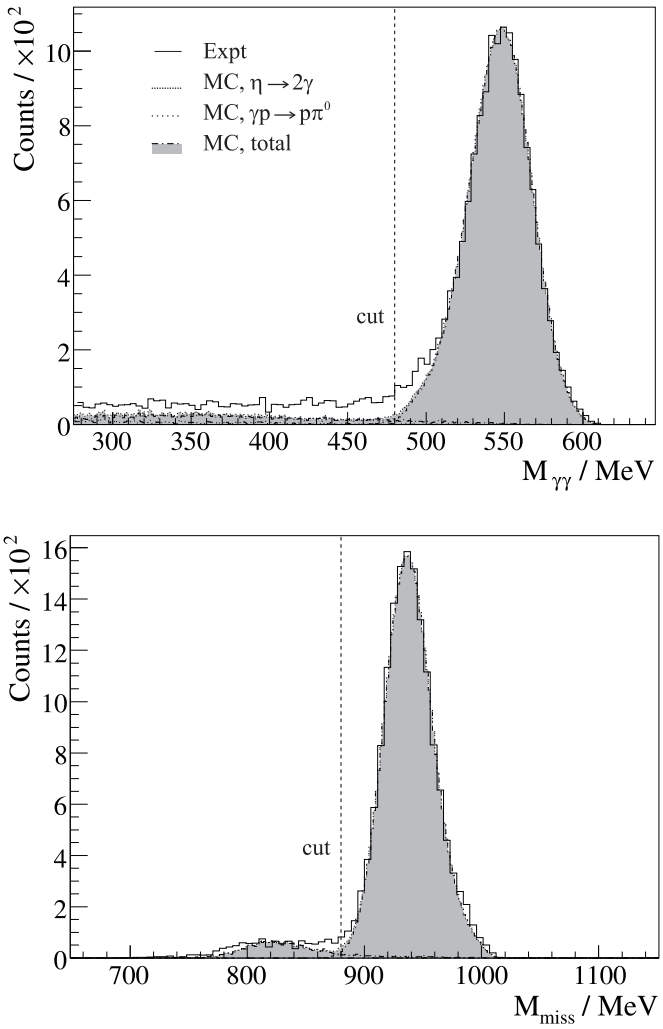

Figure 6.4: Top: two-photon invariant mass distribution for 707 MeV $< E_\gamma <$ 730 MeV after a cut on the missing mass. Bottom: two-photon missing mass distribution after a cut on the invariant mass. The shaded histograms were produced by the Monte Carlo simulation.

6.3.2 Decay channel $\eta \to 3\pi^0$

The identification of the $\eta \to 3\pi^0 \to 6\gamma$ decay concentrated on events with a trigger multiplicity M ≥ 3 and six clusters detected as photons, ignoring all other particles. Among the 15 possible combinations of six photons to be arranged in three pairs, the combination with the minimum χ^2-value:

$$\chi^2 = \frac{1}{3\sigma_{\gamma\gamma}^2} \sum_{i=1}^{3} (m_{\gamma\gamma}[i] - m_{\pi^0})^2 \tag{6.3}$$

was assumed to be correct. Here $m_{\gamma\gamma}[i]$ are the invariant masses of the photon pairs, $\sigma_{\gamma\gamma}$ is the width of the invariant mass distributions and m_{π^0} is the well-known π^0 mass. Figure 6.5 shows the distribution of the minimum χ^2 and distribution of the

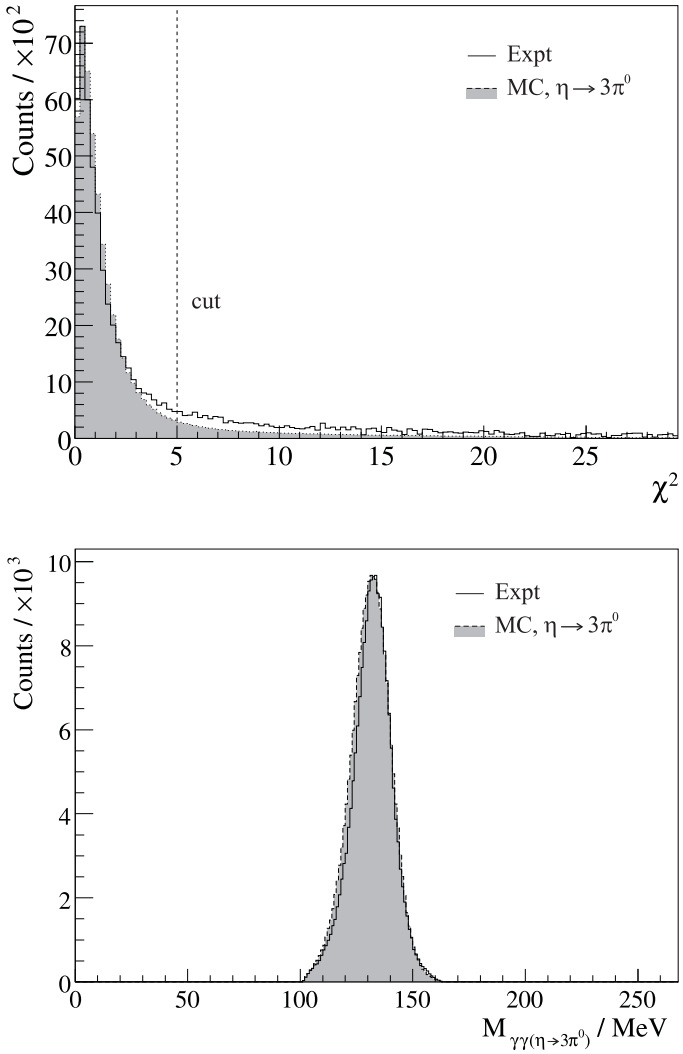

Figure 6.5: Top: distribution of the minimum χ^2 from 6γ-events for $707\,\mathrm{MeV} < E_\gamma < 820\,\mathrm{MeV}$. Bottom: invariant mass distribution of photon pairs from 6γ-events after applying a cut at $\chi^2 < 5$. The shaded histograms are from the Monte Carlo simulation of the $\eta \to 3\pi^0$ events.

invariant mass of the photon pairs after a cut at $\chi^2 < 5$ was applied. Simulation of this channel with the GEANT code showed that 12% of the simulated $\eta \to 3\pi^0$ events generated a χ^2 beyond this threshold. The invariant mass and missing mass distributions of the six photons, shown in fig. 6.6, were in quite good agreement with the simulation. Additional cuts on the invariant mass at $M_{6\gamma} > 460\,\mathrm{MeV}$ and on the missing mass $M_{\mathrm{miss}} < 1020\,\mathrm{MeV}$ were applied.

The main background contribution was caused by the resonant $3\pi^0$ production through the reaction $\gamma p \to 3\pi^0 p$. The simulation of this process gave a total reconstruction efficiency $\varepsilon_{3\pi^0} \approx 7\%$. Using the estimate of the total cross section made in [Jun05], $\sigma_{3\pi^0} \approx 0.4\,\mu\mathrm{b}$ for $E_\gamma < 1100\,\mathrm{MeV}$, the cross section $\sigma_{3\pi^0} \approx 0.15\,\mu\mathrm{b}$ in the E_γ

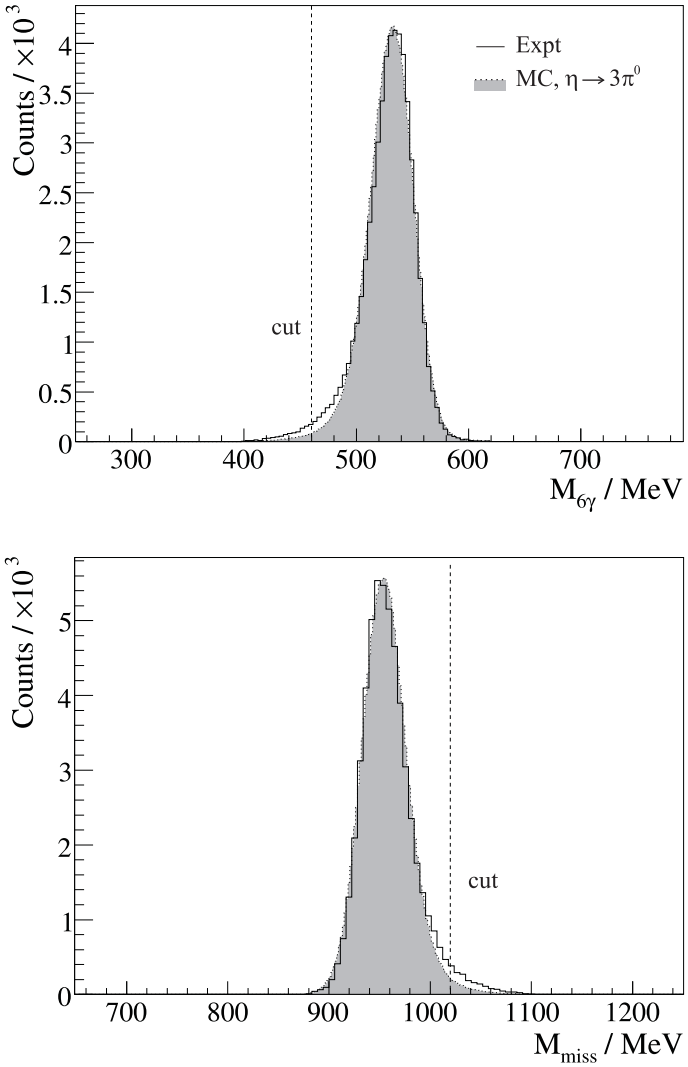

Figure 6.6: Top: six-photon invariant mass distribution for 707 MeV $< E_\gamma <$ 820 MeV after applying the $\chi^2 < 5$ cut of fig. 6.5. Bottom: six photon missing mass distribution. The shaded histograms are from the Monte Carlo simulation of the $\eta \to 3\pi^0$ events.

energy range 707 to 730 MeV was calculated, supposing a linear behavior starting from zero at the production threshold near $E_\gamma = 492$ MeV. Since the average cross section for the reaction $\gamma p \to p\eta$ in this region is $\sigma_\eta \approx 8\,\mu$b, the fraction of the $3\pi^0$ events can be calculated:

$$\frac{N_{3\pi^0}}{N_{\eta\to 3\pi^0}} = \frac{\sigma_{3\pi^0}}{\sigma_\eta \cdot \mathrm{BR}_{\eta\to 3\pi^0}} \cdot \frac{\varepsilon_{3\pi^0}}{\varepsilon_{\eta\to 3\pi^0}} \approx 2\%, \tag{6.4}$$

where $\varepsilon_{3\pi^0}$ and $\varepsilon_{\eta\to 3\pi^0}$ are the acceptances for the resonant $3\pi^0$ production and the $\eta \to 3\pi^0$ decay, respectively, and $\mathrm{BR}_{\eta\to 3\pi^0}$ is the branching ratio for the given decay. Since below the η production threshold ($E_\gamma < 707$ MeV) no other process can

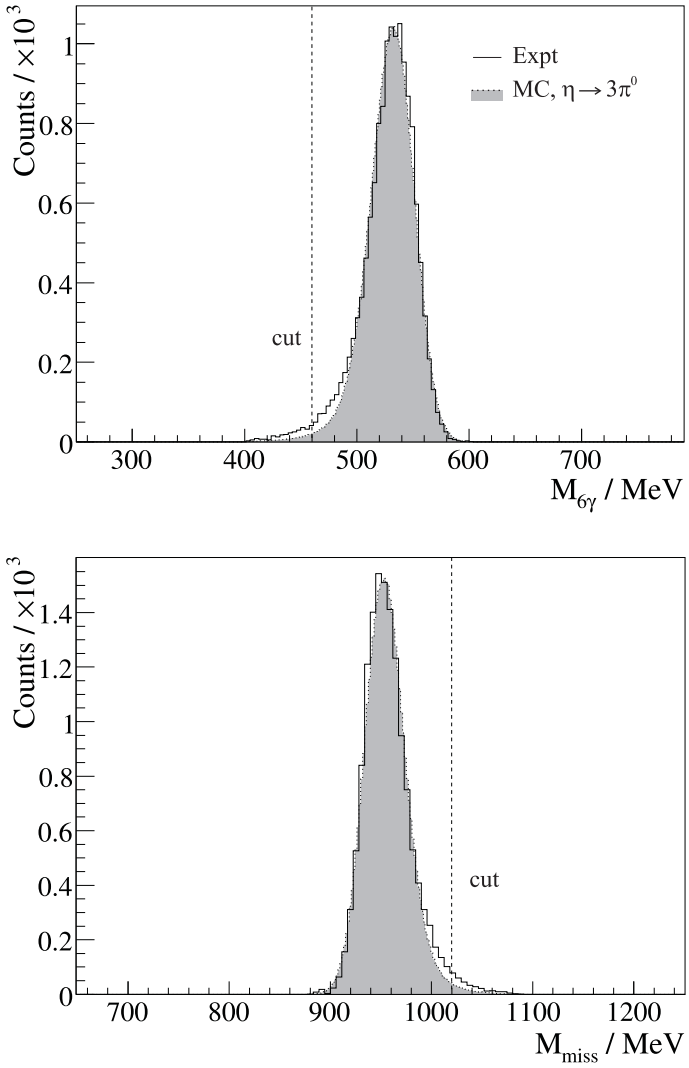

Figure 6.7: Top: six-photon invariant mass distribution for $707\,\mathrm{MeV} < E_\gamma < 730\,\mathrm{MeV}$ after applying the $\chi^2 < 5$ cut of fig. 6.5. Bottom: six photon missing mass distribution. The shaded histograms indicate the Monte Carlo simulation of the $\eta \to 3\pi^0$ events.

produce six or more photons, the contribution of the resonant $3\pi^0$ production can also be estimated by measuring the η cross section below threshold, which ideally must be zero. Such an estimate resulted in approximately $0.12\,\mu$b. Supposing that the considered process made the same contribution to the η cross section above the η threshold, one can determine the contribution of the $3\pi^0$ events to the η events of about 2% in the energy region $707\,\mathrm{MeV} < E_\gamma < 730\,\mathrm{MeV}$, in agreement with the estimate made with equation (6.4).

	η experiment	MDM experiment
Real time	81 h	96 h
Collimator	3 mm	4 mm
MAMI beam current	35 nA	12 nA
Tagged decays $\eta \to 2\gamma$	198,000	5,000
Tagged decays $\eta \to 3\pi^0$	159,000	76,000
Tagged decays $\eta \to 2\gamma$ (microscope)	46,000	1,400
Tagged decays $\eta \to 3\pi^0$ (microscope)	40,000	22,000

Table 6.1: Overview of the experimental statistics. The higher beam current in the η experiment produced more useful events. The last two rows show the events tagged with the tagger microscope in the energy range $707\,\mathrm{MeV} < E_\gamma < 730\,\mathrm{MeV}$.

6.4 Overview of the experimental statistics

Using the analysis steps described in this chapter, the candidate η events were selected. Table 6.1 summarizes the total number of registered η candidates in the two experiments dedicated to determination of the η meson mass. The number of events has been estimated by subtracting the number of events in the random time window of the tagger from prompt events. The last two rows in table 6.1 show the events tagged with the tagger microscope in the energy range $707\,\mathrm{MeV} < E_\gamma < 730\,\mathrm{MeV}$. The higher electron beam current during the η experiment produced more useful events than in the MDM experiment. Moreover, the multiplicity trigger $\mathrm{M} \geq 2$ in the MDM experiment was scaled by a factor of 49 in order to suppress detection of $\pi^0 \to 2\gamma$ events, which also markedly decreased the number of registered $\eta \to 2\gamma$ events. Thus, the $\eta \to 2\gamma$ events from the data of the MDM experiment were too few to be useful.

Chapter 7

Results and discussion

The last chapter of this work presents the final results of the data analysis described in the previous chapter. The analysis steps were applied not only to the experimental data, to pick out candidate events, but also to the simulated data in order to find the detector acceptance, which was necessary for determination of the total cross sections. In the following sections of this chapter, the total cross sections for the investigated reactions are presented. The cross section for the $\gamma p \to p\pi^0$ reaction is well known and was used to check different steps of the analysis and normalizations. The main focus of this work is the cross section for the $\gamma p \to p\eta$ reaction and measurement of the production threshold using the high resolution tagger microscope. Since a complete analysis of microscope data has never been undertaken so far, comparison was made with cross sections derived from the main focal-plane detector to verify that the microscope produced consistent results. Finally, the procedure for the measurement of the threshold energy is described, and the result for the mass of the η meson is presented and discussed.

7.1 Total cross sections

The normalizations of the total cross sections were obtained from the target thickness, the intensity of the photon flux, the simulated acceptance of the Crystal Ball/TAPS detector setup, and the branching ratios of the η decays. The candidate $\pi^0 \to 2\gamma$, $\eta \to 2\gamma$, and $\eta \to 3\pi^0$ events, reconstructed as described in chapter 6, were used to determine the total cross sections for the corresponding reactions. The total cross section $\sigma_{\mathrm{x}}(i)$ for a tagger channel i can be found using

$$\sigma_{\mathrm{x}}(i) = \frac{N_{\mathrm{x}}(i)}{N_{e^-}(i) \cdot \varepsilon_{\mathrm{tagg}}(i) \cdot N_p \cdot \varepsilon_{\mathrm{x}}(i) \cdot \mathrm{BR(x)}}\,, \tag{7.1}$$

where x represents one of the investigated reactions, $N_{\mathrm{x}}(i)$ is the number of reconstructed events, $N_{e^-}(i) \cdot \varepsilon_{\mathrm{tagg}}(i) = N_\gamma(i)$ is the photon flux, N_p is the target density, $\varepsilon_{\mathrm{x}}(i)$ is the acceptance of the detector setup, and BR(x) is the branching ratio of the corresponding decay into photons. The number of reconstructed events was

determined using the coincidence analysis and by subtracting the measurements made with an empty target normalized to the same livetime as the experimental data. The determination of the target density and the photon flux were already discussed in chapter 4. The target density was calculated from the target thickness, molar mass, and density of the liquid hydrogen. The photon flux was determined by counting electrons detected in the tagger, and measuring the ratio of the number of tagged photons, passing through the collimator, to the number of the tagger electrons (tagging efficiency).

In the simulation the decays of the η meson were implemented without taking into account the branching ratios. Thus, the branching ratios [Ams08]

$$\begin{cases} \mathrm{BR}\,(\eta \to 2\gamma) &= 39.31\% \\ \mathrm{BR}\,(\eta \to 3\pi^0) &= 32.56\% \end{cases} \tag{7.2}$$

had to be included in equation (7.1) when calculating the total η cross section. Decay of the π^0 meson into photons was handled by GEANT, which calculated this decay with the corresponding branching ratio. Thus, the simulated detector efficiency $\varepsilon_{\pi^0\to 2\gamma}(i)$ already contained the branching ratio of the π^0 meson, and it was therefore not explicitly included in equation (7.1).

The acceptance of the Crystal Ball/TAPS detector setup was determined for each decay channel by analysis of the events simulated with the GEANT code as described in chapter 5. Figure 7.1 shows the acceptance for π^0 production (top) and for η production using decay channel $\eta \to 3\pi^0$ (bottom) as a function of the incident photon energy. The acceptance for the MDM experiment is shown on the left and for the η experiment – on the right. As expected there is little difference for the $\eta \to 3\pi^0$ analyses, however, the π^0 and $\eta \to 2\gamma$ events were suppressed by the $\mathrm{M} \geq 2$ condition of the L2 trigger, which was scaled down by 49 in the MDM experiment and by 3 in the η experiment, thus, reducing the acceptance for these channels. The trigger divide factor was not usually included in the simulation; the acceptances $\varepsilon_{\pi^0\to 2\gamma}(i)$ and $\varepsilon_{\eta\to 2\gamma}(i)$ from the simulation were explicitly divided by this factor. The $\eta \to 2\gamma$ channel was ignored in the MDM experiment as the large scaling factor for the $\mathrm{M} \geq 2$ events resulted in too few events for a meaningful result.

The acceptances for η production in the η experiment are shown in fig. 7.2 for the two decays of the meson. For more consistency, and to cross check the analysis, the data have also been analyzed using Crystal Ball detector without TAPS (right). Figure 7.2 shows that the acceptance of the detector setup for the $\eta \to 2\gamma$ decay is almost unchanged when TAPS is excluded from the analysis. This is because only a few photons are emitted into the angle range covered by TAPS. The acceptance for decay $\eta \to 2\gamma$ was approximately 25% at the η production threshold smoothly decreasing to about 18% at $E_\gamma = 820\,\mathrm{MeV}$. On the other hand, the exclusion of TAPS noticeably influenced the acceptance for $\eta \to 3\pi^0$ decay. With TAPS included the acceptance was 38% at threshold smoothly decreasing to 22% at $E_\gamma = 820\,\mathrm{MeV}$. Without TAPS the acceptance was smaller, decreasing from 28% to 16% over the same tagged photon energy range.

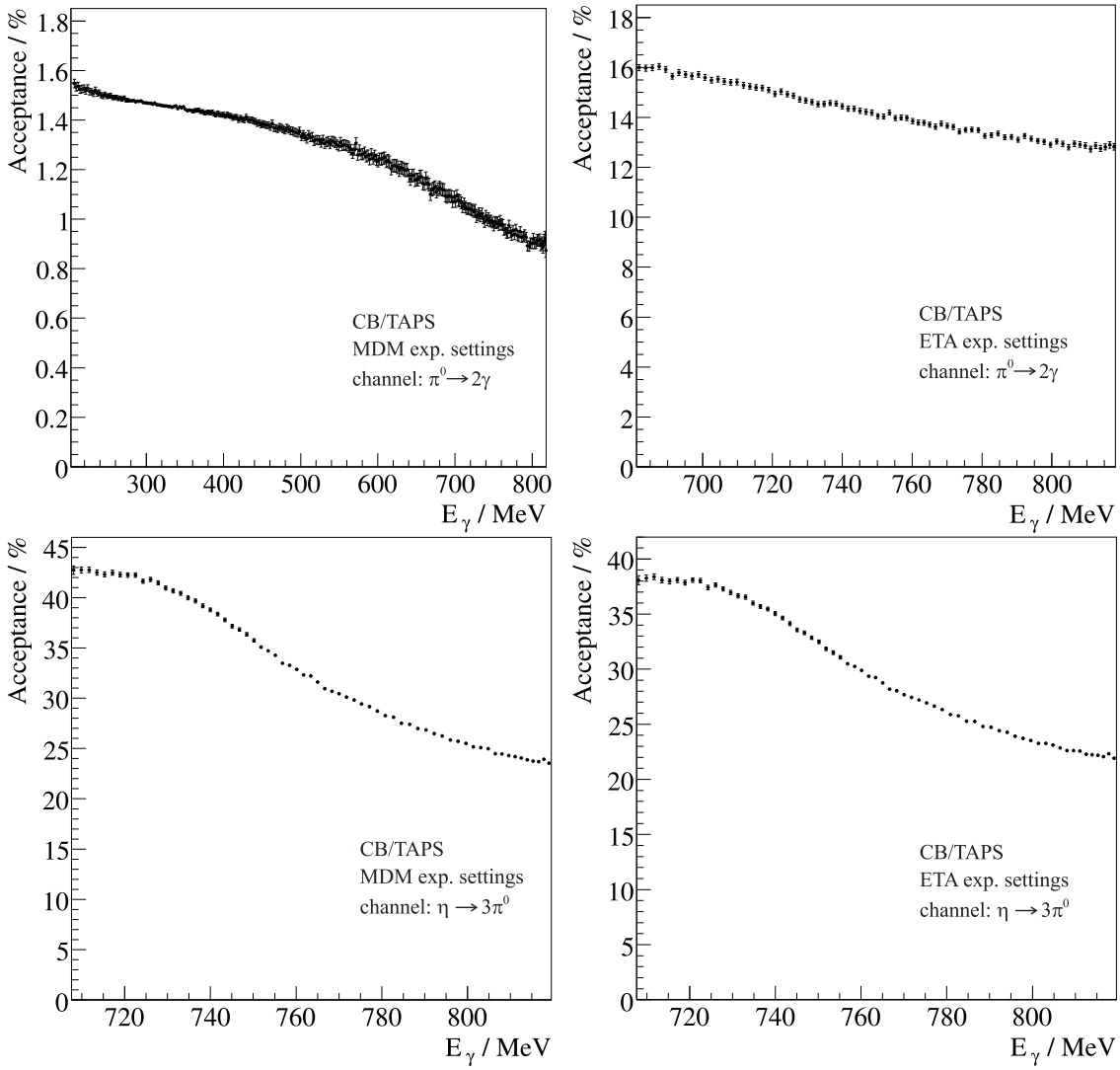

Figure 7.1: Top: acceptance of the Crystal Ball/TAPS detector setup for π^0 production obtained using the trigger condition of the MDM experiment (left) and the η experiment (right). Bottom: acceptance of the detector setup for η production obtained using $\eta \rightarrow 3\pi^0$ decay and the trigger condition of the MDM experiment (left) and the η experiment (right).

The systematic uncertainty of the cross sections, calculated with equation (7.1), is composed of the uncertainties of the target density (1.2%) and the detector acceptance (3%). In addition to the normalization factors explicitly presented in equation (7.1), one more correction was necessary for the cross sections obtained from the MDM experiment in order to reduce the effect caused by the problem in the tagger electronics (see fig. 4.20), which additionally introduced a systematic uncertainty estimated to be about 5%. Thus, the total systematic uncertainty was estimated to be about 6% for the cross sections obtained from the MDM experiment and about 3% for the cross sections from the η experiment.

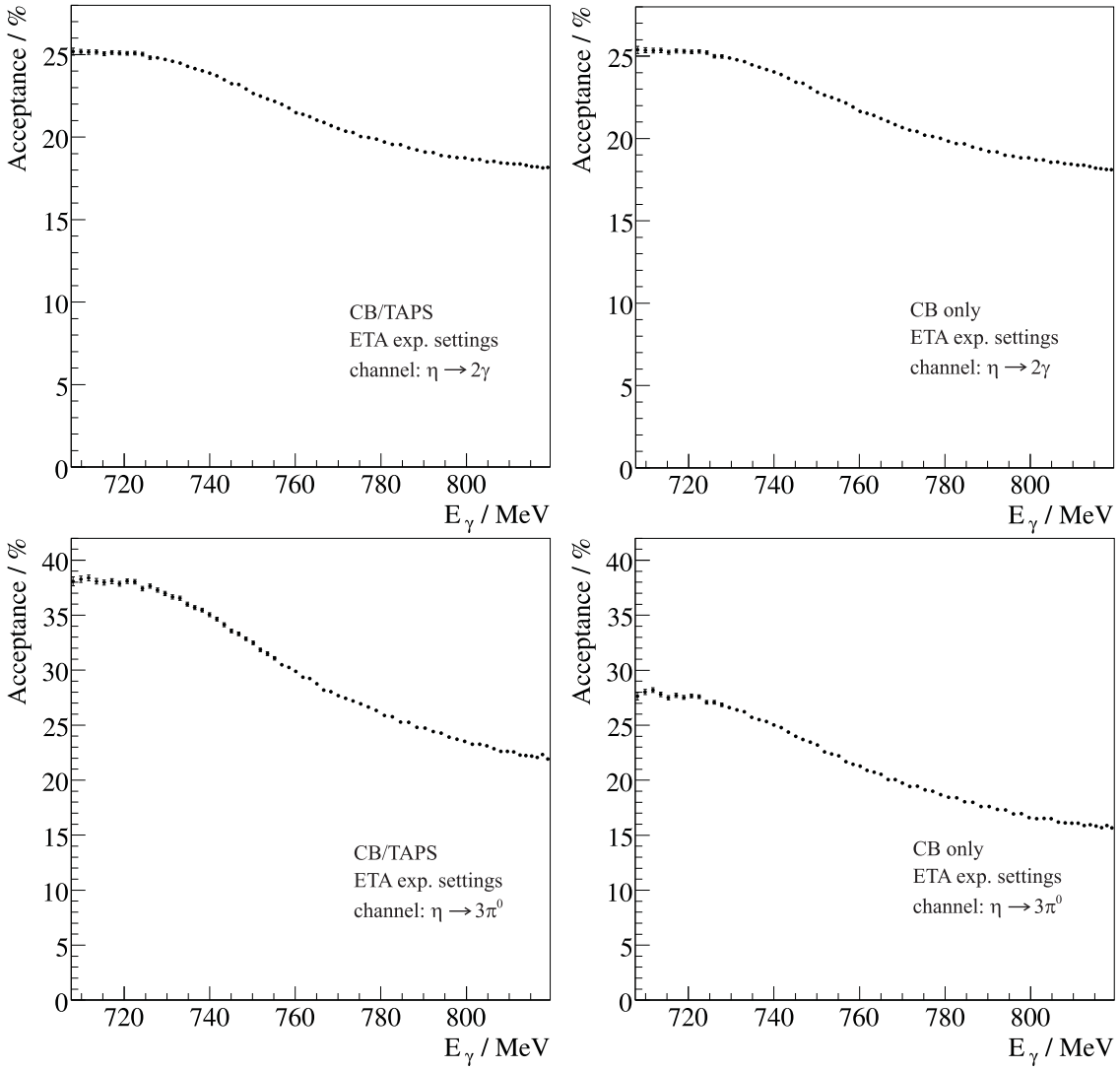

Figure 7.2: Acceptance of the detector setup for η production obtained using the trigger condition of the η experiment. Top: $\eta \to 2\gamma$ decay. Bottom: $\eta \to 3\pi^0$ decay. Left: Crystal Ball with TAPS. Right: Crystal Ball only.

The resulting total cross section for π^0 photoproduction from the MDM experiment is shown in fig. 7.3 in comparison with the MAID theoretical model taken from [Web02] and the earlier TAPS data [Leu01]. The plot results from about 250 hours of data collected in 07/2004. In the energy region up to $E_\gamma = 500\,\mathrm{MeV}$, the $P_{33}(1232)$ resonance is dominant. In this region the cross section has its maximum of about $290\,\mu\mathrm{b}$ at $E_\gamma \approx 320\,\mathrm{MeV}$. At energies higher than $E_\gamma \approx 650\,\mathrm{MeV}$ one can see the contribution of the second resonance region mainly due to the $S_{11}(1535)$, $P_{11}(1440)$ and $D_{13}(1520)$. At the maximum the present results are lower than the TAPS data by about 8%, though at lower energy they are above the MAID model and the TAPS data. Nevertheless, the difference between the present results and the TAPS data is comparable with the systematic uncertainty of both measurements.

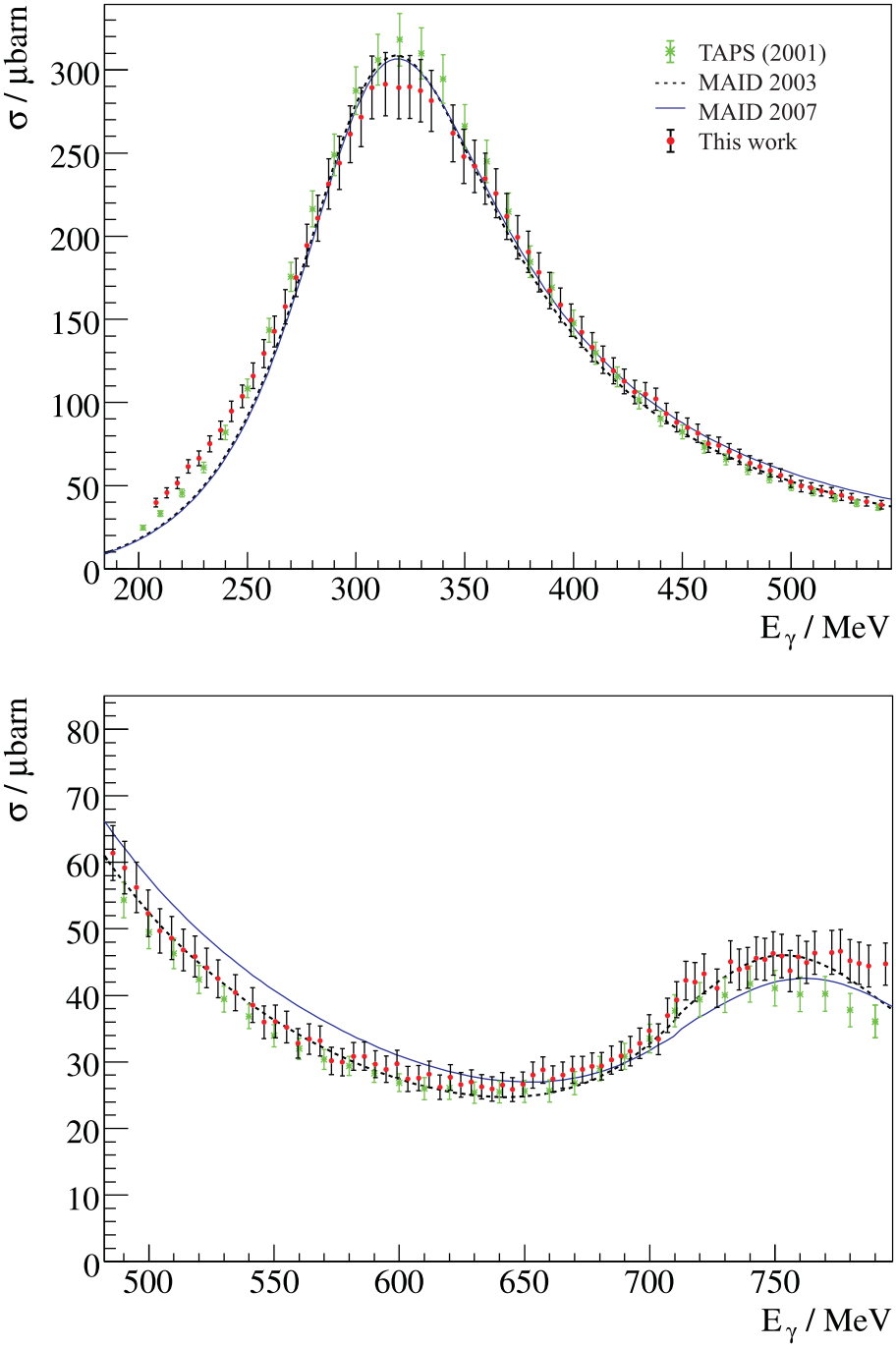

Figure 7.3: Total cross section for π^0 photoproduction obtained from the MDM experiment (07/2004) in comparison with the MAID theoretical model [Web02] and the earlier TAPS data [Leu01]. The error bars represent statistical (±1-3%) and systematic (±6%) uncertainties added in quadrature.

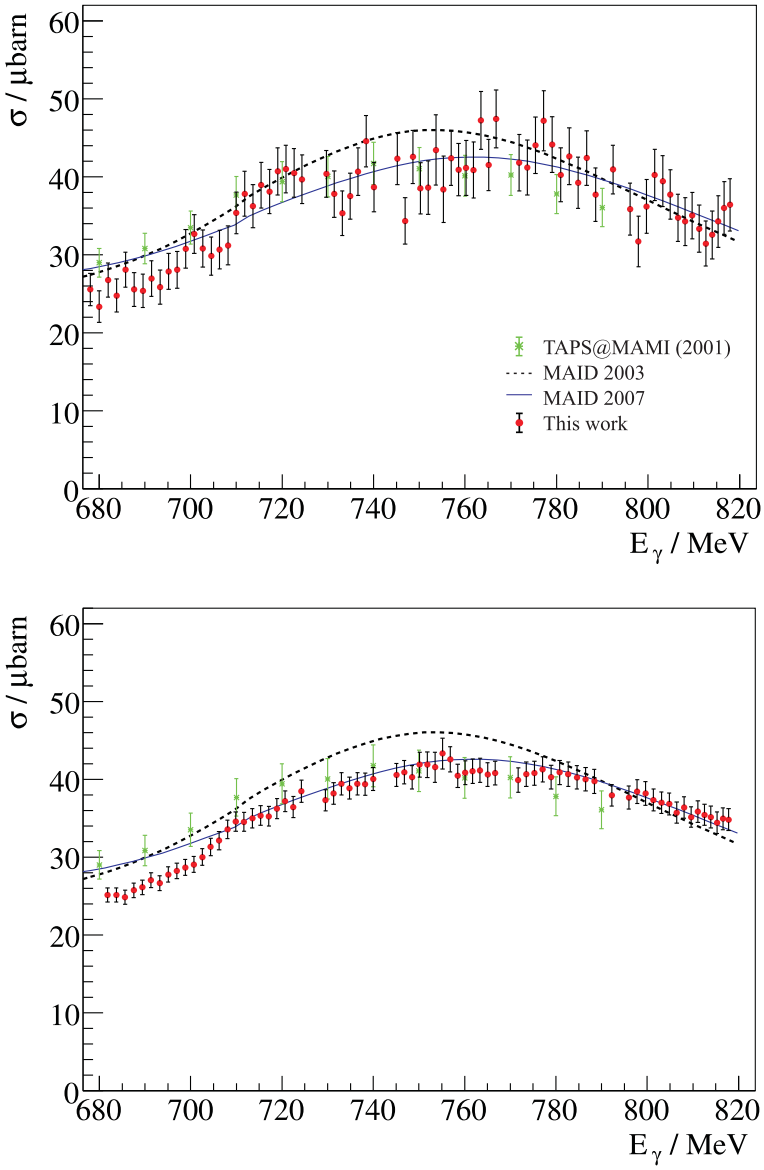

Figure 7.4: Total cross section for π^0 photoproduction obtained from the MDM (01/2005) experiment (top) and from the η experiment (bottom).

The small discrepancies are possibly due to uncertainty in some of the parameters used in the simulation.

In the second resonance region at $E_\gamma > 700\,\mathrm{MeV}$, which is important for the η threshold determination, the π^0 cross section is shown in fig. 7.4 in comparison with the MAID model [Web02] and the TAPS data [Leu01]. The figure shows that the cross sections, obtained from the MDM experiment (top) and from the η experiment (bottom), both agree quite well with the MAID 2007 model [Web02].

The cross section for η photoproduction is shown in fig. 7.5 in comparison with the earlier TAPS result [Kru95] and the theoretical prediction of the ETA-MAID model [Web03]. For the cross section, obtained from the data of the MDM experi-

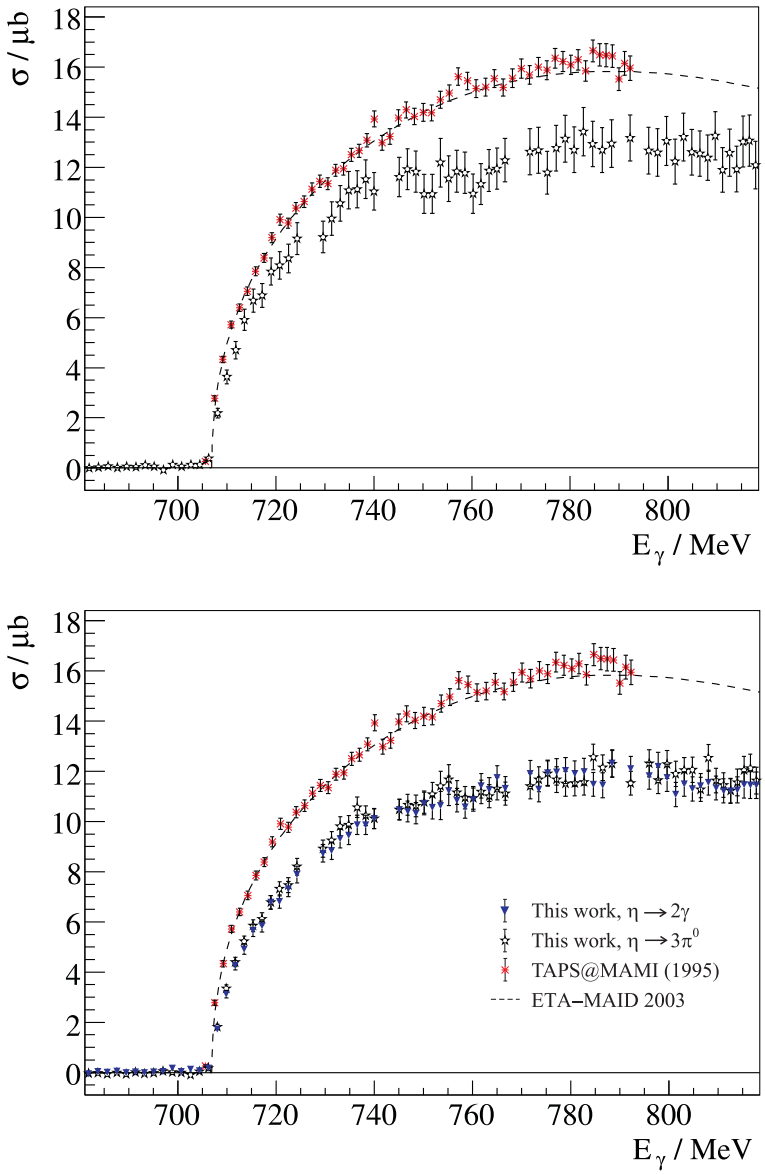

Figure 7.5: Total cross section for η photoproduction from the MDM (top) and η (bottom) experiments obtained using the main focal-plane detector in comparison with the ETA-MAID model [Web03] and TAPS data [Kru95].

ment shown in fig. 7.5 top, the correction for the fault in the electronics discussed in section 4.7.1 has been applied. The bottom picture shows the result of the η experiment. The error bars represent total uncertainty obtained by adding statistical and systematic uncertainties in quadrature. Unfortunately, for η photoproduction, it was not possible to obtain agreement with the earlier TAPS data [Kru95]. In fig. 7.5 one can see that the MDM experiment gave cross sections about 18% lower than the TAPS data, and the η experiment gave the values about 24% lower than the TAPS data over the whole energy region. Nevertheless, the cross sections, calculated from the $\eta \to 2\gamma$ events (triangles) and from the $\eta \to 3\pi^0$ events (stars), agreed good,

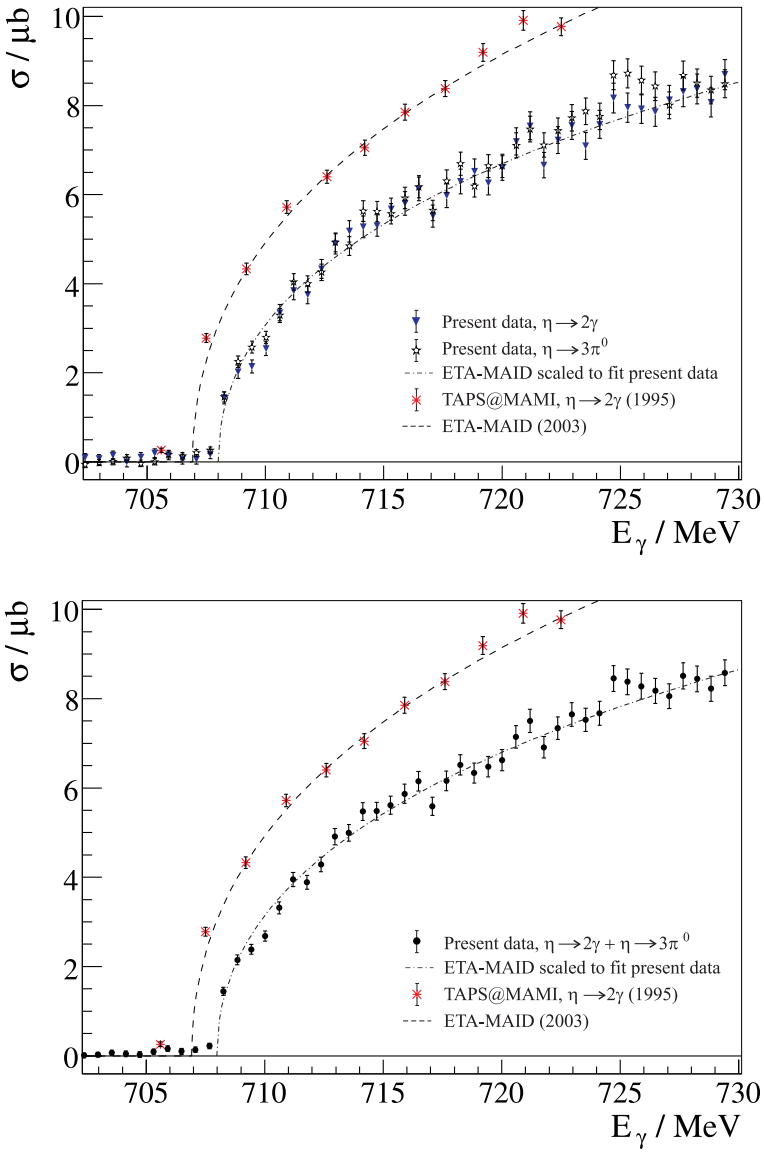

Figure 7.6: Total cross section for η photoproduction in 590 keV steps obtained using the strips of the high resolution tagger microscope. Top: cross sections obtained by separate analysis of data from the two η decay modes. Bottom: cross section obtained by summing all η events. The data are from the η experiment.

and also the difference between the cross sections from the MDM experiment and from the η experiment did not exceed the systematic uncertainty. The difference of about 7% between the η and MDM experiments can be explained by a feature of the tagger electronics (see also fig. 4.20). During the 2004/2005 round of experiments the tagger electronics allowed each TDC to register only the first hit within the 160 ns wide time window, and all further hits were lost. At low beam current this gave quite a small effect, but at higher beam current, like in the η experiment, more hits were registered within the 160 ns time window, and some of them got lost.

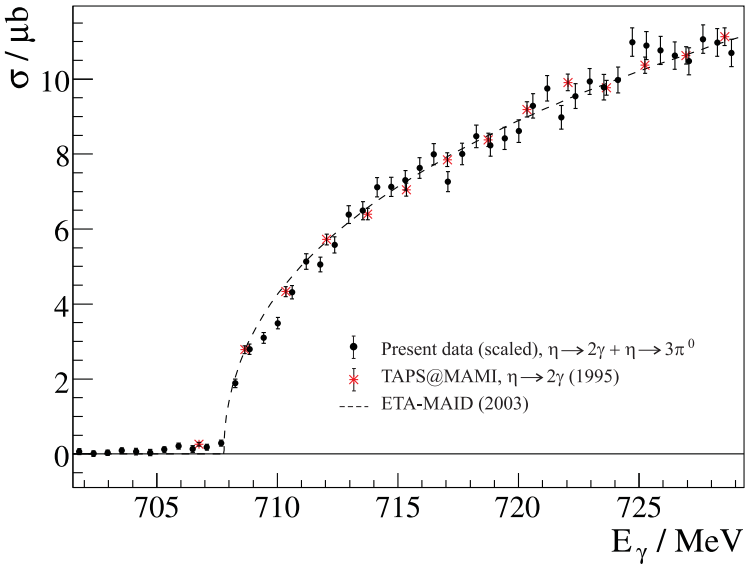

Figure 7.7: Total cross section for η photoproduction obtained using the strips of the high resolution tagger microscope scaled by factor 1.30. For visual comparison both the ETA-MAID model and the TAPS data were shifted to fit the threshold determined from the present data.

A calculation, made with 80 tagger channels and about 5 hits per event (in the η experiment), has shown that the effect leads to about 3-4% lost of the tagger hits in the η experiment in comparison to the MDM experiment.

In the analyses of the same data, described in references [Sch07] and [Unv08], some improvements of the geometry of the virtual detector setup, motivated by some discrepancies with the real one, have been suggested. One of the changes concerned the thickness of the bottom plates of the Crystal Ball hemispheres [Unv10]. The suggested larger value of this thickness decreased the detecting efficiency of the virtual detector setup by about 16% for the $\eta \to 3\pi^0$ events and by 5% for the $\eta \to 2\gamma$ events. The influence of the new thickness on the acceptance for π^0 events was less than 2%. The larger value of Crystal Ball plates thickness gave better agreement of the η cross section obtained from $\eta \to 3\pi^0$ events with the old TAPS data (see ref. [Unv08]), but it also introduced quite a large deviation between the cross sections obtained from $\eta \to 2\gamma$ and $\eta \to 3\pi^0$ events. After further discussion it was concluded that the old value of the bottom plates thickness should be correct, and it was decided to keep the old value. Thus, the discrepancy between the present and the old data remained unexplained.

In order to measure the η production threshold and determine the η mass, the high resolution tagger focal-plane microscope detector was used. As a first step, the total η production cross section was obtained using the microscope strips and is shown in fig. 7.6 for the photon energies up to 730 MeV in 590 keV steps. Though the background, caused by the target windows was measured with an empty target and subtracted, there is a small residual background ($\approx 0.12\,\mu$b) below threshold,

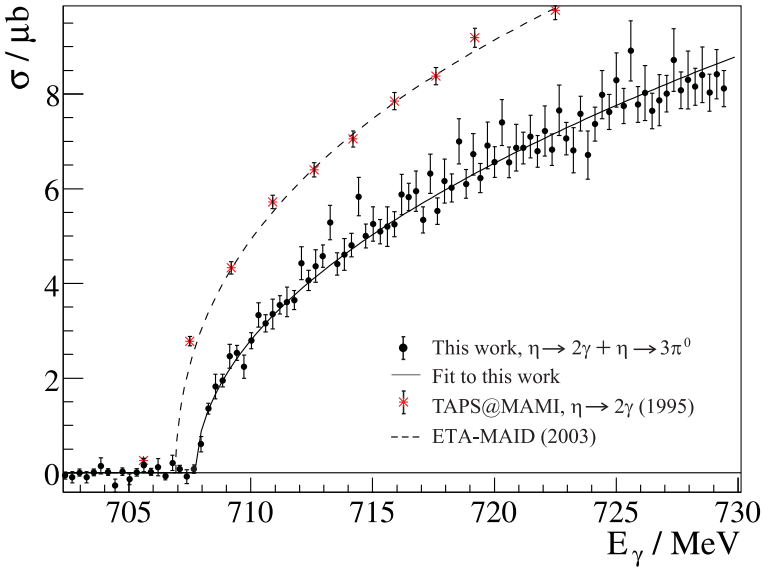

Figure 7.8: Total cross section for η photoproduction in 290 keV steps obtained using the channels of the high resolution tagger microscope. The cross section has been obtained by summing the η events from both decays. The solid line represents a fit to the result of this work. The data are from the η experiment.

caused by the background processes considered in chapter 6. The cross section was determined separately for the two considered decays of the η meson and by summing the events of both decays. For the latter the cross section was determined using

$$\sigma_\eta(i) = \frac{N_{\eta\to 2\gamma}(i) + N_{\eta\to 3\pi^0}(i)}{N_{e^-}(i)\cdot\varepsilon_{\mathrm{tagg}}(i)\cdot N_p\cdot(\varepsilon_{\eta\to 2\gamma}(i)\cdot \mathrm{BR}_{\eta\to 2\gamma} + \varepsilon_{\eta\to 3\pi^0}(i)\cdot \mathrm{BR}_{\eta\to 3\pi^0})}\,. \qquad (7.3)$$

In fig. 7.6 the result is compared to the old TAPS data [Kru95] and the prediction of the ETA-MAID model. Note that the ETA-MAID curve implies a production threshold corresponding to η mass $m_\eta = 547.300\,\mathrm{MeV}$ and is mainly dominated by the TAPS data. The results obtained using the $\eta \to 2\gamma$ and $\eta \to 3\pi^0$ events agree and show a similar deviation from the TAPS data as the cross sections obtained with the main tagger focal-plane detector (see fig. 7.5).

The discrepancy between the present η cross section and the previous data is probably due to a fault in the tagger electronics or in the simulation, but has not been fully explained within the scope of this work. However, in the energy range up to 730 MeV the data differed by an almost constant factor. Figure 7.7 shows the cross section obtained by summing all η events scaled by factor 1.30 in comparison with the ETA-MAID model and the TAPS data which both imply different η thresholds and, therefore, were shifted to fit the threshold determined from the present data. Correcting for a problem in the tagger electronics or in the simulated acceptance should influence the absolute value of the measured η cross section by an almost constant factor, but is very unlikely to significantly affect the result for the η threshold.

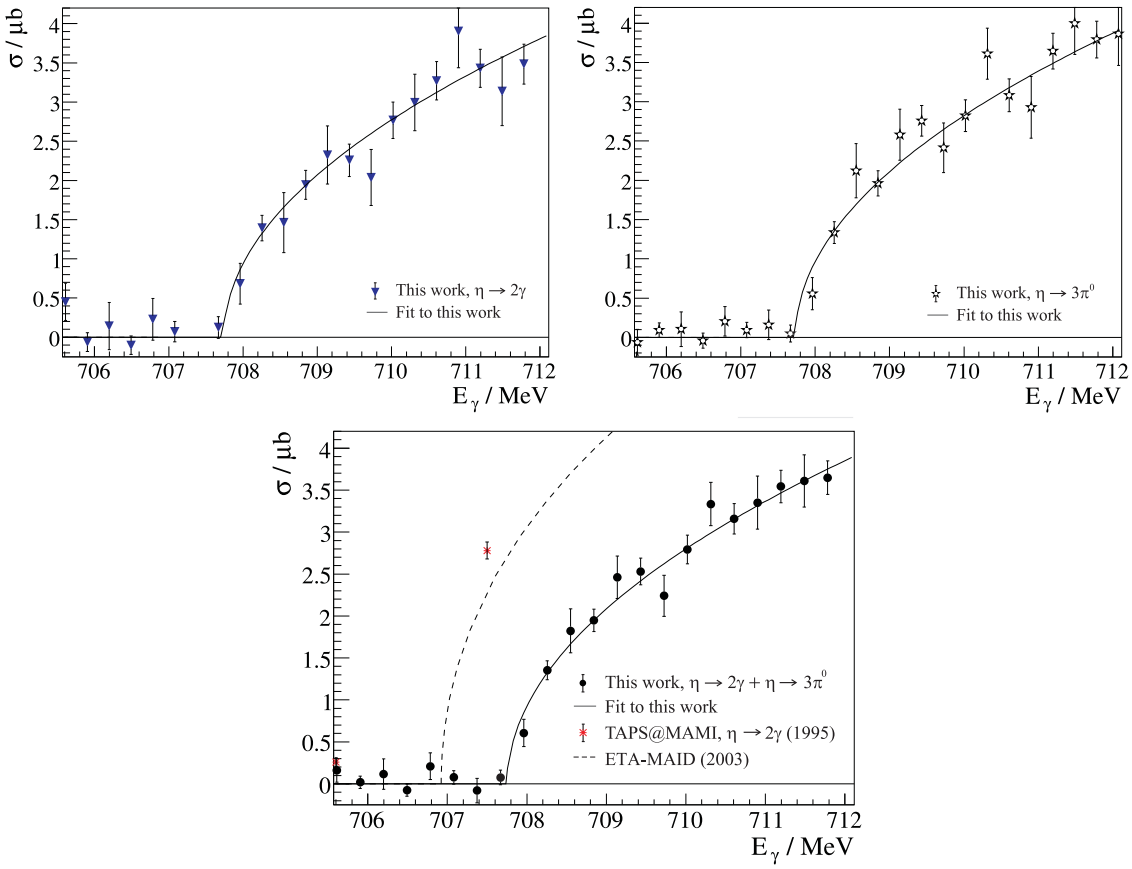

Figure 7.9: Total η cross section near production threshold. The solid line represents the fit for determination of the threshold energy.

7.2 Threshold energy and the η mass

In the previous section it was shown that though the result for the cross section did not agree with the other data, it was possible to describe the difference by a constant factor. For the measurement of the production threshold it is necessary to precisely determine the energy bin in which the η yield starts to grow. Therefore, the difference in the absolute value of the cross section should not hinder the measurement of the production threshold. The center of the first energy bin with non-zero η yield corresponds to η mass 547.965 MeV. The next bin with lower energy can be considered as consistent with zero and corresponds to η mass 547.780 MeV. Since the threshold must be between these bins, one can make a rough estimate of the η mass as the average of the two bins: $m_\eta = (547.873 \pm 0.094 \pm 0.062_{\text{syst.}})$ MeV, where the first uncertainty is the bin half-width, and the second systematic one originates from the uncertainty in the photon beam energy calibration discussed in section 4.5.8.

For precise measurement of the production threshold and the η mass, it was necessary to determine the behavior of the cross section near threshold. Due to strong dominance of the $S_{11}(1535)$ resonance in the threshold region, it is expected

for the total cross section

$$\sigma(E_\gamma) \propto (E_\gamma - E_{\rm thr})^{1/2}. \tag{7.4}$$

The cross section should vary with E_γ in the same way as the S_{11} partial width, which must vary near threshold as the η momentum q in the center-of-mass frame[1]. The momentum q is a function of $x = (E_\gamma - E_{\rm thr})$, and if expanded for small x, the leading order behavior is an $x^{1/2}$ term, and the next one is an $x^{3/2}$ term. Since $(E_\gamma - E_{\rm thr})$ is small near threshold, it was sufficient to use the first term of the expansion and neglect the rest. The function

$$f(E_\gamma) = a_1 \, (E_\gamma - E_{\rm thr})^{1/2}, \tag{7.5}$$

gave quite good agreement with the shape of the cross section near threshold and was used to fit the total η cross section σ_η.

The total cross section σ_η obtained with the full resolution of the tagger microscope is shown in fig. 7.8 in 290 keV steps. In order to simplify the fitting procedure, the residual background below the production threshold was linearly fitted and subtracted. Figure 7.9 shows the cross section near production threshold. To improve the statistical uncertainty, it was decided to fit the cross section obtained by summing the reconstructed events of both η decays. One can see in fig. 7.9 that each second bin has larger statistical uncertainty, which is because of the different widths of the single- and double-hit channels (see section 3.3). Single-hit channels were wider and collected more counts resulting in less statistical uncertainty. The square of the cross section, σ_η^2, which should depend linearly on the photon energy, is shown in fig. 7.10 top.

Due to the finite size of the energy bins, the number of counts in the center of the bin is proportional to the average value of the cross section over the width of the bin, so that its content will not be zero even if the bin only slightly overlaps the threshold. Therefore, the center of the first bin with non-zero counts can be below the threshold, which makes difficulties for the fitting procedure. One possibility to take this into account and make the fitting procedure more reliable is not to use this bin in the fit. Another possibility, which was suggested in [Kru95], is to fit the integral of the cross section. The experimental value of the integrated cross section is given by

$$S(n) = \sum_{i=n_0}^{n} \sigma_\eta(i) \cdot \Delta(i), \tag{7.6}$$

where $\sigma_\eta(i)$ is the cross section in the energy bin i, and $\Delta(i)$ is the width of the bin. The sum starts at n_0, which is the first bin with non-zero counts. Note that if $\sigma_\eta(i)$ gives the average value of the cross section over the width of the bin with energy $E_\gamma(i)$, then the value of $S(i)$ will give the integrated cross section at the upper edge

[1]This is an analytic property that can be shown by solving the Schrödinger equation for a short-range potential.

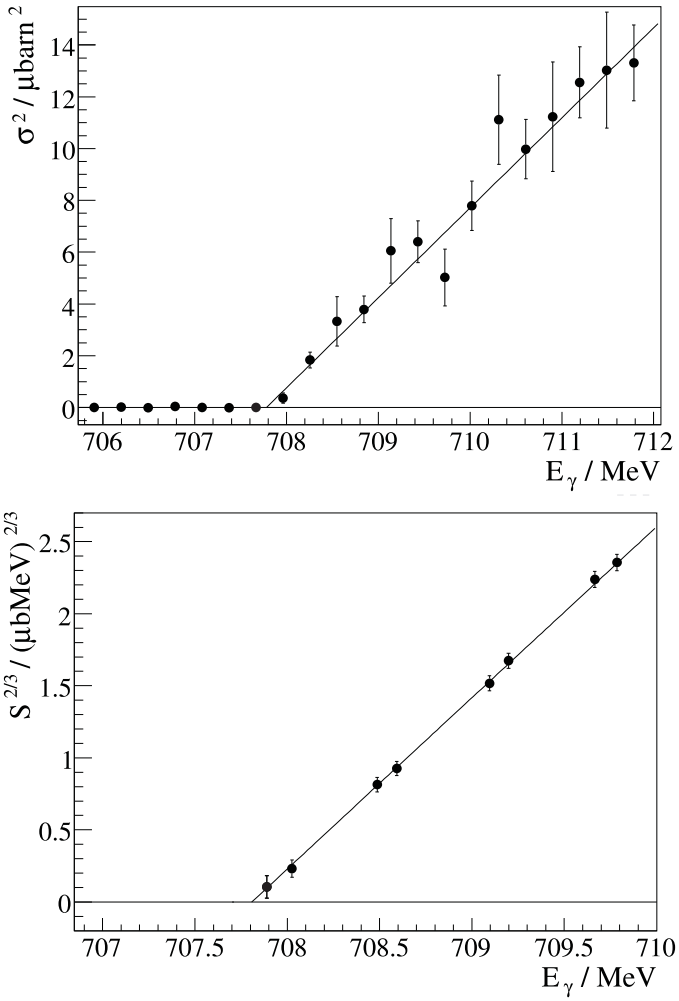

Figure 7.10: The square of the total η cross section σ_η^2 (top) and the integrated cross section $S^{2/3}$ (bottom) near production threshold. Solid lines represent fits for determination of the threshold energy.

of the bin, which corresponds to the photon energy $E_\gamma(i) + \Delta(i)/2$. Due to s-wave like energy behavior of the cross section it is expected:

$$S(i) \propto (E_\gamma(i) + \frac{\Delta(i)}{2} - E_{\rm thr})^{3/2}, \tag{7.7}$$

and, therefore, $S^{2/3}$ should be a linear function of the photon energy E_γ. The result for $S^{2/3}$ is shown in fig. 7.10 bottom. The behavior of the data close to threshold showed negligible deviation from linear.

The fit to $S^{2/3}$ data allows very precise determination of the threshold energy. However, one should take into account that the value of the cross section $\sigma_\eta(n_0)$ in the n_0 bin influences the $S^{2/3}$ values for all higher energy points and shifts the intersection of the fit line with the energy axis. The residual background mentioned above is particularly important for $\sigma_\eta(n_0)$. It was determined by fitting 60 points below threshold with maximum statistical uncertainty about $\pm 0.15\,\mu$b which suggests a

	m_η [MeV], fit σ_η	m_η [MeV], fit σ_η^2	m_η [MeV], fit $S^{2/3}$
$\eta \to 2\gamma + \eta \to 3\pi^0$	547.834 ± 0.035	547.851 ± 0.028	547.869 ± 0.031
$\eta \to 2\gamma$	547.826 ± 0.051	547.837 ± 0.046	547.824 ± 0.048
$\eta \to 3\pi^0$	547.822 ± 0.044	547.853 ± 0.033	547.860 ± 0.038
$\eta \to 3\pi^0$ (MDM exp.)	547.843 ± 0.058	547.849 ± 0.055	547.861 ± 0.056

Table 7.1: Comparison of the results for the η mass obtained by fitting the total cross section σ_η, σ_η^2, and the integral $S^{2/3}$ up to $E_\gamma = 730\,\text{MeV}$. The uncertainties are statistical only.

contribution of about $\pm 0.03\,\mu$b to the uncertainty in $\sigma_\eta(n_0)$. After subtraction of this background, the value of the cross section in the n_0 bin was $\sigma_\eta(n_0) = (0.10 \pm 0.08)\,\mu$b. The $\pm 0.08\,\mu$b uncertainty contributes an additional $\pm 9\,$keV to the statistical uncertainty of the η mass that results from the fit. Similarly the next bin $(n_0 + 1)$ added $\pm 15\,$keV, bin $(n_0 + 2)$ added $\pm 9\,$keV, $(n_0 + 3)$ added $\pm 13\,$keV, and so on. The influence of bin $(n_0 + 12)$ was less than 1 keV, and the influence of all higher energy bins could be neglected. In total, the additional statistical uncertainty was estimated to be $\pm 27\,$keV and was independent from the uncertainty of the fit of about $\pm 10\,$keV.

The threshold energy has been obtained by fitting the cross section σ_η, the square of the cross section σ_η^2, and the integral $S^{2/3}$. The cross section σ_η was fitted with function (7.5). Since σ_η^2 should depend linearly on E_γ near threshold, it was fitted with a piecewise linear function:

$$f(E_\gamma) = \begin{cases} 0, & \text{if } E_\gamma < E_{\text{thr}} \\ a_1\,(E_\gamma - E_{\text{thr}}), & \text{if } E_\gamma \geq E_{\text{thr}} \end{cases} \tag{7.8}$$

with the threshold energy E_{thr} and slope a_1. The integral of the cross section $S^{2/3}$ showed almost linear behavior close to threshold, but at higher energies a small quadratic term appeared [Kru95], and, therefore, the $S^{2/3}$ data has been fitted with a second order polynomial:

$$f(E_\gamma) = a_0 + a_1\,E_\gamma + a_2\,E_\gamma^2. \tag{7.9}$$

The intersection of the fit line (7.9) with zero delivered the result for the threshold energy E_{thr}. All mentioned fits, shown in figures 7.9 and 7.10, delivered consistent values for the threshold energy, which was converted to η mass using equation (1.1)

$$m_\eta = -m_p + \sqrt{m_p^2 + 2\,m_p\,\frac{E_\gamma^{\text{thr}}}{c^2}}, \tag{7.10}$$

repeated here for convenience. The results for the η mass are summarized in table 7.1. The values, derived separately from the $\eta \to 2\gamma$ and $\eta \to 3\pi^0$ events, also agreed well within the statistical uncertainties. Analysis of the additional experimental data of the MDM experiment also led to a consistent result for the η meson mass. Figure

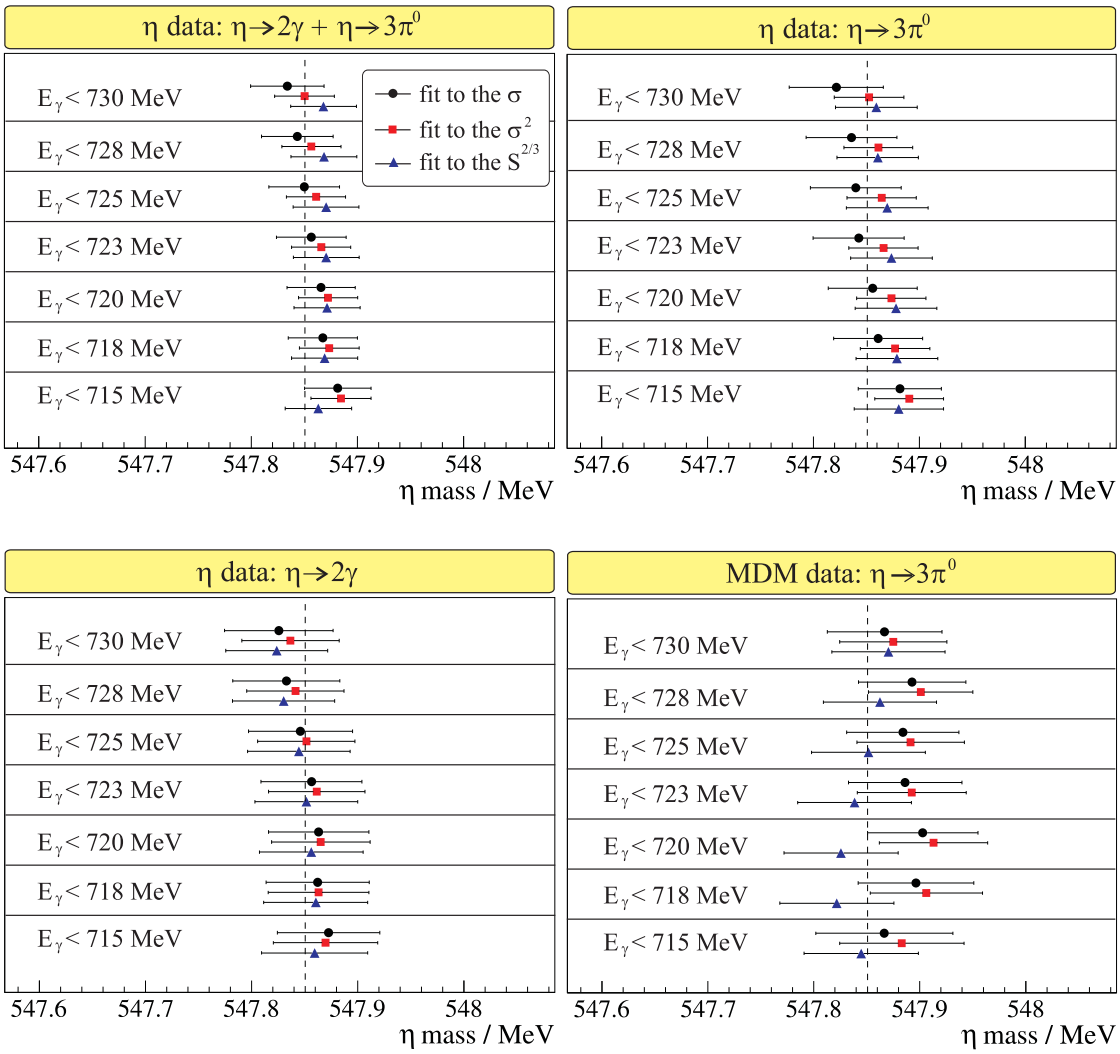

Figure 7.11: The η mass obtained using different methods to fit the threshold energy plotted versus the fit range. The dashed line indicates the result of this work.

7.11 shows the η mass obtained by fitting σ_η, σ_η^2, and $S^{2/3}$, plotted versus the upper limit of the fit range, showing good agreement with the η mass found by fitting over the full E_γ range up to 730 MeV.

The average of the three values listed in the first row of table 7.1 resulted in a threshold energy $E_{\text{thr}} = (707.794 \pm 0.049)$ MeV and corresponding η mass

$$m_\eta = (547.851 \pm 0.031_{\,\text{stat.}} \pm 0.062_{\,\text{syst.}})\,\text{MeV}, \tag{7.11}$$

where the first uncertainty is due only to statistics, and the second originates from the uncertainty in the photon beam energy calibration discussed in section 4.5.8. The result (7.11) supports the three very precise measurements by the NA48 [Lai02], KLOE [Amb07], and CLEO [Mil07] collaborations and disagrees by about 5σ with the smaller value obtained by the GEM [Abd05] collaboration. The η mass determined in this work is plotted in fig. 7.12 with the other measurements in the order of

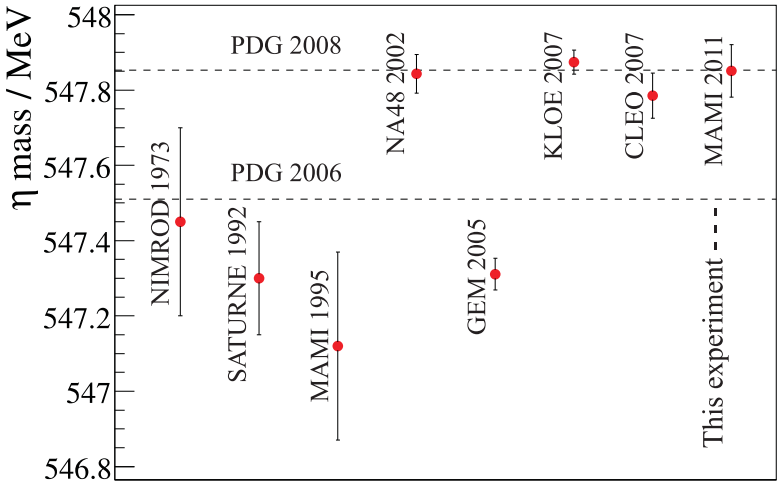

Figure 7.12: Overview of previous η mass measurements in comparison to the world average reported by the Particle Data Group [Yao06, Ams08] in 2006 and 2008 and the result of this analysis.

the year of publication. The disagreement with the previous measurement [Kru95] at MAMI may be due to the poorer photon energy resolution ($\Delta E_\gamma \approx 1.8\,\mathrm{MeV}$) of the main focal-plane detector and the lack of on-line beam monitors that resulted in a larger systematic uncertainty for the photon tagger energy calibration.

Chapter 8

Conclusion

This work describes the determination of the η mass by measuring the threshold of the $\gamma p \to p\eta$ reaction. This experiment was performed using the Crystal Ball/TAPS detector setup at the MAMI-B facility in Mainz and the recently developed tagger focal-plane microscope detector, which was used for the first time to obtain the total cross sections. The real photons were produced by Bremsstrahlung of the 883 MeV electron beam from MAMI-B on a thin diamond radiator. The absolute electron energy of the incident beam was precisely determined in the 3rd race-track microtron of MAMI-B, and the tagged photon energies were determined using the Glasgow photon tagging spectrometer (tagger). The microscope focal-plane detector was placed in front of the main focal-plane detector array and improved the tagged photon energy resolution, covering the energy region around the η production threshold ($E_{\mathrm{thr}} = 707\,\mathrm{MeV}$) from $E_\gamma = 674\,\mathrm{MeV}$ to $E_\gamma = 730\,\mathrm{MeV}$ at an electron beam energy $E_0 = 883\,\mathrm{MeV}$. The microscope provided 191 tagging channels with an energy resolution of about 290 keV per channel compared to approximately 2 MeV available from the main focal-plane detector.

Special care was taken of the energy calibration of the tagger microscope with electrons of different known energies from MAMI. The calibration of the tagger microscope was performed by varying the magnetic field B_{cal} in the tagging spectrometer around the value B_{exp} used in the experiment. This was done with three different MAMI energies to scan across the tagger microscope by increasing the value of B_{cal} in small steps and plotting the measured hit position of the beam in the microscope versus the equivalent energy. The fit was performed by a least squares minimization with the aid of the MINUIT package, supposing a linear dependence between tagging electron energy and microscope channel number.

The η mesons were selected by identifying the decay products of the two most prominent neutral decays, $\eta \to 2\gamma$ and $\eta \to 3\pi^0$, in the Crystal Ball/TAPS detector setup. The three precise η mass measurements by the NA48, KLOE, and CLEO collaborations were confirmed, though the result presented in this work disagrees with the GEM collaboration measurement. The uncertainty for the new η mass measurement has been improved in comparison to the previous Mainz experiment by

a factor of about 3. Poorer resolution and an underestimated systematic uncertainty of the tagger energy calibration in the old measurement may be responsible for the disagreement with the present result.

Appendix A

Accurate absolute tagger energy calibration for the main focal-plane detector

The main tagger focal plane detector was also directly calibrated in the region overlapping with the microscope. The procedures of the calibration were designed by our colleagues at the University of Glasgow [Rei04] and repeated by the author. For the main tagger focal-plane detector the calibration program TAGCAL 6.0 was available, which took the NMR value as a parameter and calculated the corresponding electron energy for each tagger channel. As result of the absolute tagger energy calibration a correcting offset to the TAGCAL prediction was found. Because of much larger (in comparison to the microscope) channel width (about 13 mm along

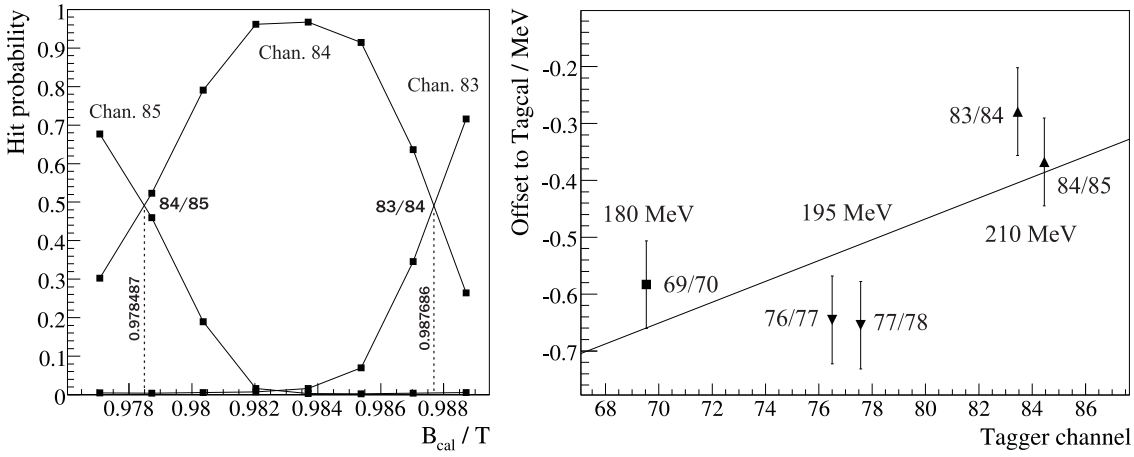

Figure A.1: Left: scan through tagger channels 83-85 with a 195 MeV electron beam. Right: linear fit to 5 points representing the energy difference between the measured MAMI energy and the prediction of the tagger calibration program TAGCAL 6.0 for 5 channel overlaps near the tagger magnetic field $B_{\mathrm{exp}} = 1.049\,\mathrm{T}$.

Overlap	E_0, MeV	B_{cal}, T	E_{equiv}, MeV	E_{tagcal}, MeV	Offset, keV
69/70	180.10	1.044963	180.802	181.386	-584
76/77	195.13	1.056130	193.859	194.505	-646
77/78	195.13	1.045930	195.750	196.405	-655
83/84	210.18	1.061792	207.655	207.935	-280
84/85	210.18	1.052388	209.511	209.879	-368

Table A.1: Measured NMR values for 5 measurements of the tagger channel overlaps. Measured energies E_{equiv} were always lower compared to the values E_{tagcal}, predicted by the TAGCAL 6.0 calibration program. The last column shows the difference between measured and predicted values ($E_{\mathrm{equiv}} - E_{\mathrm{tagcal}}$). The magnetic field $B_{\mathrm{exp}} = 1.04904\,\mathrm{T}$ was assumed (average over January 2005).

the focal plane) the narrow overlap between two adjacent channels was used to obtain accurate hit positions during the calibration scans with the MAMI beam. In order to find the NMR value, corresponding to the overlap of two channels, the field was changed in small steps around the field $B_{\mathrm{exp}} = 1.049\,\mathrm{T}$ until the main beam had at least been moved from one tagger channel to the next.

For each measured field value the tagger TDC hit pattern was normalized to unit area (divided by the total number of counts in the histogram), so that the spectrum represented the probability, that a certain channel was hit for a given NMR value. A typical plot for those probabilities as a function of the magnetic field is shown in fig. A.1 (left) for the 3 tagger channels 83-85 and beam energy 195.13 MeV. The NMR values of the intersection points were well defined and as expected were located at about 50% probability (fig. A.1 left).

The measured NMR values at the overlap positions (and hence corresponding equivalent electron energies) are compared with the TAGCAL prediction in table A.1. As one can see, the measured values were always smaller than predicted. The differences between measured and predicted values are shown in fig. A.1 (right) for 5 overlaps at the magnetic field close to B_{exp}. The error bars represent the $\pm 140\,\mathrm{keV}$ uncertainty of the MAMI beam energy. Lacking any better information the measured energy offsets were fitted with a straight line determined with the origin moved to the barycenter. The result of the fit allowed correction of the energies predicted by TAGCAL for the tagger channels 69-85:

$$\Delta(ch) = a + b \cdot (ch - 78.30), \tag{A.1}$$

$$a = -(499 \pm 53)\ \mathrm{keV},\ b = (18.3 \pm 9.2)\ \mathrm{keV/ch}.$$

This gave a $-710\,\mathrm{keV}$ correction to the TAGCAL prediction at the overlap between channels (numbering begins at 1 for the highest tagged photon energy) 66/67 (near η threshold) or $+450\,\mathrm{keV}$ in the η mass scale.

Appendix B

Stability of the experimental parameters

The tagger magnetic field and the MAMI beam position at the radiator affect the tagger energy calibration. Both were regularly read during the experiment and saved to the database.

B.1 Tagger magnetic field

To produce the tagger electron energy calibration map, the dipole magnetic field value must be specified. The magnetic field was monitored during the experiment with the NMR probe, located in the uniform region of the tagger dipole. In fig. B.1 the NMR information extracted from the database for the December 2004 period is shown. The average value of $B_{\mathrm{exp}} = 1.04943\,\mathrm{T}$ was obtained.

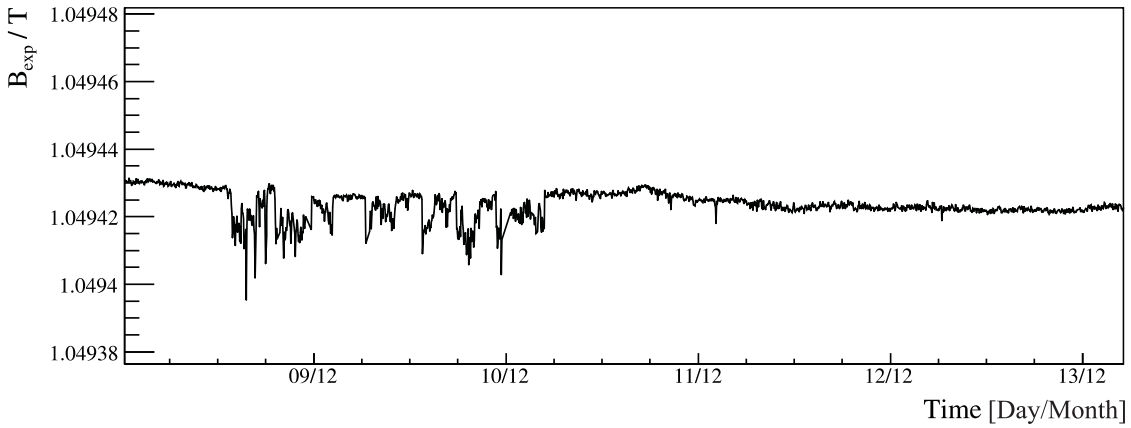

Figure B.1: Behavior of the tagger dipole magnetic field B_{exp}. The data are based on the NMR information.

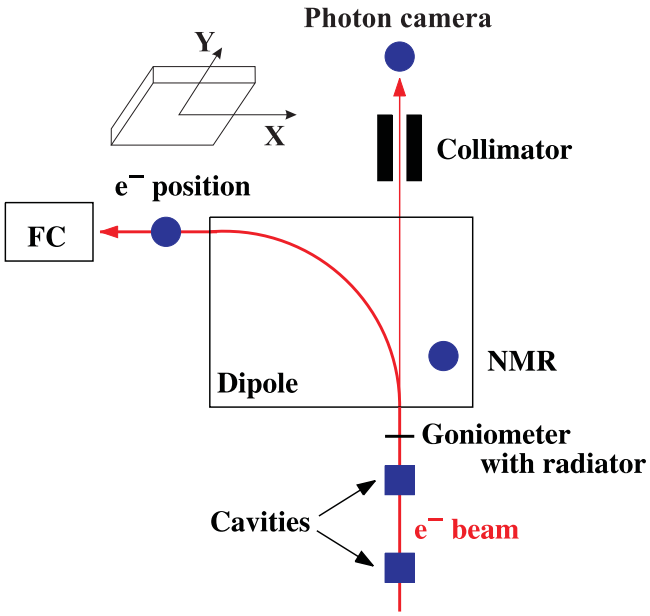

Figure B.2: Schematic view of the beam position monitoring. The beam position is defined in the coordinate system, in which the positive x axis points right and the positive y axis points upward.

B.2 Electron beam position at radiator

The electron beam position monitoring is schematically drawn in fig. B.2. The beam position at the radiator is of main importance, since a shift at this place can influence the hit position at the tagger focal plane. The beam position at the radiator was precisely monitored with 4 position sensitive cavities. As the beam goes through the cavity it incites high frequency beats in it. If the beam is centered in the cavity, no signal is delivered. If the beam is not centered, a signal proportional to the offset of the beam from the center is generated. The beam position is monitored with these cavities in two places before the beam hits the radiator (see fig. B.2 and B.3). The information obtained with the cavities is shown in fig. B.4. The cavities 1 and 2 are responsible for the x position, cavities 3 and 4 – for the y position. During the experiment maximum shifts of 0.35 mm in cavity 1 and 0.3 mm in cavity

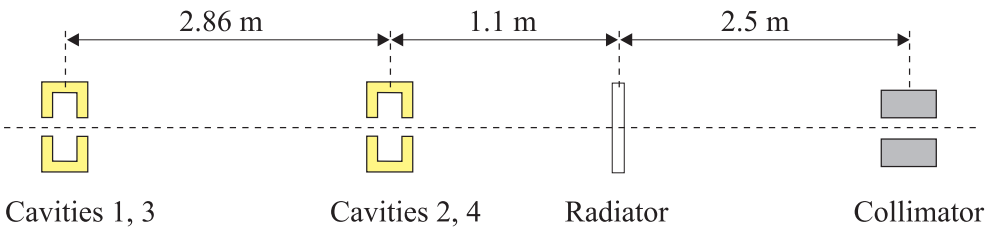

Figure B.3: Distances between the position sensitive cavities, the radiator, and the collimator.

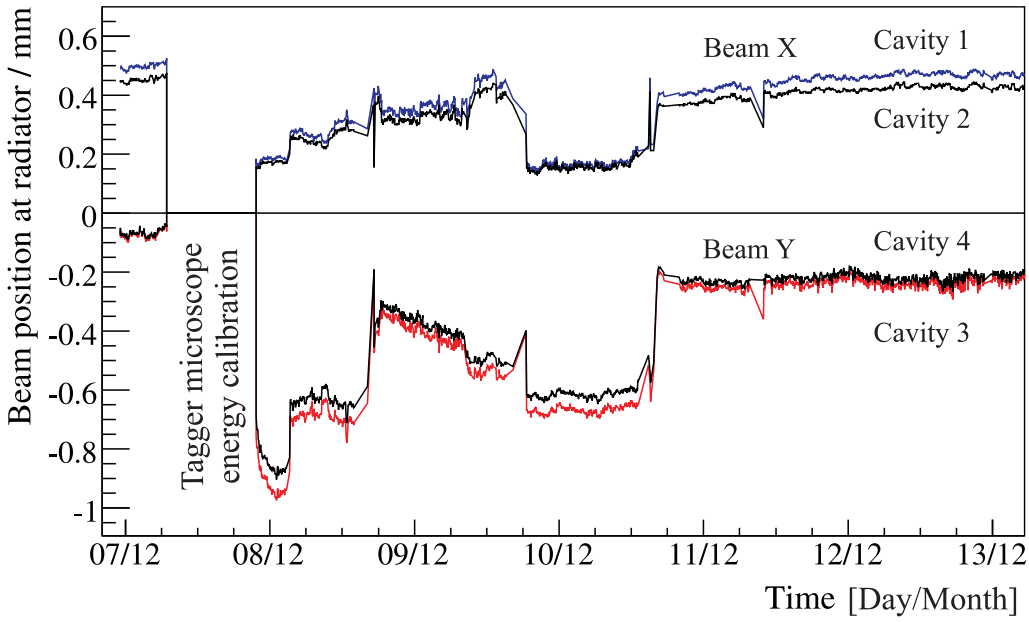

Figure B.4: The electron beam position measured with position sensitive cavities. Cavities 1 and 2 are responsible for the x position, cavities 3 and 4 for the y position.

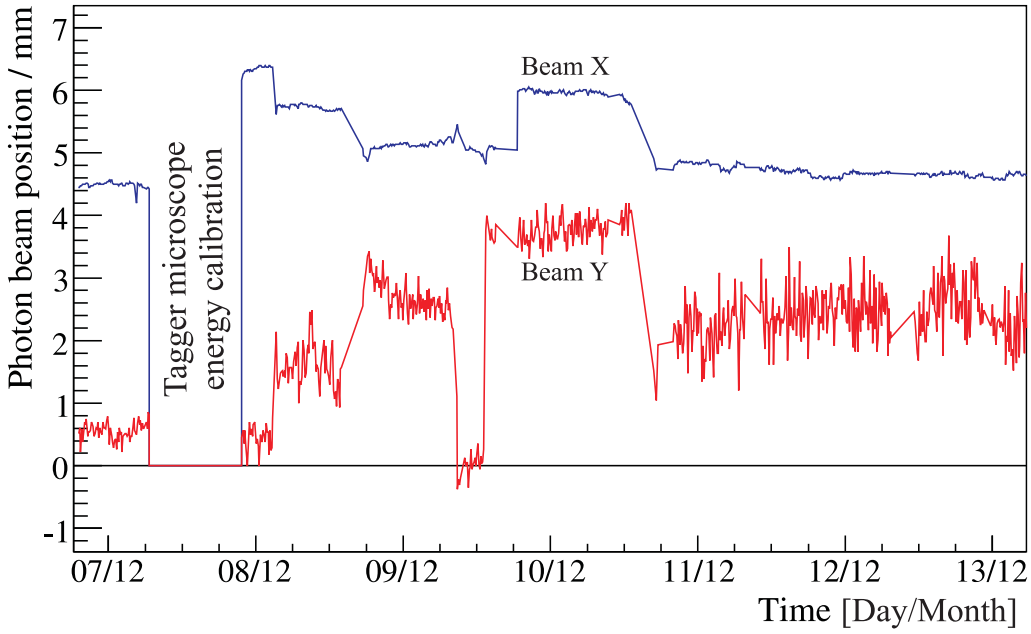

Figure B.5: The photon beam position determined with the photon beam camera. The deflection of the photon beam is opposite to the deflection of the electron beam in the cavities. This is due to the collimation at the tagger exit.

2 were observed. Taking into account the distances between the cavities and the radiator illustrated in fig. B.3, one obtains a maximum shift of about 0.3 mm at the radiator. The corresponding shift in the position, where the beam hits the focal plane in the region of the microscope, is 60% (perpendicular to the electron trajectory) of the shift at the radiator (an estimate from a ray-tracing simulation by I. Anthony [Mcg06]), which should be divided by $\sin(\theta)$, where θ is the angle the electron trajectory makes with the focal plane ($\theta = 40^\circ$ at tagger channel 66 [Mcg06], near η threshold). Therefore, the maximum shift in the tagging electron energy can be estimated to be

$$\frac{290\,\mathrm{keV/ch}}{2\,\mathrm{mm/ch}} \cdot 0.3\,\mathrm{mm} \cdot \frac{60\%}{\sin(40^\circ)} = 40\,\mathrm{keV}, \tag{B.1}$$

where 290 keV/ch is the microscope resolution, and 2 mm/ch is the channel width. This value corresponds to a ± 20 keV uncertainty. Due to very low beam intensity during the tagger energy calibration, the online monitoring using the cavities was impossible, thus, no correction for the beam position could be applied.

The electron beam camera in the tagger beam dump was not calibrated, and the data from it was not useful (the beam position was measured in pixels).

B.3 Photon beam position

The photon beam position was monitored in the photon camera near the photon beam dump. Figure B.5 shows opposite beam deflection with response to the position in the cavities. This is due to the collimation at the tagger exit. Thus, the relative beam deflections at the radiator and in the photon camera are proportional to the distances from the radiator to the collimator (~ 2.5 m) and from the collimator to the photon camera (~ 25 m).

B.4 Alignment of the electron beam at radiator

It was common practice to use the photon camera to fine tune the beam alignment. The radiator to collimator distance is about 2.5 m, and the radiator to photon camera distance is about 25 m. The 3 mm diameter collimator produces a spot of about 30 mm diameter at the photon camera. It could be noticed if the spot was misaligned by 1/10 of the diameter, *i. e.* ± 3 mm at the photon camera or ± 0.3 mm at the radiator. The same calculation as in equation B.1 converts this value to about ± 40 keV in tagging electron energies.

Bibliography

[Abd05] M. Abdel-Bary *et al.* (GEM Collaboration), Phys. Lett. **B 619** (2005) 281.

[Ahr00] J. Ahrens *et al.* (GDH and A2 Collaborations), Phys. Rev. Lett. **84** (2000) 5950.

[Amb07] F. Ambrosino *et al.* (KLOE Collaboration), JHEP **0712** (Oct 2007) 073.

[Ams08] C. Amsler *et al.* (Particle Data Group), Phys. Lett. **B 667** (2008) 1.

[Ani05] A. V. Anisovich, A. Sarantsev, O. Bartholomy, E. Klempt, V. A. Nikonov, and U. Thoma, Eur. Phys. J. **A 25** (2005) 427.

[Ann05] J. R. M. Annand, *Data Analysis within an AcquRoot Framework*, Internal Report, University of Glasgow, Scotland (2005).

[Ant91] I. Anthony *et al.*, Nucl. Instrum. Meth. **A 301** (1991) 230.

[Bar89] R. J. Barlow, *Statistics – a guide to the use of statistical methods in physical sciences*, Wiley & Sons (1989).

[Bas62] P. L. Bastien *et al.*, Phys. Rev. Lett. **8** (1962) 114117.

[Ben95] M. Benmerrouche, N. C. Mukhopadhyay, and J. F. Zhang, Phys. Rev. **D 51** (1995) 3237.

[Bjo64] J. D. Bjorken and S. D. Drell, *Relativistic Quantum Mechanics*, McGraw-Hill, New York (1964).

[Boi08] B. Boillat, *Magnetic moment of the $\Delta(1232)$ resonance*, Ph. D. Thesis, University of Basel, Switzerland (2008).

[Bor02] B. Borasoy, E. Marco, S. Wetzel, Phys. Rev. **C 66** (2002) 055208.

[Bru07] J. Brudvik, *Measurement of the branching ratio for eta-meson decay into a neutral pion and two photons*, Ph. D. Thesis, University of California Los Angeles, USA (2007).

[Chi97] W.-T. Chiang and F. Tabakin, Phys. Rev. **C 55** (1997) 2054.

[Chi02] W.-T. Chiang, S. N. Yang, L. Tiator, and D. Drechsel, Nucl. Phys. **A 700** (2002) 429.

[Chi03] W.-T. Chiang, S. N. Yang, L. Tiator, M. Vanderhaeghen, and D. Drechsel, Phys. Rev. **C 68** (2003) 045202.

[Cla97] M. Clajus, *Recent changes to the Crystal Ball simulation code*, Crystal Ball note CB-97-004, Department of Physics and Astronomy, University of California Los Angeles, USA (1997).

[Cod05] R. Codling, *Measurement of the magnetic dipole moment of the $\Delta^+(1232)$ resonance via the $p(\vec{\gamma}, \gamma'\pi^+ n)$ reaction*, Ph. D. Second Year Report, Department of Physics & Astronomy, University of Glasgow, Scotland (2005).

[Cre05] V. Crede, O. Bartholomy *et. al.*, Phys. Rev. Lett. **94** (2005) 012004.

[Don92] J. F. Donoghue, E. Golowich, B. R. Holstein, *Dynamics of the Standard Model*, Press Syndicate of the University of Cambridge, Cambridge, United Kingdom (1992) 36.

[Dow07] E. Downie, *Radiative π^0 photoproduction in the region of the $\Delta(1232)$ resonance*, Ph. D. Thesis, Department of Physics & Astronomy, University of Glasgow, Scotland (2007).

[Dör96] Th. Dörk, *Entwurf und Erprobung einer Anordnung zur kontinuierlichen und hochauflösenden Messung der Endenergie des Mainzer Mikrotrons MAMI*, Diplomarbeit, Institut für Kernphysik, Johannes Gutenberg-Universität Mainz (1996).

[Dre99] D. Drechsel, S. S. Kamalov, L. Tiator, Nucl. Phys. **A 645** (1999) 145-174.

[Dre03] P. Drexler *et al.*, IEEE Trans. Nucl. Sci. **50** (2003) 969.

[Dua74] A. Duane *et al.*, Phys. Rev. Lett. **32** (1974) 425.

[Eid04] S. Eidelman *et al.* (Particle Data Group), Phys. Lett. **B 592** (2004) 1.

[Gol64] M. Goldberg, M. Gundzik, S. Lichtman, J. Leitner, M. Primer *et al.*, Phys. Rev. Lett. **12** (1964) 546550.

[Gro00] D. E. Groom *et al.* (Particle Data Group), Eur. Phys. J. **C 15** (2000) 1.

[Hal96] S. J. Hall *et al.*, Nucl. Instrum. Meth. **A 368** (1996) 698.

[Her76] H. Herminghaus *et al.*, Nucl. Inst. Meth. A **138** (1976) 1.

[Her92] K. Herter, *Entwicklung und Erprobung eines Verfahrens zur Messung der absoluten Energie des Elektronenstrahls von MAMI*, Diplomarbeit, Institut für Kernphysik, Johannes Gutenberg-Universität Mainz (1992).

[Jan06] A. Jankowiak, Eur. Phys. J. **A 28** (2006) 149.

[Jan06a] A. Jankowiak, *Compilation of: Measurement of the electron beam energy at the Mainz Microtron*, MAMI Internal Report 03/2006, Institut für Kernphysik, Johannes Gutenberg-Universität Mainz (2006).

[Jan08] A. Jankowiak, private communication (2008).

[Jun05] J. Junkersfeld, Ph. D. Thesis, *Photoproduktion von $\pi^0\omega$ am Proton bei Energien bis zu 3 GeV*, Rheinische Friedrich-Wilhelms-Universität Bonn (2005).

[Kai87] K.-H. Kaiser, *PTRACE – Ein Programm auf der Basis von RAYTRACE zur Simulation der Elektronenbahn im Mikrotron*, Institut für Kernphysik, Johannes Gutenberg-Universität Mainz (1987).

[Kal64] G. R. Kalbfleisch *et al.*, Phys. Rev. Lett. **12** (1964) 527530.

[Knö95] G. Knöchlein, D. Drechsel, and L. Tiator, Z. Phys. **A 352** (1995) 327.

[Kot01] M. Kotulla, *Experiment zur Bestimmung des magnetischen Moments der $\Delta^+(1232)$ Resonanz*, Dissertation, II. Physikalisches Institut, Justus-Liebig-Universität Giessen (2001).

[Kra07] D. Krambrich, *Aufbau des Crystal Ball Detektorsystems und Untersuchung der Helizitätsasymmetrie in $\gamma p \to p\pi^0\pi^0$*, Dissertation, Institut für Kernphysik, Johannes Gutenberg-Universität Mainz (2007).

[Kru95] B. Krusche *et al.*, Z. Phys. **A 351** (1995) 237.

[Lai02] A. Lai *et al.* (NA48 Collaboration), Phys. Lett. **B 533** (2002) 196.

[Leu01] R. Leukel, *Photoproduktion neutraler Pionen am Proton mit linear polarisierten Photonen im Bereich der $\Delta(1232)$-Resonanz*, Dissertation, Institut für Kernphysik, Johannes Gutenberg-Universität Mainz (2001).

[Lug07] S. Lugert, *In-Medium modification of pion-pairs on deuterium* Ph. D. Thesis, II. Physikalisches Institut, Justus-Liebig-Universität Giessen (2007).

[Mar01] P. Marciniewski, *Fast Trigger Systems for Experiments in High Energy Physics*, Ph. D. Thesis, Uppsala University, Schweden (2001).

[Mcg06] J. C. McGeorge, private communication (2006).

[Mil07] D. H. Miller *et al.* (CLEO Collaboration), Phys. Rev. Lett. **99**, (2007) 122002.

[Nov91] R. Novotny, IEEE Trans. on Nucl. Sc. **38** (1991) 392.

[Oku62] S. Okubo, Prog. Theor. Phys. **27** (1962).

[Pev61] A. Pevsner *et al.*, Phys. Rev. Lett. **7** (1961) 421.

[Plo92] F. Plouin *et al.*, Phys. Lett. **B 276** (1992) 526.

[Rei99] A. Reiter, *Entwicklung und Test eines ortsauflösenden Detektors für die Photonenmarkierungsanlage*, Diplomarbeit, Institut für Kernphysik, Johannes Gutenberg-Universität Mainz (1999).

[Rei04] A. Reiter, *A study of the energy calibration of the tagger microscope*, A2 Internal Report, Institut für Kernphysik, Johannes Gutenberg-Universität Mainz (2004).

[Rei06] A. Reiter *et al.*, Eur. Phys. J. **A 30** (2006) 461.

[Ren02] F. Renard *et al.* (GRAAL Collaboration), Phys. Lett. **B 528** (2002) 215.

[Sch01] A. Schmidt, *Photoproduktion neutraler Pionen am Proton mit linear polarisierten Photonen im Bereich der Schwelle*, Dissertation, Institut für Kernphysik, Johannes Gutenberg-Universität Mainz (2001).

[Sch04] S. Schumann, *Test der Sampling ADCs für den Crystal Ball-Detektor*, Diplomarbeit, Institut für Kernphysik, Johannes Gutenberg-Universität Mainz (2004).

[Sch07] S. Schumann, *Strahlungsbegleitete π^0-Photoproduktion am Proton*, Dissertation, Helmholtz-Institut für Strahlen- und Kernphysik, Rheinische Friedrich-Wilhelms-Universität Bonn (2007).

[Tho07] A. Thomas, *Crystal Ball Hydrogen (Deuterium) Target manual*, A2 Internal Report, Institut für Kernphysik, Johannes Gutenberg-Universität Mainz (2007).

[Tia94] L. Tiator, C. Bennhold, and S. S. Kamalov, Nucl. Phys. **A 580** (1994) 455.

[Unv04] M. Unverzagt, *Energie-Eichung des Crystal Ball-Detektors am MAMI*, Diplomarbeit, Institut für Kernphysik, Johannes Gutenberg-Universität Mainz (2004).

[Unv08] M. Unverzagt, *Bestimmung des Dalitz-Plot-Parameters α für den Zerfall $\eta \to 3\pi^0$ mit dem Crystal Ball am MAMI*, Dissertation, Helmholtz-Institut für Strahlen- und Kernphysik, Rheinische Friedrich-Wilhelms-Universität Bonn (2008).

[Unv10] M. Unverzagt, private communication (2010).

[Wal69] R. L. Walker, Phys. Rev. **182** (1969) 1729.

[Wal90] Th. Walcher, Prog. Part. Nucl. Phys. **24** (1990) 189.

[Web01] R. Brun, F. Rademakers *et al.*, *ROOT - an object oriented data analysis framework*, http://root.cern.ch/.

[Web02] D. Drechsel, S. S. Kamalov, L. Tiator, *MAID 2003: A unitary isobar model for pion photo- and electroproduction on the nucleon*, http://www.kph.uni-mainz.de/MAID/.

[Web03] W.-T. Chiang, L. Tiator, *η-MAID 2003: A reggeized isobar model for η photoproduction on the proton*, http://www.kph.uni-mainz.de/MAID/.

[Web04] NIST Standard Reference Data, http://webbook.nist.gov/chemistry/fluid/.

[Yao06] W.-M. Yao *et al.* (Particle Data Group), J. Phys. **G 33** (2006) 1.

[Zeh08] F. Zehr, *Measurement of the $\pi^0\pi^0$ photoproduction off the proton at threshold and in the second resonance region*, Ph. D. Thesis, University of Basel, Switzerland (2008).

Acknowledgements

Writing this thesis has been a great experience, and I would like to thank the people who helped me during these years and made them enjoyable. First of all, I would like to thank Prof. Dr. Reinhard Beck for giving me the opportunity to join the A2 collaboration in Mainz and work on such an interesting topic. During these years, he was always ready to answer any questions and to give a helpful advice. Also his friendly attitude created comfortable conditions for work, and it was a great pleasure to be part of the group.

This thesis would not be possible without the tagger microscope, which was constructed within the framework of diploma thesis by Dr. Andreas Reiter, who also made an essential contribution to the calibration of this device. Thanks for introducing me into the "secrets" of the calibration procedures and into statistical physics. Special thanks to Dr. Cameron McGeorge for very helpful enthusiastic discussions on the calibration of the tagger microscope, on the estimation of the uncertainty of the calibration, and also for careful proof-reading of this thesis. Without these discussions the calibration results would not be so good.

Also thanks to Dr. Marc Unverzagt, a good advice-giver, and a proof-reader of this thesis. He was always able to find time, and patiently explained how do things work. I really appreciate his help, especially concerning the data analysis.

I also would like to thank all former Ph. D. students (doctors now) who participated in the experiments in these years for their hard work during the shifts and for the calibration of every single part of the detector setup. Many thanks to Benedicte Boillat, Jason Brudvik, Richard Codling, Evie Downie, Ralf Gregor, Dirk Krambrich, Stefan Lugert, Matthias Rost, Sven Schumann, Claire Tarbert, Marc Unverzagt, and Fabien Zehr. I did not forget the undergraduate students of Mount Allison University and The George Washington University for their assistance.